ADVANCED NOMA TECHNIQUES FOR SPECTRAL AND ENERGY EFFICIENCY IN NEXT-GENERATION WIRELESS NETWORKS

Ph.D. Thesis

by

SHUBHAM BISEN

DEPARTMENT OF ELECTRICAL ENGINEERING
INDIAN INSTITUTE OF TECHNOLOGY INDORE

October, 2024

ADVANCED NOMA TECHNIQUES FOR SPECTRAL AND ENERGY EFFICIENCY IN NEXT-GENERATION WIRELESS NETWORKS

A THESIS

Submitted in partial fulfillment of the

requirements for the award of the degree

of

DOCTOR OF PHILOSOPHY

by

SHUBHAM BISEN

DEPARTMENT OF ELECTRICAL ENGINEERING

INDIAN INSTITUTE OF TECHNOLOGY INDORE

October, 2024

INDIAN INSTITUTE OF TECHNOLOGY INDORE

CANDIDATE'S DECLARATION

I hereby certify that the work which is being presented in the thesis entitled "**Advanced NOMA Techniques For Spectral And Energy Efficiency In Next-Generation Wireless Networks**" in the partial fulfillment of the requirements for the award of the degree of DOCTOR OF PHILOSOPHY and submitted in the DEPARTMENT OF ELECTRICAL ENGINEERING, Indian Institute of Technology Indore, is an authentic record of my own work carried out during the time period from November 2019 to October 2024 under the supervision of Prof. Vimal Bhatia, Professor, Indian Institute of Technology Indore, India.

The matter presented in this thesis has not been submitted for the award of any other degree of this or any other institute.

08/10/2024

Signature of the student with date
(SHUBHAM BISEN)

This is to certify that the above statement made by the candidate is correct to the best of my knowledge.

08/10/24

Signature of Thesis Supervisor with date
(Prof. VIMAL BHATIA)

Shubham Bisen has successfully given his Ph.D. Oral Examination held on February 21, 2025.

21/02/2025

Signature of Thesis Supervisor with date
(Prof. VIMAL BHATIA)

ACKNOWLEDGEMENTS

I want to take this opportunity to express my gratitude to everyone who has kindly supported me from the beginning of my Ph.D. career. First and foremost, I would like to express my deepest gratitude to God for the guidance, strength, and blessings that have supported me throughout this challenging journey.

I express my deepest gratitude to my Ph.D. supervisor, Prof. Vimal Bhatia, for his invaluable guidance, motivation, and gracious support throughout my thesis. Your willingness to provide me with the independence to explore different ideas while always being available for support and advice has been invaluable in fostering my growth as a researcher. A heartfelt thank you to the members of the PSPC committee, Prof. Mukesh Kumar and Prof. Abhirup Datta, for their fruitful discussions and suggestions towards my research.

I express my sincere gratitude to the TIH Foundation for IoT and IoE, IIT Bombay, for the financial assistance, which greatly supported my research endeavours. I am also deeply thankful to the Metiy Convergence, Communications & Broadband Technologies project for facilitating my visit to CEWiT, IIT Madras, where I had the opportunity to work on the 5G test bed. I would also like to thank the Finnish national agency, the TFK program, for the financial assistance for the research visit to Oulu University, Finland, which broadened my international exposure and research perspective. Additionally, I am grateful to the IEEE ANTS and COMSNETS travel grants, which enabled me to present my work at international conferences and helped me meet new people and experts who have helped shape my Ph.D. thesis.

There is a great purpose for everyone we meet in our life. I have great pleasure in acknowledging my gratitude to all the members of the Signal and Software group (SaSg) for their support during the tough times and for never letting me feel alone on this journey. I want to extend my special thanks to my seniors and friends: Justin Jose, Deepak Kumar, Amit Baghel, Abhinav Singh Parihar, Vidya Bhaskar Shukla, Vaishali Sharma, Purva Sharma, and, last but not least, Anupma, for the invaluable support and friendship throughout this journey. I would also like to thank my senior, Dr Parvez Shaik, for their constant support, knowledge-sharing, caring, and guidance, especially at the starting phase of my PhD. I also thank all the SaSg juniors who helped me in several ways during my thesis work.

Moreover, whatever little achievements I have attained, I owe to my parents, to whom I am proud to dedicate this thesis. A special thanks to my sister and brother-in-law. They have always been a source of inspiration for me and have kept my trust and faith in whatever I do. Your endless love, sacrifices, and unwavering belief in me have been my most significant source of strength. I sincerely thank my best friend and now my wife, Gayatree Mishra, for her steadfast support throughout this research journey. Her encouragement and emphasis on hard work were essential for completing the PhD, and her presence has positively transformed my life.

SHUBHAM BISEN

Dedicated to my family and my wife

ABSTRACT

The evolution of wireless communication beyond fifth-generation (5G) and towards sixth-generation (6G) networks necessitates advancements in spectral efficiency, energy efficiency, and massive connectivity. To address these demands, non-orthogonal multiple access (NOMA) has emerged as a promising multiple access scheme that enables multiple users to share the same resources efficiently. However, practical challenges such as multi-user interference, error propagation in successive interference cancellation (SIC), imperfect channel state information (CSI), and transceiver hardware impairments (HIs) significantly impact system performance. Additionally, the increasing demand for self-sustainable communication has motivated the exploration of energy harvesting (EH) and backscatter communication (BC), which improve energy efficiency by utilizing ambient radio frequency signals. The thesis investigates advanced NOMA-based frameworks that integrate HQAM, EH, and BC to enhance wireless systems' spectral and energy efficiency under realistic constraints.

The initial focus of this thesis is the error performance analysis of HQAM-based NOMA systems. The average symbol error rate (ASER) of HQAM schemes is analyzed by considering a two-user NOMA downlink system, and closed-form expressions are derived over generalized Nakagami-m fading channels. The impact of modulation order, power allocation, and channel conditions on ASER performance is investigated, providing critical insights into optimal constellation design for NOMA transmission. Furthermore, the feasibility of HQAM in practical NOMA systems is assessed, and a power allocation strategy is proposed to improve its error performance.

Since interference management and error propagation remain significant challenges in NOMA systems, the thesis proposes a multiple feedback successive interference cancellation (MF-SIC) algorithm for ultra-dense internet-of-things (IoT) networks. The proposed MF-SIC algorithm enhances the reliability of SIC by utilizing multiple feedback iterations, significantly reducing error propagation and improving detection performance. The effectiveness of MF-SIC is evaluated in both uplink and downlink NOMA systems under the presence of imperfect CSI, and a comparative analysis with conventional SIC is conducted to demonstrate its robustness.

To address the need for self-sustainable wireless networks, this thesis investigates an EH cooperative NOMA system, where multiple decode-and-forward relays assist the transmission while harvesting energy from the base station. A relay selection strategy is implemented to optimize performance, and closed-form expressions for outage probability and ergodic rate are derived under perfect and imperfect CSI/SIC conditions. Additionally, an asymptotic analysis of outage probability is presented to provide further insights into system reliability. The results demonstrate how energy-harvesting relays can enhance coverage and improve the energy efficiency of cooperative NOMA networks.

Further extending the concept of EH-based NOMA, a hybrid backscatter-assisted NOMA system is introduced, integrating passive and active relaying modes to support low-power IoT devices. A novel hybrid relay protocol is developed, where the relay simultaneously performs energy harvesting, active information reception, and passive backscatter transmission. The system is analyzed under nonlinear EH constraints, residual hardware impairments, and channel estimation errors, and the performance is evaluated in terms of outage probability, system throughput, and

energy efficiency. The findings highlight the potential of backscatter-NOMA as a viable solution for extending connectivity in energy-constrained IoT networks.

Finally, the thesis presents a symbiotic radio (SR)-enabled NOMA framework that facilitates dynamic spectrum sharing between the primary network and IoT devices. The SR-based system allows passive IoT devices to backscatter primary signals while improving the performance of the primary network itself. The outage probability for NOMA users is analyzed under different deployment scenarios, considering cases with and without a direct link between the primary base station and the far user. The results demonstrate that SR-enabled NOMA significantly outperforms orthogonal multiple access making it an attractive solution for next-generation ultra-dense wireless networks.

The analytical models presented in this thesis are extensively validated through Monte Carlo simulations, confirming the accuracy of the derived expressions. The proposed methodologies contribute to the advancement of next-generation multiple access techniques, offering novel insights into the design of spectrally and energy-efficient NOMA-based communication systems for beyond 5G and 6G networks.

Contents

List of Figures

List of Tables

List of Abbreviations/Acronyms

AF amplify-and-forward.

ASER average symbol error rate.

AWGN additive white Gaussian noise.

BC backscatter coomunication.

BER bit error rate.

BPSK binary phase-shift keying.

CC computational complexity.

CDF cumulative distribution function.

CDRT coordinated direct relay transmission.

CEE channel estimation error.

CP constellation point.

CR cognitive radio.

CSI channel state information.

DF decode-and-forward.

DLI direct link interference.

EH energy harvesting.

FD full-duplex.

HD half-duplex.

HQAM hexagonal QAM.

i.i.d. independent and identically distributed.

i.n.i.d. independent and non-identically distributed.

IoT Internet-of-Things.

IT information transmission.

LoS line-of-sight.

MF-SIC multiple feedback based SIC.

MIMO multiple-input and multiple-output.

NC neighbouring constellations.

NLD non-linear distortion.

NLPA non-linear power amplifier.

NOMA non-orthogonal multiple access.

PA power amplifier.

PAPR peak-to-average-power ratio.

PDF probability density function.

PS power splitting.

QAM quadrature amplitude modulation.

QoS quality-of-service.

QPSK quadrature phase-shift keying.

RF radio frequency.

RV random variable.

SC superposition coding.

SIC succesice interference cancellation.

SINR signal-to-interference-plus-noise ratio.

SNR signal-to-noise ratio.

SQAM square QAM.

SR symbiotic radio.

SWIPT simultaneous wireless information and power transfer.

TS time switching.

List of Symbols

- Basic arithmetic and calculus notations with their definitions.

Elementary & Special Functions

Notation	Definition
$\Gamma(x)$	$= \int_0^\infty t^{x-1} e^{-t}\, dt$ is the Gamma function.
$\Gamma(x, y)$	$= \int_y^\infty t^{x-1} e^{-t} dt$ is the upper incomplete Gamma function.
$\Upsilon(x, y)$	$= \int_0^y t^{x-1} e^{-t} dt$ is the lower incomplete Gamma function.
${}_1F_1(a, b; x)$	$= \sum_{r=0}^{\infty} \frac{(a)_r}{(b)_r} \frac{x^r}{r!}$ is the confluent hypergeometric function of first kind.
${}_2F_1(a, b; c; x)$	$= \sum_{r=0}^{\infty} \frac{(a)_r (b)_r}{(c)_r} \frac{x^r}{r!}$ is the Gauss hypergeometric function.
$\mathcal{W}_{\lambda,\mu}(x)$	$= \frac{x^{\mu+\frac{1}{2}} e^{-\frac{x}{2}}}{\Gamma\left(\mu-\lambda+\frac{1}{2}\right)} \int_0^\infty e^{-xt} t^{\mu-\lambda-\frac{1}{2}} (1+t)^{\mu-\lambda+\frac{1}{2}}\, dt$ denotes the Whittaker function.
$I_v(x)$	$= \sum_{r=0}^{\infty} \frac{(\frac{1}{2})^{v+2r}}{r!\Gamma(v+r+1)} x^{v+2r}$ denotes the v^{th} order modified Bessel function of the first kind.
$\mathcal{K}_v(x)$	$= \frac{1}{2} \left(\frac{x}{2}\right)^v \int_0^\infty \frac{\mathrm{e}^{-t-\frac{x^2}{4t}}}{t^{v+1}} dt$ represents the modified Bessel function of the second kind of order v.
$G_{p\ q}^{m\ n}\left({a_1,\dots,a_p \atop b_1,\dots,b_p} \middle\vert x\right)$	$= \frac{1}{2\pi i} \int_{\mathcal{L}} \frac{\prod_{j=1}^{m} \Gamma(b_j+s) \prod_{j=1}^{n} \Gamma(1-a_j-s)}{\prod_{j=m+1}^{q} \Gamma(1-b_j-s) \prod_{j=n+1}^{p} \Gamma(a_j+s)} z^s\, ds$ is the MeigerG function.
$Q(x)$	$= \frac{1}{\sqrt{2\pi}} \int_x^\infty e^{-\frac{t^2}{2}} dt$ is the Gaussian Q-function.

Probability & Statistics

Let X be a random variable (RV).

Notation	Definition
$\mathbb{E}[\cdot]$	statistical expectation operator
$\mathcal{P}(\cdot)$	statistical probability operator
$f_X(\cdot)$	probability density function (PDF) of a RV X
$F_X(\cdot)$	cumulative distribution function (CDF) of a RV X
$\mathcal{CN}(\mu, \sigma^2)$	complex normal distribution with mean μ and variance σ^2

Chapter 1

Introduction

1.1 Evolution of Wireless Communications: From 1G to 6G

In the early 1980s, the foundations of mobile telecommunications were laid with the first generation (1G) of mobile networks. It introduced seamless connectivity of voice services in determined zones of the world. By being an analogue technology, it had some limitations, for example, it only supported one user per channel. In terms of its radio access technology (RAT), frequency division multiple access (FDMA) was used, multiple users were assigned to different frequencies but frequency gaps in-between channels were needed, to minimize adjacent-channel interference (ACI). The transition to second generation (2G) in the early 1990s marked a significant technological leap, moving from analog to digital systems. This new generation introduced enhanced voice quality, with data speeds of up to 384 Kbps, SMS text messaging, and rudimentary data services, enhancing communication efficiency. The 2G of mobile networks, also known as global system for mobile communications (GSM), used time division multiple access (TDMA), a RAT that allowed eight users to share the same channel, occupying 200 KHz. The third generation (3G) networks launched in the early 2000s, bringing speed and functionality improvements. These networks offered data transfer rates of at least 144 Kbps, significantly enhancing mobile internet capabilities and supporting services like video calls. The 3G mobile networks, also known as universal mobile telecommunications system (UMTS) brought code division multiple access (CDMA) as its RAT, allowing users to share the same frequency and communicate at the same time, using different orthogonal codes. This was a breakthrough from a spectral efficiency theoretical point of view since users could share the same time/frequency but it had some limitations, namely, the bandwidth used was very large compared to 2G and there was a limitation in the number of codes that could be assigned to the users. The fourth generation (4G), rolled out in the early 2010s, provides a monumental advancement in mobile technology, offering broadband-like speeds and low latency. This generation enabled high-definition video streaming, real-time online gaming, and seamless video conferencing, fundamentally changing user interactions with their devices. 4G mobile networks, also known as long term evolution (LTE), came as a response to the need of faster and better mobile broadband. From a spectral efficiency perspective, the RAT used in downlink LTE, orthogonal frequency division multiple access (OFDMA), is not great because the OFDMA sub-carriers are packed in 20 MHz of spectrum. The fifth generation (5G) networks began rolling out around 2019, heralding a new era of hyperconnectivity with unprecedented speeds and ultra-low latency. 5G can support vast numbers of connected devices and is crucial for enabling applications such as Internet-of-things (IoT), smart cities, and autonomous vehicles. Its capacity for high-speed data transmission is foundational for innovative sectors, including healthcare, transportation, and entertainment. Typical peak data rates are expected to reach 20 Gbps with an emphasis on reliability and bandwidth efficiency. New performance indicators introduced during this phase included metrics for ultra-reliable low-latency communication (URLLC) and massive machine-type communications (mMTC), reflecting the technological advancements and more complex use cases. Expected to debut in the early 2030s, sixth generation (6G) will push the boundaries of mobile technology, potentially delivering data rates up to 1 terabit per second. Innovations in 6G may include advanced applications like immersive extended reality (XR) and artificial intelligent (AI)-driven networks, promising to fundamentally transform daily life and various industries. This future generation will support even more incredible levels of connectivity, making it integral to the next chapter of mobile technology evolution In wireless communication, ultra-high data rates and energy efficiency, URLLC, enhanced mobile broadband

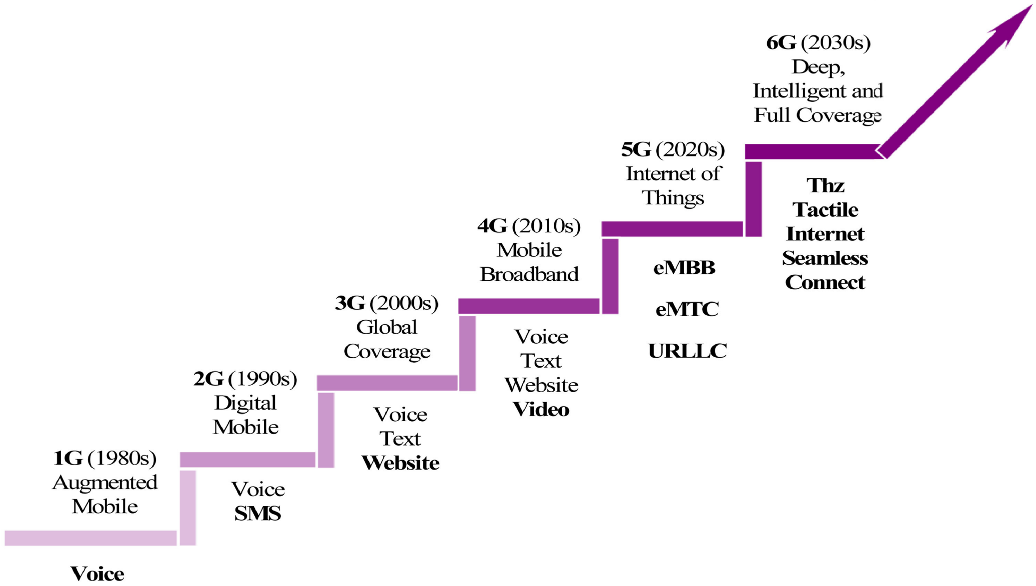

Figure 1.1: Mobile Network Evolution [1].

(eMBB), global coverage and connectivity, and mMTC are stringent requirements for beyond 5G/6G networks [3]. At the physical layer, the speed of the cellular links has increased manyfold from 50 kbps in 2G systems, 144 kbps in 2.5G systems, approximately 2 Mbps in 3G systems to around 100 Mbps in 4G systems (3GPP-LTE and WiMAX), around 1 Gbps in 5G and around 1 Tbps in 6G systems [4]. Similarly, the speed of indoor wireless local area networks (LANs) has increased from 11 Mbps in IEEE 802.11b to 300 Mbps in IEEE 802.11n within the last twenty years [5]. Although 4G systems provide many services with high data rates, there is still a gap between customers' requirements and the services provided by 4G systems. To fill this gap, current and future research is directed toward next-generation wireless communication technologies such as non-orthogonal multiple access (NOMA), cooperative relaying, and higher order modulation scheme. As the frequency spectrum for wireless communication is worldwide allocated, efficient utilization of the limited bandwidth along with high data rate transmission over multipath fading channels is also a challenging task in practical wireless communication systems. Thus, various challenges exist in the design and operation of wireless communication systems which must be studied and analyzed to get high data rate transmission with high reliability and low latency over multipath fading channels.

1.2 Non-Orthogonal Multiple Access

The fundamental concept of NOMA lies in leveraging the power domain for multiple access, as illustrated in Figure 1.2. Unlike conventional multiple access technologies, NOMA introduces a new power dimension to perform multiplexing within the existing time, frequency, or code domains. In essence, NOMA can be seen as an 'add-on' technique with the potential to seamlessly integrate with existing multiple access paradigms, offering significant improvements in spectral efficiency and connectivity [6, 7].

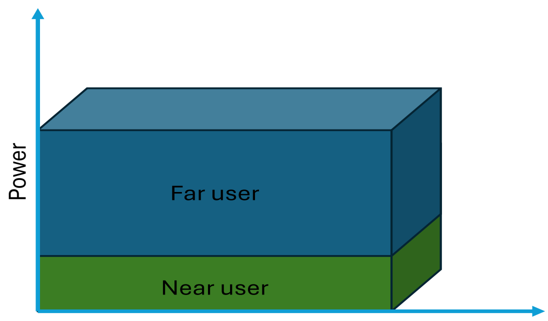

Figure 1.2: Illustration of NOMA transmission.

The key enabling technologies for NOMA are superposition coding (SC) and successive interference cancellation (SIC). These principles have evolved significantly in both theory and practice, making NOMA feasible for next-generation networks. In NOMA, the base station uses the SC technique to transmit a composite signal formed by superimposing coded signals from multiple users' messages. The users selection also plays a critical role in NOMA performance, users are typically arranged according to their channel gains. User selection in NOMA is based not only on channel conditions but also on quality-of-service (QoS) requirements [8]. In a typical NOMA scenario, users with different channel conditions are paired together. For instance, a user with a strong channel (near user) is paired with a user with a weaker channel (far user). The user with the poorer channel condition is allocated more power to ensure it can decode its own message while treating other users' signals as interference. Conversely, users with better channel conditions apply SIC to subtract the interference from far user, enabling them to decode their messages effectively as shown in Figure 1.3. In the scenario when channel condition of users are not diverse, the users are selected based on the QoS requirement. Users with higher QoS demands may be prioritized in power allocation and pairing strategies to ensure that their stringent latency, reliability, or throughput needs are met.

Unlike traditional orthogonal multiple access (OMA) schemes, which often use a power allocation policy like water-filling, NOMA allocates more power to users with poorer channel conditions. This ensures that these users can decode their messages while treating other users' messages as noise. For users with better channel conditions, SIC is employed to subtract the interference caused by signals from users with poorer conditions, thus enhancing overall system performance.

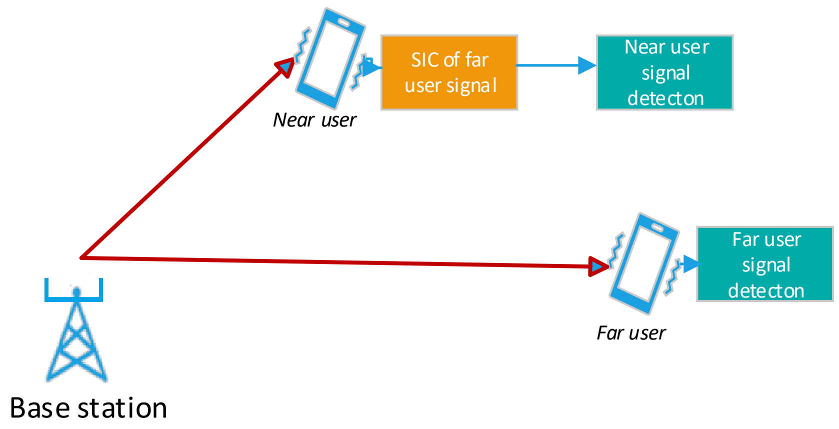

Figure 1.3: Illustration of downlink power domain NOMA transmission.

Superposition Coding

First proposed by Cover in 1972, the concept of superposition coding is a fundamental component of coding schemes designed to achieve capacity on a scalar Gaussian broadcast channel. The core idea behind SC is to encode the signal of a user with poor channel conditions at a lower rate, and then superimpose the signal of a user with better channel conditions on top of it. Building on its strong theoretical foundation in information theory, SC has been applied to various types of channels, including interference channels, relay channels, and multiple access channels. While these theoretical advancements have provided ample motivation for the use of SC, a significant breakthrough has been its successful transition from theory to practical implementation.

Successive Interference Cancellation

SIC is a promising technology for enhancing network capacity by efficiently managing interference in wireless networks. The SIC technique achieves this by enabling the user with a stronger link to first decode the signal intended for the user with a weaker link. The stronger user then regenerates the weaker user's signal and subtracts it from the received signal to eliminate interference. Finally, the stronger user decodes its own information without any interference from the weaker user. SIC has been shown to achieve the boundaries of Shannon capacity for both broadcast channels and multiple access networks. Moreover, one of the key advantages of SIC is its low hardware complexity at the receiver side [9, 10].

Downlink and Uplink NOMA Transmission

Downlink NOMA transmission employees the superposition coding technique at the base station for sending superimposed signals and the SIC technique at users for interference cancellation. More specifically, as shown in Figure 1.3, at the side of near user, the interference of the superimposed signal can be cancelled with employing SIC technique. While at the side of far user, it will decode the message by treating near user as interference.

Unlike the downlink NOMA transmission, the uplink NOMA transmission requires that the base station should send controlling signals to multiple users for power allocation first. Then multiple users transmit their own information to the base station in the same orthogonal resource block resource. With the aid of SIC technique, the base station decodes all the messages of users following increasing/decreasing decoding order.

1.3 Cooperative Communication

In wireless communication, multipath fading is one of the major impairments that cause reduced reliability, robustness, and coverage of a network. Cooperative relaying has been reckoned as an effective approach to counteract the effect of multipath fading in wireless communications. Cooperative relaying can mitigate the path-loss and shadowing effects by introducing an intermediate node i.e., a relay node in between the source and destination. In this way, three distinct gains can be achieved: (i) diversity is increased because of the additional and independent path available for signal propagation between source and destination; (ii) communication between source and destination is performed in hops i.e., the transmitter is closer to the receiver and path-loss is reduced; (iii) the smart relay position mitigates the shadowing effect [11]. The basic idea of cooperative relaying is to process the information between source and destination through alternative indirect multipath via intermediate relay nodes. The cooperative relaying has been incorporated in the standards such as LTE-Advanced and IEEE 802.16j [12]. The transmitted signal is processed through different relaying schemes. Commonly used relaying schemes are

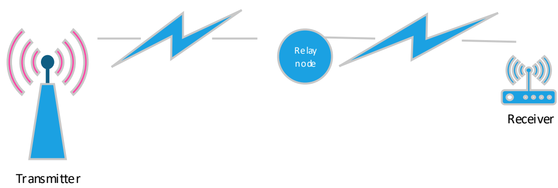

Figure 1.4: Cooperative communication.

- Amplify-and-forward (AF)
- Decode-and-forward (DF)

Amplify-and-forward:

In AF relaying, the relay receives the signal coming from the source node, amplifies it, and forwards it to the destination. The signal received at the relay is affected by channel fading and noise. Hence, noise is also amplified at the relay along with the information signal. AF is the simplest relaying technique because no further processing is required at the relay. However, since a power amplifier (PA) is used to amplify the signal, AF relaying is sensitive to PA nonlinearity i.e., non-linear PA (NLPA), and the impact of non-linear distortion (NLD) becomes a major issue in a multi-hop network.

Decode-and-forward:

In DF relaying, the relay first decodes the received information signal from the source, and then re-encodes and transmits it to the destination. Both decoding and re-encoding are performed at the relay. Ideally, the same information is retransmitted through the relay, so noise is not amplified and fading impairments of the source to relay channel are mitigated. However, the processing load at the relay is greater than AF relaying, and an accumulation in error occurs if there is an error in the recovery of the information signal at the relay which is also forwarded to the destination.

1.4 Wireless Energy Harvesting

In wireless communication networks, energy harvesting (EH) is a new paradigm that enables terminals to recharge their batteries using the received radio-frequency (RF) signal [13]. The energy constraint issue in wireless networks can be resolved by RF-EH. EH is the process of transforming RF energy into electrical energy. In contrast to traditional battery or grid-powered communications, the EH offers several unique advantages and promising benefits for future wireless communications, such as self-sustaining functionality, reduction of carbon footprint, wireless nodes that don't require battery replacement, and many more [14]. As a result, EH in wireless networks is becoming increasingly popular in a variety of applications, such as medicinal implants, remote environmental monitoring, etc. EH-enabled receiver architectures such as time switching (TS), power splitting (PS), and hybrid time switching and power splitting are commonly used.

Time Switching

TS architecture, also known as co-located receiver architecture, shares the same antenna for EH and information reception [15]. As illustrated in Figure 1.5, the receiver employed in this architecture includes an RF energy harvester, an information decoder, and a switch that alters the system's receiving antenna. Based on a TS sequence, the receiver antenna switches between the energy harvester and informa-

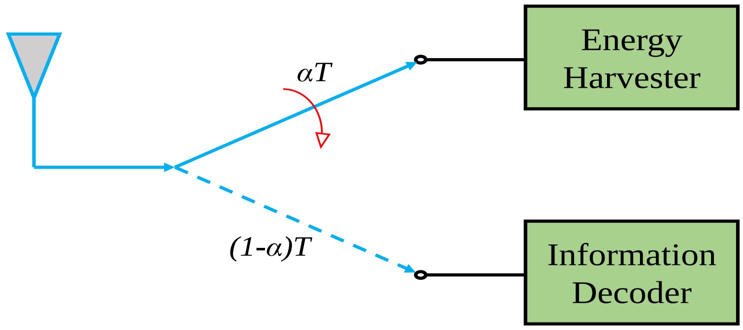

Figure 1.5: Time switching receiver architecture.

tion decoder circuit periodically. The received RF signal is switches between energy harvester and information decoder into $\alpha T : (1 - \alpha)T$ proportion, where α denotes time switching factor and T denotes frame duration. Further, the TS receiver also requires accurate information/energy scheduling and time synchronization. The TS factor can be optimized to achieve optimum performance.

Power Splitting

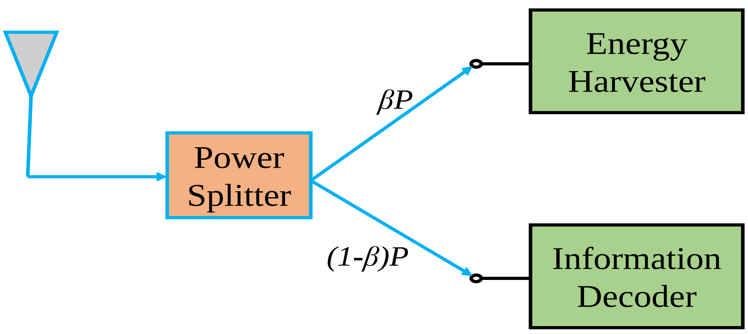

Figure 1.6: Power splitting receiver architecture.

The PS receiver divides the received signal into two power streams of different power levels with a certain PS ratio before signal processing is performed at the receiver [15]. To enable simultaneous EH and information decoding, both power streams are then delivered to an information decoder and energy harvester as depicted in Figure 1.6. The power splitter splits the received power between energy harvester and information decoder into $\beta P : (1 - \beta)P$ proportion, where β denotes power splitting ratio and P denotes transmit power. Further, by varying PS ratios, the information rate and the harvested energy can be balanced according to the system requirements. Furthermore, the overall performance can also be improved by optimizing the PS ratio.

1.5 Backscatter Communication

Backscatter communication (BC) is an ultra-low-power wireless communication technology that enables devices to communicate by reflecting existing RF signals. This method leverages ambient signals from sources like Wi-Fi, TV towers, or dedicated RF emitters, allowing devices to operate without batteries or with minimal power consumption. The BC refers to a design where a radio device transmits data via reflecting and modulating an incident RF signal by adapting the level of antenna impedance mismatch to vary the reflection coefficient and furthermore harvests energy from the signal for operating the circuit. Backscatter devices do not require oscillators to generate carrier signals that are obtained from the air instead. Furthermore, using the simple analog modulation scheme, the device requires no analog-to-digital converters (ADCs) used in the case of digital modulation. As a result of these features, a backscatter transmitter consumes power orders-of-magnitude less than a conventional radio. Traditionally, BC is widely used in the application of RF identification (RFID) where a reader powers and communicates with a RFID tag over a short range typically of several meters [16].

In the BC as shown in Figure 1.7, the radiation or incident signal is reflected by the backscatter tag and then the transmit information at the backscatter transmitter is remodulated to the reflected signal and delivered to the backscatter receiver. Signal reflection by the backscatter tag is involved in the BC. This is different from the traditional communications, where the transmit information is included in the radiation signal and delivered to the receiver directly. In particular, instead of initiating their own RF transmissions as conventional wireless systems, a backscatter transmitter can send data to a backscatter receiver just by tuning its antenna impedance to reflect the received RF signals. Specifically, the backscatter transmitter maps its bit sequence to RF waveforms by adjusting the load impedance of the antenna [16].

BC is particularly suited for IoT applications, where numerous low-power devices are required to communicate over short distances. Its ability to support EH

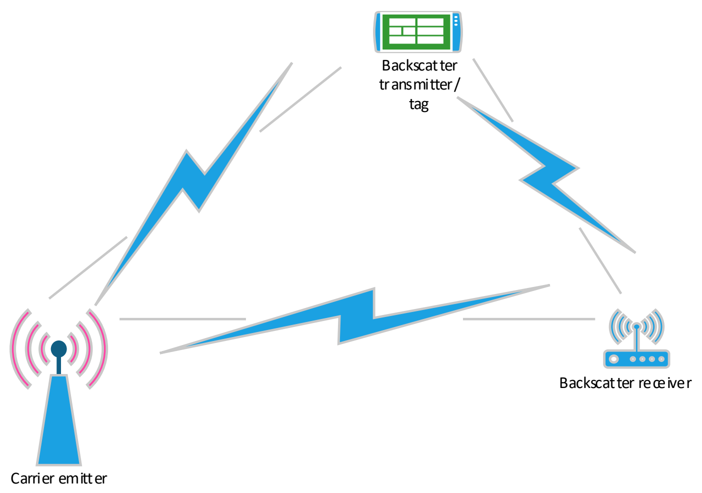

Figure 1.7: Backscatter communication architecture.

and enable battery-free or extended-lifespan devices makes it ideal for sustainable, scalable IoT networks, especially in environments with dense deployments of sensors and smart objects. The traditional reader-tag configuration is unsuitable for IoT since typical nodes are energy-constrained and may not be able to wirelessly power other nodes for communications over sufficiently long distances. This motivated the design of a BC system powered by RF EH, where the transmission of a backscatter node relies on harvesting energy and reflecting incident RF signals from the ambient environment such as TV, Wi-Fi and cellular signals.

1.6 Symbiotic Radio

The symbiotic radio (SR), has attracted significant attention to support IoT connections using cellular (Primary) networks due to its spectrum and energy mutualistic sharing feature. SR combines the advantages of BC and cognitive radio (CR), and has gained significant attention as a solution for achieving spectrum-efficient, energy-efficient, and cost-effective communications [17, 18]. In the SR system, the IoT device transmits information by passively backscattering the primary signal, and thus the primary and IoT transmissions share the same spectrum and energy resources. For example, smart home sensors (tags) in an IoT network can be integrated with a primary network. The secondary tags form an BC network. This symbiotic relationship improves overall performance, enhances energy efficiency, and utilizes wireless resources more efficiently. The passive tags can exploit the primary signal for EH and data transmission.

Similar to CR systems, SR achieves spectrum sharing communication with co-existence of primary and secondary systems without causing interference to the primary system as in CR systems. In return, due to the collaboration between the primary and IoT transmissions, the backscattered signal serves as a multipath component instead of interference, leading to an enhancement to the primary transmission. Therefore, both cellular and IoT transmissions can benefit from their co-existence in SR. Due to the outstanding spectrum and energy mutualistic sharing properties, SR has been regarded as an enabling technology for massive IoT connections in 6G networks.

1.7 Wireless Channel: Modeling and Performance Metrics

The wireless communication channel is a medium through which the information signals traverse from source to destination. Information signals suffer from various impairments during propagation. In this section, the fundamentals of wireless propagation, multipath fading, and various channel models are discussed. Further, to characterize the performance of wireless systems, various fundamental performance metrics with their mathematical descriptions are explained.

1.7.1 Modeling of wireless channel

Fading in wireless communication is the fluctuation of signal strength due to factors like multipath propagation, obstacles, or motion. It results in signal attenuation, phase shifts, or interference over time, space, or frequency. Due to reflection, diffraction, refraction, or scattering, the transmitted signal in wireless communication traverses multiple paths to reach the destination (receiver). Different replicas of the transmitted signal (experiencing different amplitude, phase, and frequency variations) are combined at the destination. Further, due to constructive or destructive interference, amplification or attenuation in the signal power occurs which affects the robustness and reliability of the wireless communication system. In Figure 1.8, a typical signal propagation scenario between a transmitting and a receiving antenna through a multipath fading channel is depicted.

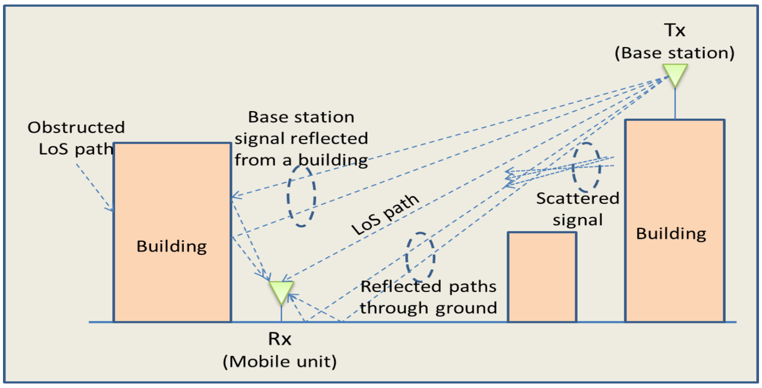

Figure 1.8: Wireless communication channel.

Small-scale and large-scale fading are the two primary categories of fading. Large-scale fading occurs mainly due to shadowing by large objects such as hills, buildings, and due to path loss as a function of distance, whereas small-scale fading occurs due to the constructive or destructive interference of multiple copies of the transmitted signal through multipath.

It is highly challenging to precisely mathematically describe fading because it varies with time, frequency, and geographic locations. Thus, substantial efforts have been directed to characterize fading statistically. According to the nature of the propagation environment, various precise and relatively simple statistical models are proposed to characterize the fading channels [19, 20]. In case of small-scale fading, the Rayleigh, Nakagami-m, Rician, Weibull, or $\alpha - \mu$ distributions are commonly used whereas, in case of large-scale fading, the Log-normal distribution is used.

Rayleigh distribution:

The Rayleigh distribution is the most popular method for describing the radio channel's statistical behavior. It is operated in the case where multipath propagation exists without a dominant line-of-sight (LoS) path between the end users and the base station. Due to the constructive or destructive interference of the multipath components, the in-phase and quadrature-phase components of the received signal are modeled with a zero mean complex Gaussian random process. Thus, the amplitude of the received signal is Rayleigh distributed.

Rician distribution:

The Rician distribution is preferred when there is a significant stationary non-LoS component between the end users. In this case, the random multipath gains a DC component from the superposition of the multipath components, which results in a dominating stationary non-fading component. In the absence of the strong LoS component, the Rayleigh distribution turns into a specific example of the Rician distribution.

Nakagami-m distribution:

Nakagami-m is used to characterize small-scale fading for dense signal scatters. It is also used in a variety of real-world applications such as modeling wireless signals and radio wave propagation due to its generalized fading characteristic for different values of the severity parameter m. One sided Gaussian distribution for $m = \frac{1}{2}$ and Rayleigh distribution for $m = 1$ are special cases of Nakagami-m distribution [21].

1.7.2 Performance metrics

To examine the performance of SWIPT-enabled wireless communication systems over fading channels, several performance metrics are used for different modulation schemes. To fix various design issues of wireless communication systems, these performance measures are used. Commonly used performance metrics are instantaneous signal-to-noise ratio (SNR), outage probability, system throughput, energy efficiency, ergodic capacity, and average symbol error rate (ASER) [20].

Instantaneous SNR:

The instantaneous SNR is a basic performance metric that is used to quantify the signal corruption due to noise. Instantaneous SNR is related to data detection as it is measured at the output of the receiver and is an excellent indicator of the overall fidelity of the communication system. Instantaneous SNR can be expressed as

$$\gamma = \frac{\text{Received signal power at the receiver}}{\text{Received noise power at the receiver}} = \frac{P|h|^2}{\sigma^2}, \tag{1.1}$$

where P, h, and σ^2 represent the transmit power, channel parameter, and noise variance, respectively. Due to the multipath fading in wireless communication, average SNR is a more appropriate performance metric than instantaneous SNR. Average SNR is the statistical averaging over the probability distribution of the fading and is given as $\Omega = \mathbb{E}[\gamma]$, where $\mathbb{E}[\cdot]$ represents the statistical expectation operator.

Outage Probability:

Outage probability is one of the important performance metric that depicts link failure probability and is mainly used in the case of a slow-fading scenario. It is defined as the probability that the received end-to-end instantaneous SNR (γ) of the considered system lies below a predefined threshold (γ_{th})

System throughput:

The system throughput is one of the important performance metrics to characterize spectrum utilization. It can also be referred to as mean spectral efficiency. Based on the derived expression of outage probability ($\mathcal{P}_{\text{out}}$), the system throughput can be formulated as

$$\tau = [1 - \mathcal{P}_{\text{out}}(\gamma_{\text{th}})]\, r_{\text{th}}. \tag{1.2}$$

Energy efficiency:

Energy efficiency is an important performance metric in the wireless communication system to achieve the vision of green communication systems. It is defined as the overall data transferred to the overall consumed energy. The overall data transferred is referred to as system throughput. Energy efficiency can be expressed as

$$\eta_{\text{EE}} = \frac{\tau}{P}. \tag{1.3}$$

Ergodic capacity:

Ergodic capacity quantifies the ultimate reliable communication limit over fading channels. Instantaneous capacity (measured in bps/Hz) is defined as the maximum rate achieved by the communication channel and can be determined as $C = \log_2(1+\gamma)$. Hence, ergodic capacity is obtained by averaging the instantaneous capacity over the PDF of the instantaneous SNR (γ).

Average symbol error rate (ASER):

ASER is an important performance metric for wireless communication systems that can be determined by averaging the symbols with error at the receiver. For any digital modulation technique, the generalized ASER expression by using the CDF-based approach can be given as

$$\mathcal{P}_e = -\int_0^{\infty} \mathcal{P}_s^{'}(e|x)\mathcal{P}_{out}(x)\mathrm{d}x, \tag{1.4}$$

where $\mathcal{P}_s^{'}(e|x)$ represents the first order derivative of the conditional SEP ($\mathcal{P}_s(e|x)$) for the received SNR.

1.8 Imperfections

In a practical system, there are many imperfections that limit the performance of wireless communication systems. These imperfections include hardware impairments (HIs), such as non-linearities in amplifiers and phase noise in oscillators, as well as channel estimation errors caused by dynamic environments. In this section, various imperfections such as imperfect channel state and transceiver HIs are discussed.

1.8.1 Imperfect channel state information

In a practical wireless communication system the knowledge of perfect channel state information (CSI) is a challenge and lead to imperfect knowledge of the channel conditions between the transmitter and receiver. This imperfect CSI can significantly impact system performance, leading to errors in data transmission and decreased overall efficiency. This imperfection primarily arises from factors such as channel estimation errors (CEE) and quantization errors, which are inherent in real-world systems. Further, other factors that affect the channel estimation performance are the time-varying channel, estimation method, and signal detection when combined with the channel estimation. Thus, the system's performance can be improved by utilizing an efficient channel estimation method that reduces channel estimation errors. A minimum mean square error (MMSE) estimator at the receiver estimates the channel with the help of some training symbols known as pilot symbols. Hence, the best combination of pilot patterns, estimation method, and signal detection provides improved performance at the cost of additional resources and is application-specific.

Under imperfect CSI, according to MMSE estimation [22, 23]

$$h_k = \hat{h}_k + \epsilon_k, \tag{1.5}$$

where h_k is actual channel between the transmitter and receiver and $\hat{h}_k$ is the estimate of the channel h_k, where h_k and $\hat{h}_k$ are jointly ergodic and stationary Gaussian process [24]. The ϵ_k is the CEE, which is assumed to be complex normal with mean zero and variance σ_e^2 [25]. The CEE arise due to the improper pilot pattern in channel estimation. A pilot pattern for estimating the channel should be performed as a function of coherence time and frequency. Otherwise, an irreducible error floor arises in the estimation.

To address the challenges posed by imperfect CSI, various strategies can be implemented. These include the use of robust resource allocation algorithms that consider the uncertainties arising from CSI inaccuracies and the development of advanced encoding and decoding techniques designed to operate effectively even with limited channel knowledge. Additionally, improving channel estimation algorithm and utilizing feedback mechanisms that can enhance overall performance in the presence of imperfect CSI.

1.8.2 Hardware impairments

In practice, wireless communication system hardware suffers from various types of impairments, such as phase noise, in-phase/quadrature-phase (I/Q) imbalances, etc. The HIs can be mitigated by the compensation algorithms, but there are always residual impairments [26]. The HIs have an adverse impact on achievable performance. The HIs create a mismatch between the intended signal x and what is actually generated and transmitted, and distort the received signal during the reception processing. By considering the impact of HIs, the received signal at the destination can be expressed as [27]

$$y = \sqrt{P}h\left(x + \eta_t\right) + \eta_r + n, \tag{1.6}$$

where P, $\eta_t \sim \mathcal{CN}(0, \kappa_t^2)$, $\eta_r \sim \mathcal{CN}(0, \kappa_r^2 P|h|^2)$, and $n \sim \mathcal{CN}(0, \sigma^2)$ represent the transmit power, distortion noise due to HIs in the transmitter, distortion noise due to HIs in the receiver, and the AWGN, respectively. The design parameters $\kappa_t \geq 0$ and $\kappa_r \geq 0$ characterize the level of impairments in the transmitter and receiver hardware, respectively. The parameters κ_t and κ_r are interpreted as error vector magnitudes. The error vector magnitude measures the RF HIs and can be defined as the ratio of the average distortion magnitude to the average signal magnitude. The design parameters κ_t and κ_r can be designed jointly by taking the aggregate distortion effect at the receiver as

$$\mathbb{E}_{\eta_t,\eta_r}\left[\left|\sqrt{P}h\eta_t + \eta_r\right|^2\right] = P\left|h\right|^2\left(\kappa_t^2 + \kappa_r^2\right). \tag{1.7}$$

The aggregate level of impairments $\kappa = \sqrt{\kappa_t^2 + \kappa_r^2}$ is sufficient to characterize transceiver HIs. By considering the aggregate level of transceiver HIs, (1.6) can be expressed as

$$y = \sqrt{P}h\left(x + \eta\right) + n, \tag{1.8}$$

where $\eta \sim \mathcal{CN}(0, \kappa^2)$ denotes distortion noise which describes the impact of HIs at both the transmitter and receiver. In particular, $\kappa = 0$ denotes the ideal transceiver i.e., $\kappa_t = \kappa_r = 0$. Meanwhile, the typical value of κ_t and κ_r lies in the range $\kappa_t, \kappa_r \in [0.08, 0.175]$ [27].

1.9 Motivation

Because of the importance of multiple access, there has been an ongoing quest during the past decade to develop next generation multiple access (NGMA). Among those potential candidates for NGMA, NOMA has received significant attention from both the industrial and academic research communities, and has been highlighted in the recently published International Mobile Telecommunications (IMT)-2030 Framework as follows: "for multiple access, technologies including NOMA and grant-free multiple access are expected to be considered to meet future requirements". NOMA is a promising technology for future wireless communication systems, enabling multiple users to share the same resources using power domain multiplexing. This approach significantly improves spectral efficiency and supports massive connectivity, which is essential for accommodating the growing number of devices in next-generation networks. Additionally, adaptive transmission schemes, which employ adaptive modulation and coding along with optimal power utilization, have become critical in modern and future wireless communication systems. These schemes are widely adopted in applications such as digital broadcasting, HDTV services, and telephone line modems due to their increased data throughput and spectral efficiency [28]. To further enhance data rates and achieve optimal spectral efficiency, higher-order modulation techniques like the quadrature amplitude modulation (QAM) family (e.g., hexagonal QAM) are gaining increased attention due to their superior power and bandwidth efficiency. Moreover, cooperative relaying has become a key area of focus in both current and future wireless systems for its ability to enhance coverage and link capacity. It has been considered in standards like IEEE 802.16j/m, 3GPP LTE-Advanced, and is seen as a promising solution for 5G and beyond systems [29]. To realize the vision of green communication, EH enables wireless nodes to capture energy from ambient sources, such as RF signals, reducing reliance on traditional power sources and extending the lifespan of battery-operated devices. Integrating NOMA with EH capabilities facilitates the design of a spectral and energy-efficient wireless system. Additionally, BC and SR technologies enable ultra-low-power communication by utilizing existing signals, while promoting mutual benefits among devices through shared resources, ultimately enhancing both energy and spectral efficiency in future IoT networks.

In practice, hardware suffers from various kinds of impairments that affect performance and play an important role in the design of practical communication systems. Further, perfect knowledge of CSI at receiving nodes is hardly available in practice. This leads to CEE, which has a significant detrimental impact on the system's performance. Thus, the impact of the CEE must be investigated for realistic system design. While moving towards 5G and beyond systems, with the increased multimedia applications through wireless channels, the bandwidth requirement has increased. Furthermore, imperfection in SIC in decoding of NOMA users also affects the performance of NOMA system.

Therefore, performance analysis of spectral and energy-efficient next-generation wireless technologies, such as NOMA, cooperative relaying, EH, and backscatter-aided systems, under practical constraints like imperfect CSI, transceiver HI, and imperfect SIC, is crucial for designing practical communication systems for beyond 5G/6G. The objective of this thesis is to address various challenges in practical wireless communication systems and enhance their performance, rather than relying solely on extensive Monte Carlo simulations

1.10 Thesis Outline, Contributions

The thesis is organized into 7 chapters, which are briefly described below with their contributions. The flowchart of the thesis is shown in Figure 1.9 which shows the advancement of future wireless communication technology with their capability.

Chapter 1. Introduction : In chapter 1, a brief introduction to the wireless communication channel, multipath fading, channel characterization, various performance metrics, NOMA, cooperative relaying, energy harvesting, backscatter communication, symbiotic radio, hardware imperfections like imperfect CSI and transceiver hardware impairments, and finally, the motivation and major contributions of the work presented in the thesis are provided.

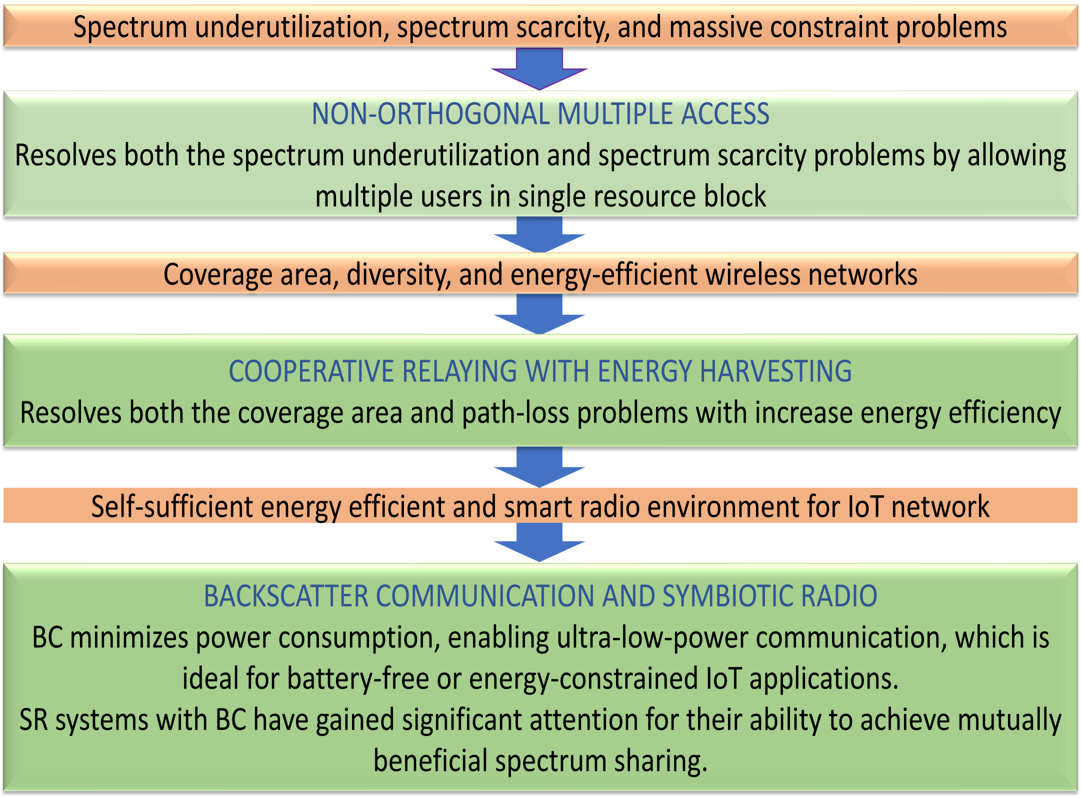

Figure 1.9: Flowchart of the thesis.

Chapter 2. Average Symbol Error Rate Analysis for NOMA Systems with Advanced Modulation Schemes: In this chapter, the performance of a downlink NOMA system over Nakagami-m fading channels is analyzed. The ASER of hexagonal quadrature amplitude modulation (HQAM) schemes by considering a two user NOMA pair is analyzed. Closed-form expressions for ASER of HQAM schemes for users are derived over generalized Nakagami-m fading channels. Further, for the HQAM constellation feasibility in two user downlink NOMA systems, the power allocation criterion for the users is presented. Furthermore, the impact of modulation order of the users over the systems ASER analysis is investigated and valuable insights are drawn.

Chapter 3. Average Symbol Error Rate with Multiple Feedback Based SIC for Multiuser NOMA Systems: This chapter investigates a novel multiple feedback-based SIC algorithm for an ultra-dense IoT device network. A multi-user uplink and downlink NOMA system is considered, and it is shown that the proposed algorithm outperforms conventional SIC. Further, the proposed algorithm's performance is analyzed under the practical case of imperfect CSI at the receiver node to validate the robustness. The computational complexity of multiple feedback SIC is compared with the conventional SIC.

Chapter 4. Performance Analysis of Energy Harvested Cooperative NOMA System: In this chapter, a EH-based multi-relay downlink cooperative NOMA system with practical constraints is considered. The base station serves NOMA users with the help of decode-and-forward based multiple EH relays, where relays harvest the energy from the base station's RF. A relay is selected from the multiple K-relays by using a partial relay selection protocol. The system is considered to operate in half-duplex mode over a generalized independent and identical Nakagami-m fading channel. The closed-form expression of outage probability and ergodic rate are derived for users, under the assumption of imperfect CSI and imperfect SIC at the receiver node. Expression of outage probability and ergodic rate for two users under the assumption of perfect CSI and perfect SIC are also presented. Further, the asymptotic expression for the outage probability is also shown.

Chapter 5. Performance Analysis of Backscatter Cooperative NOMA System: This chapter presents a NOMA-based coordinated direct and relay transmission system that utilizes a hybrid backscatter relay. The hybrid backscatter relay consists of passive information transmission via backscatter, EH, and active information reception. A novel and simple hybrid protocol is presented, where the relay operates in EH mode and active mode in the first phase, while in the second phase, the relay operates in passive mode. The chapter investigates the outage probability of the backscatter NOMA systems, considering realistic assumptions of nonlinear EH, channel estimation errors, and residual hardware impairments. Moreover, to gain deeper insights into the considered system, asymptotic outage probability, system throughput, and energy efficiency are derived.

Chapter 6. Performance of Backscatter-NOMA Systems: Symbiotic Communication for IoT Devices: In this chapter, a SR system tailored for IoT devices is presented, proposing an innovative framework that integrates backscatter-based IoT devices into the NOMA network. In this system, the primary base station uses NOMA principles to serve both near and far users simultaneously. The IoT network includes an IoT device equipped with a backscatter transmitter, which transmits its information over the primary signal, creating a symbiotic relationship between the two networks. The IoT transmitter not only serves the IoT receiver but also enhances the performance of the far user. This chapter provides a comprehensive analysis of the outage probabilities for both the NOMA and IoT networks. The outage probability of the far user is derived for scenarios with and without a direct link between the primary base station and the far user. The results clearly demonstrate a significant performance improvement over OMA techniques.

Chapter 7. Conclusions and Future Works: All the contributions of the thesis have been summarized in this chapter, and important insights and conclusions have been presented. Further, the scope for future works is also discussed.

Chapter 2

Average Symbol Error Rate of Higher Order Hexagonal-QAM Schemes for NOMA Systems

In this chapter, the performance of a downlink NOMA system over Nakagami-m fading channels is analyzed. This chapter presents a novel closed-form ASER analysis for HQAM-based NOMA under generalized Nakagami-m fading channels, addressing key limitations in existing studies that primarily focus on square QAM (SQAM). Unlike conventional SQAM, HQAM provides better power and spectral efficiency due to its hexagonal lattice structure, making it a promising modulation scheme for future NOMA systems. The key contributions of this chapter include the derivation of closed-form ASER expressions for HQAM-NOMA, a detailed investigation of power allocation strategies to minimize ASER, and an analysis of the impact of different modulation orders on system performance. Additionally, this work evaluates the feasibility of HQAM in practical two-user NOMA systems, providing key insights into its robustness under various fading conditions and power allocation scenarios. The findings demonstrate that HQAM outperforms SQAM in terms of error resilience, further establishing its viability for spectral and energy-efficient NOMA-based communication systems.

2.1 Introduction

NOMA is recognized as a promising technology for beyond 5G wireless communications with superior spectrum efficiency, user fairness, and high connectivity [6, 30–32]. Hence, applications like IoT, unmanned aerial vehicles (UAV), and satellite communication focus on integrating NOMA for future deployments [33–37]. On the other hand, use of energy and bandwidth-efficient QAM schemes have gained enormous research interest for beyond 5G communication systems [2, 38]. The family of QAM schemes includes square QAM (SQAM), rectangle QAM (RQAM), cross QAM (XQAM) and HQAM. SQAM scheme is used to transmit an even number of bits, e.g. 4, 16, 64, 256, 1024, 4096, and so on and usually takes a perfect square shape also refer as QAM scheme. SQAM has the maximum possible minimum Euclidean distance between the constellation points for a given average symbol power and requires a simple maximum likelihood detection technique [2]. For example, the 16-SQAM constellations is shown in Figure 2.1. RQAM scheme is used to transmit an odd number of bits, which includes SQAM, quadrature phase shift key, binary phase shift key and multilevel amplitude shift keying schemes as special cases [39]. However, RQAM scheme is inappropriate because of its high average and peak powers. An improved XQAM scheme is prefered over RQAM schme because of the lower peak to average energy than RQAM. The research for an energy-efficient modulation technique with high data-rate has directed us towards an optimum two-dimensional (2D) hexagonal-shaped constellation namely HQAM. Among the available QAM schemes, the HQAM scheme has a relatively low peak-to-average power ratio (PAPR), considerable SNR gain over the other QAM schemes, and a more spectral and power-efficient constellation due to its densest 2D packing [40]. Therefore, to achieve high target data rates with limited power and bandwidth, HQAM scheme can be adopted in multiple wireless applications for beyond 5G communication, such as multiple-antenna systems, physical-layer network coding, small cell, optical communications, and advanced channel coding [2]. HQAM constellations are further categorized into regular and irregular HQAM, based on the placement of the constellation points. Regular HQAM has high power efficiency or BER performance for larger values of modulation order with simpler detection. The irregular HQAM

M	SQAM		Regular HQAM		Irregular HQAM	
	E_{avg}	PAPR	E_{avg}	PAPR	E_{avg}	PAPR
4	2	1	2	1.5	2	1.5
8	-	-	4.5	1.55	4.321	2.13
16	10	1.8	9	2.11	8.75	1.74
32	-	-	17.75	2.08	17.59	1.879
64	42	2.33	37	2.51	35.22	1.90
128	-	-	72	2.347	70.56	1.96
256	170	2.647	149	2.74	141.23	2.03

Table 2.1: Comparison of various QAM schemes [2].

provides improved power efficiency and optimum performance, however, at the cost of increased detection complexity. The constellation points of irregular 4-HQAM and 16-HQAM with hexagonal decision boundaries are shown in Figure 2.2. Results of a comparative study between SQAM, regular HQAM, and irregular HQAM schemes for different constellation orders are shown in Table 2.1. Table 2.1 presents the average constellation energy or power (E_{avg}) and PAPR for the different constellations. From the table, it is observed that irregular HQAM has the reduced peak and average energies or power for all the constellation orders. Hence, HQAM is the most energy or power efficient constellation and can be concluded as the optimum constellation which provides better performance than the other constellations [2].

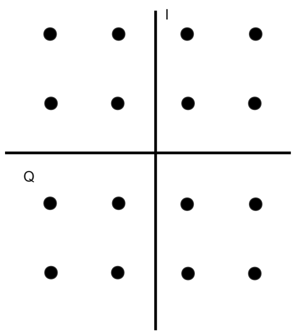

Figure 2.1: 16-SQAM constellation.

The error rate analysis of downlink NOMA using the SIC technique has received considerable attention by the research community recently [41–46]. In [41], the authors derived the exact BER for NOMA over Nakagami-m using quadrature phase shift key (QPSK). In [42], the authors analyzed the NOMA system considering symbol level SIC and derived closed-form expression of SER using M-ary QAM. In [43], the authors derived the pairwise error probability expression of downlink NOMA considering the symbol-level SIC. In [45], the authors considered a coordinated relay NOMA system and derived the closed-form expression of ASER using SQAM scheme over the Rayleigh fading channel. The authors in [46] consider a NOMA system with an arbitrary number of users and modulation order for SQAM scheme over the Rayleigh faded channel.

In NOMA, users are served in the same resource block, resulting in inter-user interference, which degrades users' performance. Thus, power allocation plays a critical role in minimizing the system's error rate. The analysis of power assignment is carried out in [41, 42, 47, 48]. In [41], the authors derived the power constraint such that the average BER of users is minimized. The power constraints in [42, 47, 48] are obtained such that the overlapping of the constellation of users is minimized. In [41], the authors considered a NOMA system and derived the power constrain using SQAM scheme with arbitrary modulation order. In [48], the authors consider a NOMA system and derive the power range using RQAM scheme. The error rate analysis of the NOMA system is already available in the open literature; however, the analysis is valid only for SQAM and RQAM scheme.

Contributions

As HQAM is a power and bandwidth-efficient modulation scheme compared to the existing QAM schemes and with NOMA systems being spectrum efficient, they are envisioned as solutions for beyond 5G communication. Hence, analysis of HQAM over NOMA systems is highly motivated for futuristic communications in attaining multi-rate power and spectrum efficient communications. To the best of the author's knowledge, the generalized analysis considering HQAM schemes in the NOMA system over Nakagami-m fading channel is not available in the literature, and for the first time, a framework to bridge this gap is presented. The main contributions are as follow

- A NOMA system is considered to unify the study of ASER analysis of M-ary HQAM schemes over Nakagami-m fading channels.

- A condition on power allocation coefficients is provided for the design of feasible HQAM constellations. The impact of power allocation coefficients on user's ASERs is investigated.

- The ASER performance of M-ary HQAM for the NOMA system is compared with the OMA system. The ASER performance of the HQAM scheme is also compared with an equivalent SQAM scheme, and useful insights are drawn from the same.

2.2 System Model

A downlink NOMA system is considered with a base station (BS) as a source of information and two users denoted as UE_1 and UE_2. It is considered that the BS serves only two users in one resource block due to the presence of error propagation in the SIC layer, high complexity and challenges in practical implementation with multiple users. The analysis can be generalized to serve the very number of users using hybrid TDMA NOMA. Where all users are divided into pairs, and each pair is allocated an orthogonal time block [49]. All the nodes are equipped with a single antenna each, and the link between BS and users experiences an independent and identically Nakagami-m distributed fading channel with m as the shape parameter. The channel coefficient corresponding to user links in the system are denoted by $h_{b,i}$, $i \in \{1, 2\}$, where $i = 1$ corresponds to UE_1, and $i = 2$ corresponds to UE_2 with fading parameter m_i and mean power $\mathbb{E}[|h_{b,i}|^2] = \Omega_i$. Without loss of generality, it is assumed that $|h_{b,1}|^2 > |h_{b,2}|^2$. The BS transmits the superimposed NOMA signal to users given as

$$x = \sqrt{\frac{Pa_1}{\mathrm{E}_{avg,1}}}x_1 + \sqrt{\frac{Pa_2}{\mathrm{E}_{avg,2}}}x_2, \tag{2.1}$$

in which P indicates total transmit power from BS, x_1 and x_2 denote complex modulated symbols of UE_1 and UE_2. The power allocation coefficients are a_1 and a_2, with $a_1 + a_2 = 1$. Further, it is assumed that the data symbols x_1 and x_2 are modulated with M_1-ary HQAM and M_2-ary HQAM respectively. $\mathrm{E_{avg,1}}$ and $\mathrm{E_{avg,2}}$ are the average constellation energy of M_1-ary and M_2-ary HQAM respectively. In a Cartesian coordinate plane, the HQAM symbol of the user is given as $x_i = A_I^i + jA_Q^i$, where $j = \sqrt{-1}$, A_I^i and A_Q^i are the I/Q components of a HQAM symbol. Consider an example for the resultant superimposed NOMA constellation for $M_1 = 16$, $M_2 =$

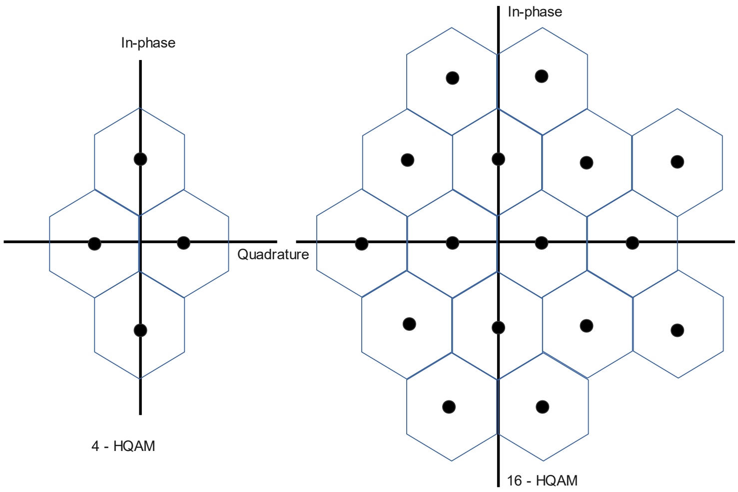

Figure 2.2: 4-HQAM and 16-HQAM constellation

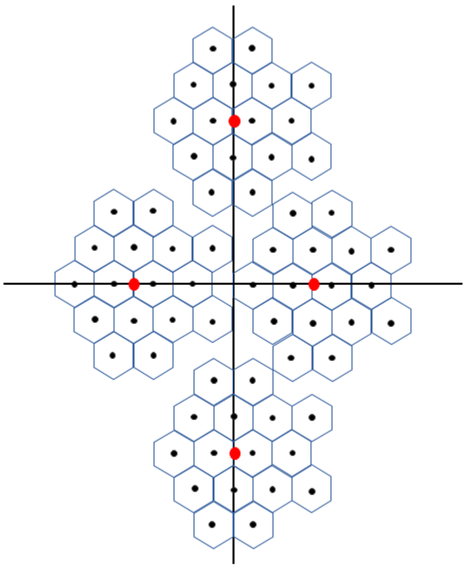

Figure 2.3: Superimposed constellation of UE_1 and UE_2 at transmitter.

4 given in Figure 2.3. The received superimposed signal at UE_1 and UE_2 is given as

$$y_i = h_{b,i}\left(\sqrt{\frac{Pa_1}{\mathrm{E}_{\mathrm{avg},1}}}x_1 + \sqrt{\frac{Pa_2}{\mathrm{E}_{\mathrm{avg},2}}}x_2\right) + z_{n,i}, i \in \{1,2\}, \tag{2.2}$$

in which $z_{n,i} \sim \mathcal{CN}(0, \sigma_0^2)$ represent the AWGN. In this work, since the fixed power allocation is considered ($a_2 > a_1$), the UE_1 performs SIC to obtain the symbol x_1 intended for UE_1. Thus, the SNR at UE_1 to detect its own message is given as

$$\gamma_{1,1} = \frac{|h_{b,1}|^2 Pa_1}{\sigma_0^2}. \tag{2.3}$$

Considering that UE_1 can decode UE_2 symbols, the signal-to-interference noise ratio (SINR) to detect x_2 is given as

$$\gamma_{1,2} = \frac{|h_{b,1}|^2 Pa_2}{|h_{b,1}|^2 Pa_1 + \sigma_0^2}. \tag{2.4}$$

The UE_2 decodes its own message in the presence of interference, the SINR is given as

$$\gamma_{2,2} = \frac{|h_{b,2}|^2 Pa_2}{|h_{b,2}|^2 Pa_1 + \sigma_0^2}. \tag{2.5}$$

2.3 Power Allocation Criteria

In this section, the power allocation criteria is derived for the downlink NOMA system using the generalized representation of the constellation point of HQAM. In NOMA, power allocation plays a crucial role in determining the system's performance. The power allocation criteria minimizes the error rate by enabling the SIC receiver to decode the signal without overlapping of constellation points. For practicable HQAM constellation of NOMA system, the feasible condition for QAM constellation is given as [42]

$$C_2 > A_I^1, C_2 > A_Q^1 \Longrightarrow C_2 > \max\left(A_I^1, A_Q^1\right)$$

$$C_2 > \max\left(\max\left(A_I^1\right), \max\left(A_Q^1\right)\right), \tag{2.6}$$

in which $C_1 = \sqrt{\frac{Pa_1}{\mathrm{E}_{avg,1}}}$ and $C_2 = \sqrt{\frac{Pa_2}{\mathrm{E}_{avg,2}}}$. For HQAM, $A_I^1 = (2k_i - 1)\,\frac{1}{2}C_1,\ k_i = 1, \ldots, 2K$ and $A_Q^1 = (2k_q - 1)\,\frac{\sqrt{3}}{2}C_1,\ k_q = 1, \ldots, K$, where $K = \sqrt{\frac{M_1}{4}}$ [50]. On substituting C_1, C_2, A_I^1 and A_Q^1 in (2.6), the following expression is obtained

$$\sqrt{\frac{Pa_2}{\mathrm{E}_{\mathrm{avg},2}}} > \sqrt{\frac{Pa_1}{\mathrm{E}_{\mathrm{avg},1}}}\left(4\sqrt{\frac{M_1}{4}} - 1\right)\frac{1}{2}. \tag{2.7}$$

After some simplifications, the power allocation coefficients must satisfy the following condition.

$$\frac{a_2}{a_1} > \frac{\mathrm{E}_{\mathrm{avg},2}}{4\mathrm{E}_{\mathrm{avg},1}}\left(4\sqrt{\frac{M_1}{4}} - 1\right)^2, \tag{2.8}$$

2.4 ASER Analysis

In this section, the ASER expressions of UE_1 and UE_2 are derived for HQAM. The generalized ASER expression for a digital modulation scheme using CDF based approach is given as [38, 51, 52]

$$P_{s,i}(e) = -\int_0^\infty P_s^{'}(e|\lambda) F_{\lambda_i}(\lambda) d\lambda, \tag{2.9}$$

in which $F_{\lambda_i}(\lambda)$ is the CDF of the instantaneous SNR of the users received signals and $P_s^{'}(e|\lambda)$ is the first-order derivative of the conditional symbol error probability (SEP) of HQAM scheme in AWGN channel with respect to (w.r.t) instantaneous SNR (λ). For M-ary HQAM scheme, the conditional SER expression over AWGN channels is given as [38]

$$P_s\left(e/\lambda\right) = W\mathrm{Q}\left(\sqrt{\alpha\lambda}\right) + \frac{2}{3}W_c\mathrm{Q}^2\left(\sqrt{2\alpha\lambda/3}\right) - 2W_c\mathrm{Q}\left(\sqrt{\alpha\lambda}\right)\mathrm{Q}\left(\sqrt{\alpha\lambda/3}\right), \tag{2.10}$$

in which the values of the parameters W, W_c and α for different constellations are given in Table 2.2. Using the identities $\mathrm{Q}\left(x\right) = 1/2\left(1 - \ \mathrm{erf}\left(\frac{x}{\sqrt{2}}\right)\right)$ and using [53,

	Regular HQAM			Irregular HQAM		
M	α	W	W_c	α	W	W_c
4	1	5/2	3/2	1	5/2	3/2
8	2/5	7/2	21/8	32/69	7/2	21/8
16	2/9	33/8	27/8	8/35	33/8	27/8
32	8/71	75/16	33/8	512/4503	75/16	33/8
64	2/37	161/32	147/32	8/141	163/32	75/16

Table 2.2: Various value of α, W, W_c for different regular and irregular HQAM constellation [2].

eq. (7.1.21)], the first order derivative of SEP w.r.t λ is given as

$$\begin{aligned} P_s^{'}\left(e/\lambda\right) =& \frac{1}{2}\sqrt{\frac{\alpha}{2\pi}}\left[W_c - W\right]\lambda^{-\frac{1}{2}}e^{-\frac{\alpha}{2}\lambda} - \frac{W_c}{3}\sqrt{\frac{\alpha}{3\pi}}\lambda^{-\frac{1}{2}}e^{-\frac{\alpha}{3}\lambda} + \frac{W_c}{2}\sqrt{\frac{\alpha}{6\pi}}\lambda^{-\frac{1}{2}}e^{-\frac{\alpha}{6}\lambda} \\ &+ \frac{2W_c\alpha}{9\pi}e^{-\frac{2\alpha}{3}\lambda}{}_1F_1\left(1;\frac{3}{2};\frac{\alpha}{3}\lambda\right) - \left({}_1F_1\left(1;\frac{3}{2};\frac{\alpha}{2}\lambda\right) + {}_1F_1\left(1;\frac{3}{2};\frac{\alpha}{6}\lambda\right)\right) \\ &\times \frac{W_c\alpha}{2\sqrt{3}\pi}e^{-\frac{2\alpha}{3}\lambda}. \end{aligned} \tag{2.11}$$

2.4.1 ASER analysis of near user

On considering perfect SIC at UE_1, the CDF of received SNR is given by

$$F_{\lambda_1}(\lambda) = \frac{\gamma\left(m_1, \frac{m_1\lambda}{a_1\rho\Omega_1}\right)}{\Gamma(m_1)}. \tag{2.12}$$

The generalized closed-form ASER expression of M-ary HQAM of UE_1 is obtained by substituting the $F_{\lambda_1}(\lambda)$ and the first-order derivative of the conditional SEP (2.11) in (2.9), the following expression is obtained

$$\begin{aligned} P_{s,1}(e) =& -\int_0^\infty \left(\frac{1}{2}\sqrt{\frac{\alpha}{2\pi}}\left[W_c - W\right]\lambda^{-\frac{1}{2}}e^{-\frac{\alpha}{2}\lambda} - \frac{W_c}{3}\sqrt{\frac{\alpha}{3\pi}}\lambda^{-\frac{1}{2}}e^{-\frac{\alpha}{3}\lambda}\right. \\ &+ \frac{W_c}{2}\sqrt{\frac{\alpha}{6\pi}}\lambda^{-\frac{1}{2}}e^{-\frac{\alpha}{6}\lambda} + \frac{2W_c\alpha}{9\pi}e^{-\frac{2\alpha}{3}\lambda}{}_1F_1\left(1;\frac{3}{2};\frac{\alpha}{3}\lambda\right) - \frac{W_c\alpha}{2\sqrt{3}\pi}e^{-\frac{2\alpha}{3}\lambda} \\ &\times \left.\left({}_1F_1\left(1;\frac{3}{2};\frac{\alpha}{2}\lambda\right) + {}_1F_1\left(1;\frac{3}{2};\frac{\alpha}{6}\lambda\right)\right)\right)\frac{\gamma\left(m_1, \frac{m_1\lambda}{a_1\rho\Omega_1}\right)}{\Gamma(m_1)}d\lambda. \end{aligned} \tag{2.13}$$

Integer valued fading parameter

For the integer-valued fading parameter, The ASER expression of UE_1 is obtained by solving required integration's with the help of [54, eq. (6.455.2), (7.522.9), (8.352.1)], the ASER expression is given as

$$\begin{aligned}
P_{s,1,i}(e) =& -\frac{1}{2}\sqrt{\frac{\alpha}{2\pi}}\frac{[W_c - W]}{\Gamma(m_1)}\mathbb{A}_1\left(\frac{m_1}{a_1\rho\Omega_1}, \frac{\alpha}{2}\right) + \sqrt{\frac{\alpha}{3\pi}}\frac{W_c}{3\Gamma(m_1)}\mathbb{A}_1\left(\frac{m_1}{a_1\rho\Omega_1}, \frac{\alpha}{3}\right) \\
&+ \mathbb{A}_1\left(\frac{m_1}{a_1\rho\Omega_1}, \frac{\alpha}{6}\right)\sqrt{\frac{\alpha}{6\pi}}\frac{W_c}{2\Gamma(m_1)} + \frac{\alpha W_c}{9\pi}\left[\mathbb{A}_2\left(1, \frac{2\alpha}{3}, \frac{\alpha}{3}\right) - \sum_{q=0}^{m_1-1}\left(\frac{m_1}{a_1\rho\Omega_1}\right)^q\right. \\
&\left.\times \frac{1}{q!}\mathbb{A}_2\left(q+1, \left(\frac{2\alpha}{3} + \frac{m_1}{a_1\rho\Omega_1}\right), \frac{\alpha}{3}\right)\right] + \frac{\alpha}{2\sqrt{3}\pi}W_c\left(\left[\mathbb{A}_2\left(1, \frac{2\alpha}{3}, \frac{\alpha}{2}\right) - \right.\right. \\
&\left.\sum_{q=0}^{m_1-1}\left(\frac{m_1}{a_1\rho\Omega_1}\right)^q\frac{1}{q!}\mathbb{A}_2\left(q+1, \frac{2\alpha}{3} + \frac{m_1}{a_1\rho\Omega_1}, \frac{\alpha}{2}\right)\right] + \left[\mathbb{A}_2\left(1, \frac{2\alpha}{3}, \frac{\alpha}{6}\right)\right. \\
&\left.\left. - \sum_{q=0}^{m_1-1}\left(\frac{m_1}{a_1\rho\Omega_1}\right)^q\mathbb{A}_2\left(q+1, \frac{2\alpha}{3} + \frac{m_1}{a_1\rho\Omega_1}\right)\right]\right),
\end{aligned} \tag{2.14}$$

in which $\rho = \frac{P}{\sigma_0^2}$, $\mathbb{A}_1(u, \varrho) = \frac{u^{m_1}\Gamma\left(\frac{1}{2}+m_1\right)}{m_1(u+\varrho)^{m_1+\frac{1}{2}}}\,{}_2F_1\left(1, \frac{1}{2}+m_3; m_1+1; \frac{u}{u+\varrho}\right)$ and $\mathbb{A}_2(a_1, b_1, c_1) = \Gamma(a_1)b_1^{a_1}\,{}_2F_1(1, a_1; \frac{3}{2}; \frac{c_1}{b_1})$.

Non-integer valued fading parameter

For the non-integer valued fading parameter, the CDF of the Nakagami-m distributed link can be expanded as an infinite series representation [55, eq. 31]. Solving required integration's with the help of [54, eq. (6.455.2), (7.522.9)], ASER expression for the general order HQAM scheme for non-integer value of fading parameter is given as

$$\begin{aligned}
P_{s,1,n}(e) =& -\frac{1}{2}\sqrt{\frac{\alpha}{2\pi}}\frac{[W_c - W]}{\Gamma(m_1)}\mathbb{A}_1\left(\frac{m_1}{a_1\rho\Omega_1}, \frac{\alpha}{2}\right) + \sqrt{\frac{\alpha}{3\pi}}\frac{W_c}{3\Gamma(m_1)}\mathbb{A}_1\left(\frac{m_1}{a_1\rho\Omega_1}, \frac{\alpha}{3}\right) \\
&+ \mathbb{A}_1\left(\frac{m_1}{a_1\rho\Omega_1}, \frac{\alpha}{6}\right)\sqrt{\frac{\alpha}{6\pi}}\frac{W_c}{2\Gamma(m_1)} + \frac{\alpha W_c}{9\pi}\left[\sum_{q=0}^{\infty}\left(\frac{2\alpha}{3} + \frac{m_1}{a_1\rho\Omega_1}\right)^{-(m_1+q+1)}\right. \\
&\left.\left(\frac{m_1}{a_1\rho\Omega_1}\right)^{m_1+q}{}_2F_1\left(1, m_1+q+1; 1.5; \frac{a_1\rho\Omega_1\alpha}{2\alpha a_1\rho\Omega_1 + 3m_1}\right)\right] + \frac{W_c\alpha}{2\sqrt{3}\pi}
\end{aligned}$$

$$\left(\left[\sum_{q=0}^{\infty} {}_2F_1\left(1, m_1+n+1; 1.5; \frac{\alpha 3 a_1 \rho \Omega_1}{2\left(2\alpha a_1 \rho \Omega_1 + 3m_1\right)}\right)\right]\left(\frac{m_1}{a_1\rho\Omega_1}\right)^{q+m_1}\right.$$
$$\left(\frac{2\alpha}{3}+\frac{m_1}{a_1\rho\Omega_1}\right)^{-(m_1+q+1)} + \left[\sum_{q=0}^{m_1-1}\left(\frac{2\alpha}{3}+\frac{m_1}{a_1\rho\Omega_1}\right)^{-(m_1+q+1)}\left(\frac{m_1}{a_1\rho\Omega_1}\right)^{q+m_1}\right.$$
$$\left.\left. {}_2F_1\left(1, m_1+q+1; 1.5; \frac{\alpha 3 a_1 \rho \Omega_1}{6\left(2\alpha a_1 \rho \Omega_1 + 3m_1\right)}\right)\right]\right). \tag{2.15}$$

2.4.2 ASER analysis of far user

The CDF of the received signal instantaneous SNR at UE_2 can be written as [56]

$$F_{\lambda_2}(\lambda) = \begin{cases} \frac{\gamma\left(m_2, \frac{m_2\lambda}{(a_2-a_1\lambda)\rho\Omega_2}\right)}{\Gamma(m_2)}, & \text{if } \lambda < \frac{a_2}{a_1} \\ 1, & \text{otherwise.} \end{cases} \tag{2.16}$$

The closed form expression of far user is obtained as follows. Substitute $F_{\lambda_2}(\lambda)$ and (2.11) in (2.9) the following expression is obtained

$$P_{s,2}(e) = -\int_0^{\frac{a_2}{a_1}} \left(\frac{1}{2}\sqrt{\frac{\alpha}{2\pi}}[W_c - W]\lambda^{-\frac{1}{2}}e^{-\frac{\alpha}{2}\lambda} - \frac{W_c}{3}\sqrt{\frac{\alpha}{3\pi}}\lambda^{-\frac{1}{2}}e^{-\frac{\alpha}{3}\lambda} + \frac{W_c}{2}\sqrt{\frac{\alpha}{6\pi}}\lambda^{-\frac{1}{2}}e^{-\frac{\alpha}{6}\lambda}\right.$$
$$\left. + \frac{2W_c\alpha}{9\pi}e^{-\frac{2\alpha}{3}\lambda}{}_1F_1\left(1;\frac{3}{2};\frac{\alpha}{3}\lambda\right) - \left[{}_1F_1\left(1;\frac{3}{2};\frac{\alpha}{2}\lambda\right) + {}_1F_1\left(1;\frac{3}{2};\frac{\alpha}{6}\lambda\right)\right]\right)$$
$$\times \frac{W_c\alpha}{2\sqrt{3}\pi}e^{-\frac{2\alpha}{3}\lambda}\frac{\gamma\left(m_2, \frac{m_2\lambda}{(a_2-a_1\lambda)\rho\Omega_2}\right)}{\Gamma(m_2)}d\lambda. \tag{2.17}$$

The (2.17) can further expressed as

$$P_{s,2}(e) = \frac{1}{2}\sqrt{\frac{\alpha}{2\pi}}\frac{W_c - W}{\Gamma(m_2)}\int_{\lambda=0}^{\frac{a_2}{a_1}}\lambda^{-\frac{1}{2}}e^{-\frac{\alpha\lambda}{2}}\gamma\left(m_2, \frac{m_2\lambda}{(a_2-a_1\lambda)\rho\Omega_2}\right)d\lambda + \sqrt{\frac{\alpha}{3\pi}}\frac{W_c}{3\Gamma(m_2)}$$
$$\int_{\lambda=0}^{\frac{a_2}{a_1}}\lambda^{-\frac{1}{2}}\gamma\left(m_2, \frac{m_2\lambda}{(a_2-a_1\lambda)\rho\Omega_2}\right)e^{-\frac{\alpha\lambda}{3}}d\lambda + \frac{W_c}{2\Gamma(m_2)}\sqrt{\frac{\alpha}{6\pi}}\int_{\lambda=0}^{\frac{a_2}{a_1}}\lambda^{-\frac{1}{2}}$$
$$\gamma\left(m_2, \frac{m_2\lambda}{(a_2-a_1\lambda)\rho\Omega_2}\right)e^{-\frac{\alpha\lambda}{3}}d\lambda + \frac{2W_c\alpha}{9\pi}\int_{\lambda=0}^{\frac{a_2}{a_1}}e^{-\frac{2\alpha\lambda}{3}}{}_1F_1\left(1;1.5;\frac{\alpha\lambda}{3}\right)$$
$$\gamma\left(m_2, \frac{m_2\lambda}{(a_2-a_1\lambda)\rho\Omega_2}\right)d\lambda + \int_{\lambda=0}^{\frac{a_2}{a_1}}\left[{}_1F_1\left(1;1.5;\frac{\alpha\lambda}{2}\right) + {}_1F_1\left(1;1.5;\frac{\alpha\lambda}{6}\right)\right]$$
$$\frac{W_c\alpha}{2\sqrt{3}\pi}e^{-\frac{2\alpha\lambda}{3}}\gamma\left(m_2, \frac{m_2\lambda}{(a_2-a_1\lambda)\rho\Omega_2}\right)d\lambda. \tag{2.18}$$

By substituting $\lambda = \frac{1}{2}\frac{a_2}{a_1}(1+v)$ and changing the integration limit accordingly, the integral in (2.18) reduces to

$$
\begin{aligned}
P_{s,2}(e) =& \sqrt{\frac{\alpha}{2\pi}}\frac{[W_c - W]}{2\Gamma(m_2)}\sqrt{\frac{a_2}{2a_1}}\int_{v=-1}^{1}\frac{1}{\sqrt{1+v}}e^{-\frac{\alpha a_2}{4a_1}(1+v)}\gamma\left(m_2, \frac{m_2(1+v)}{a_1(1-v)\rho\Omega_2}\right)dv \\
&+\sqrt{\frac{\alpha}{3\pi}}\frac{W_c}{3\Gamma(m_2)}\sqrt{\frac{a_2}{2a_1}}\int_{v=-1}^{1}\frac{1}{\sqrt{1+v}}e^{-\frac{\alpha a_2}{6a_1}(1+v)}\gamma\left(m_2, \frac{m_2(1+v)}{a_1(1-v)\rho\Omega_2}\right)dv \\
&+\sqrt{\frac{\alpha}{6\pi}}\frac{W_c}{2\Gamma(m_2)}\sqrt{\frac{a_2}{2a_1}}\int_{v=-1}^{1}\frac{1}{\sqrt{1+v}}e^{-\frac{\alpha a_2}{12a_1}(1+v)}\gamma\left(m_2, \frac{m_2(1+v)}{a_1(1-v)\rho\Omega_2}\right)dv \\
&+\frac{2W_c\alpha}{9n\Gamma(m_2)}\frac{a_2}{2a_1}\int_{v=-1}^{1}{}_1F_1\left(1;1.5;\frac{\alpha a_2(1+v)}{6a_1}\right)e^{-\frac{2\alpha a_2}{6a_1}(1+v)}dv \\
&+\frac{\alpha W_c}{2\sqrt{3}\pi\Gamma(m_2)}\frac{a_2}{2a_1}\int_{v=-1}^{1}e^{-\frac{2\alpha a_2}{6a_1}(1+v)}\left[{}_1F_1\left(1;1.5;\frac{\alpha a_2(1+v)}{4a_1}\right)\right. \\
&\left.+{}_1F_1\left(1;1.5;\frac{\alpha a_2(1+v)}{12a_1}\right)\right]dv, \qquad (2.19)
\end{aligned}
$$

after some simplification, the following expression is obtained

$$
\begin{aligned}
P_{s,2}(e) =& \sqrt{\frac{\alpha}{2\pi}}\frac{[W_c - W]}{2\Gamma(m_2)}\sqrt{\frac{a_2}{2a_1}}\int_{v=-1}^{1}\frac{\sqrt{1-v}}{\sqrt{1-v^2}}e^{-\frac{\alpha a_2}{4a_1}(1+v)}\gamma\left(m_2, \frac{m_2(1+v)}{a_1(1-v)\rho\Omega_2}\right)dv \\
&+\sqrt{\frac{\alpha}{3\pi}}\frac{W_c}{3\Gamma(m_2)}\sqrt{\frac{a_2}{2a_1}}\int_{v=-1}^{1}\frac{\sqrt{1-v}}{\sqrt{1-v^2}}e^{-\frac{\alpha a_2}{6a_1}(1+v)}\gamma\left(m_2, \frac{m_2(1+v)}{a_1(1-v)\rho\Omega_2}\right)dv \\
&+\sqrt{\frac{\alpha}{6\pi}}\frac{W_c}{2\Gamma(m_2)}\sqrt{\frac{a_2}{2a_1}}\int_{v=-1}^{1}\frac{\sqrt{1-v}}{\sqrt{1-v^2}}e^{-\frac{\alpha a_2}{12a_1}(1+v)}\gamma\left(m_2, \frac{m_2(1+v)}{a_1(1-v)\rho\Omega_2}\right)dv \\
&+\frac{2W_c\alpha}{9n\Gamma(m_2)}\frac{a_2}{2a_1}\int_{v=-1}^{1}\frac{\sqrt{1-v^2}}{\sqrt{1-v^2}}{}_1F_1\left(1;1.5;\frac{\alpha a_2(1+v)}{6a_1}\right)e^{-\frac{2\alpha a_2}{6a_1}(1+v)}dv \\
&+\frac{\alpha W_c}{2\sqrt{3}\pi\Gamma(m_2)}\frac{a_2}{2a_1}\int_{v=-1}^{1}\frac{\sqrt{1-v^2}}{\sqrt{1-v^2}}e^{-\frac{2\alpha a_2}{6a_1}(1+v)} \\
&\times\left[{}_1F_1\left(1;1.5;\frac{\alpha a_2(1+v)}{4a_1}\right)+{}_1F_1\left(1;1.5;\frac{\alpha a_2(1+v)}{12a_1}\right)\right]dv. \qquad (2.20)
\end{aligned}
$$

The integral in (2.20) is challenging to solve. Thus, Gaussian-Chebyshev quadrature (GCQ) [57, eq. (8.8)] is applied to obtained an approximation for the integral. The GCQ is given as

$$
\int_{-1}^{1}\frac{f(v)}{\sqrt{(1-v^2)}}dv \approx \frac{\pi}{n}\sum_{k=1}^{n} f\left(\cos\left(\frac{(2k-1)\pi}{2n}\right)\right), \qquad (2.21)
$$

in which and without the indentation n is the complexity-accuracy trad-off parameter. By utilizing (2.21), the obtained generalized closed form ASER expression of

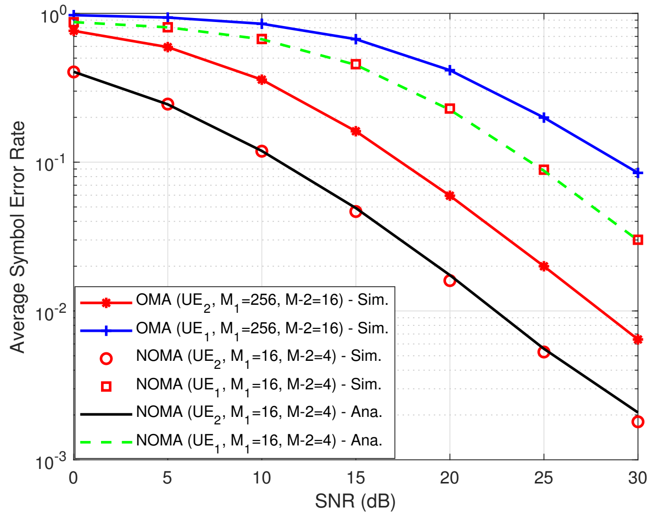

Figure 2.4: ASER of UE_1 and UE_2 w.r.t SNR for NOMA and OMA.

M-ary HQAM of UE_2 is given as

$$\begin{aligned}
P_{s,2}(e) \approx & \sqrt{\frac{\alpha}{2\pi}} \frac{[W_c - W]\pi}{2n\Gamma(m_2)} \sum_{k=1}^{n} \sqrt{1-v_k} e^{-\frac{\alpha a_2}{4a_1}(1+v_k)} \gamma\left(m_2, \frac{m_2(1+v_k)}{a_1(1-v_k)\rho\Omega_2}\right) \\
& + \sqrt{\frac{\alpha}{3\pi}} \sqrt{\frac{a_2}{2a_1}} \frac{W_c\pi}{3n\Gamma(m_2)} \sum_{k=1}^{n} \sqrt{1-v_k} e^{-\frac{\alpha a_2}{6a_1}(1+v_k)} \gamma\left(m_2, \frac{m_2(1+v_k)}{a_1(1-v_k)\rho\Omega_2}\right) \\
& + \sqrt{\frac{\alpha}{6\pi}} \sqrt{\frac{a_2}{2a_1}} \frac{W_c\pi}{2n} \frac{1}{\Gamma(m_2)} \sum_{k=1}^{n} \sqrt{1-v_k} e^{-\frac{\alpha a_2}{12a_1}(1+v_k)} \gamma\left(m_2, \frac{m_2(1+v_k)}{a_1(1-v_k)\rho\Omega_2}\right) \\
& + \frac{2\alpha W_c\pi}{9n\pi\Gamma(m_2)} \frac{a_2}{2a_1} \sum_{k=1}^{n} \sqrt{1-v_k^2} e^{-\frac{\alpha a_2}{3a_1}(1+v_k)} \gamma\left(m_2, \frac{m_2(1+v_k)}{a_1(1-v_k)\rho\Omega_2}\right) \\
& {}_1F_1\left(1; 1.5; \frac{\alpha a_2(1+v_k)}{6a_1}\right) + \frac{\alpha W_c}{2\sqrt{3}n\Gamma(m_2)} \frac{a_2}{2a_1} \sum_{k=1}^{n} \gamma\left(m_2, \frac{m_2(1+v_k)}{a_1(1-v_k)\rho\Omega_2}\right) \\
& \sqrt{1-v_k^2} e^{-\frac{\alpha a_2}{3a_1}(1+v_k)} \left[{}_1F_1\left(1; \frac{3}{2}; \frac{\alpha a_2(1+v_k)}{4a_1}\right) + {}_1F_1\left(1; \frac{3}{2}; \frac{\alpha a_2(1+v_k)}{12a_1}\right) \right],
\end{aligned} \tag{2.22}$$

in which $v_k = \cos\left(\frac{(2k-1)\pi}{2n}\right)$.

2.5 Numerical and Simulation Results

In this section, numerical and simulation results are presented. Unless specified, the system parameters are as follows: $a_1 = 0.1$, $n = 50$, $m_1 = 1$, $m_2 = 1$, $\Omega_1 = 2$ and $\Omega_2 = 1$. In the figures, 'Sim.' refers to simulation and 'Ana.' refers to analyt-

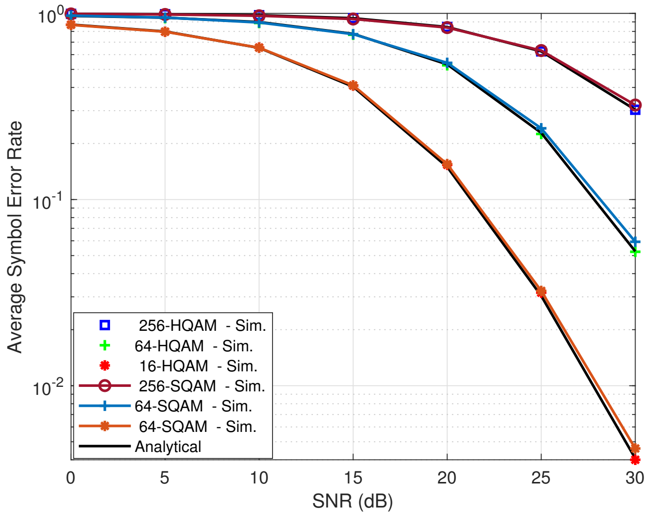

Figure 2.5: ASER of UE_1 w.r.t SNR for HQAM scheme and SQAM scheme.

ical results. The accuracy of the closed-form expressions is validated through the Monte-Carlo simulations.

Comparison of OMA and NOMA system

Figure 2.4 demonstrates superiority of the NOMA system over the OMA system. In this Figure, analytical and simulation results for ASER performance for HQAM for both the systems are presented w.r.t. the transmit SNR. For a fair comparison, the total bit rate of OMA and NOMA is considered to be equal. For example, when $M_1 = 16$ is employed for UE_1 and $M_2 = 4$ for UE_2 in the NOMA system during two transmission frames. For consistency in the data rate of the two systems i.e., $2\log_2 M_1 = 2\log_2 16 = \log_2 256 = 8$ bit per channel used (bpcu). Hence, in the corresponding OMA system, $M_1 = 256$ must be utilized for UE_1 in the first frame, and $M_2 = 16$ must be utilized for UE_2 in the second frame. It is observed that the ASER of both users in the NOMA system is much lower than its ASER in the OMA system. At ASER of 10^{-1}, NOMA system provides a gain of approximately 6 dB over OMA system for UE_2. Further, it is observed that the analytical ASER of both users matches the simulated ASER perfectly, which validates the derived expressions.

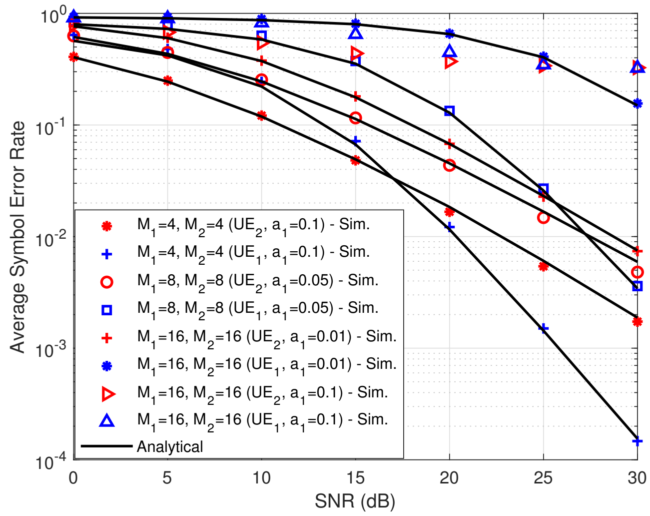

Figure 2.6: ASER of UE_1 and UE_2 w.r.t. SNR with same modulation orders ($M_1 = M_2$).

Comparison of SQAM and HQAM schemes

In Figure 2.5 comparison of SQAM and HQAM schemes is given for the considered NOMA system. Analytical and simulation results for ASER performance are presented for the constellation orders of $M_1 = 16$ and $M_2 = 4$. It is observed that at an ASER of 3.2×10^{-2}, 16−HQAM provides a gain of 0.4 dB over 16−SQAM. Further, it is observed that at an ASER of 3.3×10^{-1}, 256−HQAM provides a gain of 0.5 dB over 256−SQAM. The superiority of HQAM is due to its low peak and average energy compared to other QAM schemes. HQAM has an optimum 2D constellation with its densest 2D packing and is efficient even at high SNRs by providing SNR gains over the other QAM schemes. Further, from the results, it is confirm that the HQAM could be adopted in futuristic wireless communication because of its optimum 2D constellation, which is energy efficient than other QAM schemes [2].

Impact of power allocation criterion for a practicable HQAM

Figure 2.6 and Figure 2.7 show the ASER performance of user receivers plotted with respect to SNR with different value of a_1. In Figure 2.6 results are presented for the same modulation orders ($M_1 = M_2$). The channel parameters are considered as $m_1 = 2$, $m_2 = 1$. The results also corroborates the power allocation criterion

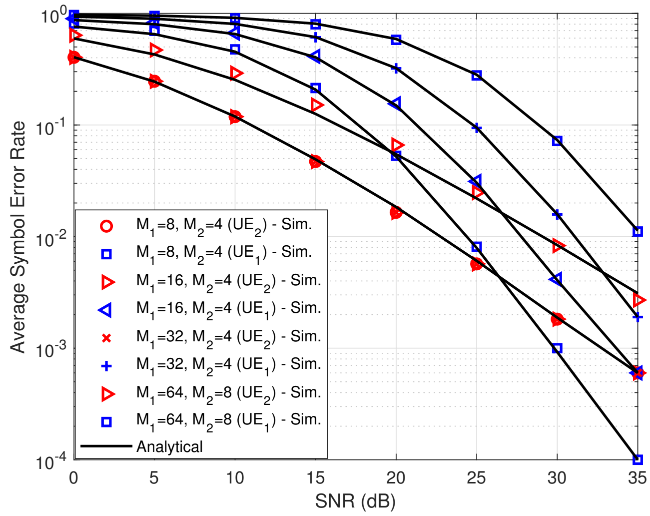

Figure 2.7: ASER of UE_1 and UE_2 w.r.t. SNR with different modulation orders ($M_1 \neq M_2$).

derived in (2.8). It is observed that the power allocation criterion must satisfy for proper decoding of a symbol. According to (2.8), the power allocation criterion for $M_1 = M_2 = 4$ is $\frac{a_2}{a_1} > 4.5$, $M_1 = M_2 = 8$ is $\frac{a_2}{a_1} > 5.42$, and $M_1 = M_2 = 16$ is $\frac{a_2}{a_1} > 12.25$. For the case $M_1 = M_2 = 4$ with $\frac{a_2}{a_1} = 9$, $M_1 = M_2 = 8$ with $\frac{a_2}{a_1} = 19$ and $M_1 = M_2 = 16$ with $\frac{a_2}{a_1} = 99$, the power criterion satisfies, and the ASER performance of both users decreases with SNR. For the case $M_1 = M_2 = 16$ with $a_1 = 0.1$, $\frac{a_2}{a_1} = 9$, the power criterion does not hold, and the ASER performance shows a constant error floor with the increase in SNR. Further, it is observed that for an ASER of 10^{-2} with $M_1 = M_2 = 4$ for the same power condition, UE_1 has an SNR gain of 2.5 dB over UE_2, due to the better channel condition. In Figure 2.7, results are presented for different modulation orders ($M_1 \neq M_2$) of users. In the case of $M_1 = 8, M_2 = 4$, and $M_1 = 16, M_2 = 4$, as the constellation order of UE_1 is changed, it is observed that the performance of UE_2 is unaffected. This is due to the consideration of power allocation criterion for a given case. It is observed that UE_1 with $M_1 = 16$ and $M_1 = 32$ need additional 3 dB SNR as compared to UE_1 with $M_1 = 8$ to achieve the ASER of 10^{-2}.

Impact of channel conditions over constellation orders

In Figure 2.8 and Figure 2.9, the ASER of UE_1 is plotted with respect to SNR for different fading parameters. In figure Figure 2.8, the ASER is plotted for integer

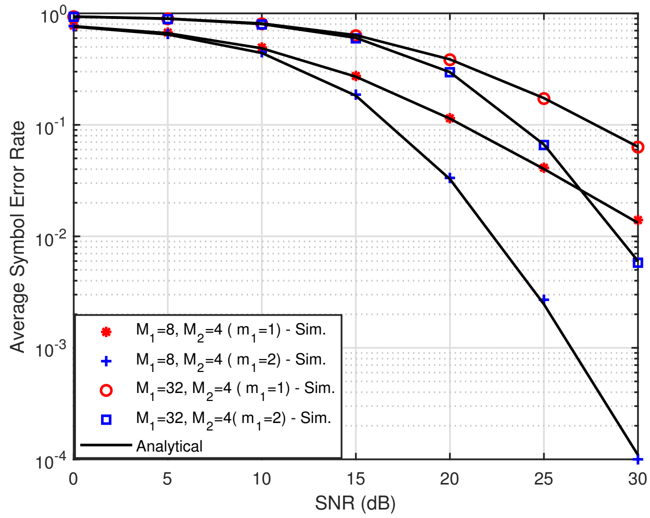

Figure 2.8: ASER of UE_1 w.r.t SNR with different integer fading parameter value (m)

valued fading parameter. It is observed that for $M_1 = 8$, at the ASER of 10^{-2}, UE_1 has a SNR gain of 6 dB by varying the fading parameter from $m_1 = 1$ to $m_1 = 2$. It is observed from the figure that at a high SNR value, the UE_1 with $M_1 = 32$ and $m_1 = 2$ performs better than $M_1 = 8$ and $m_1 = 1$. At SNR of 27 dB, UE_1 with $M_1 = 32$ and $m_1 = 2$ shows equal ASER performance as $M_1 = 8$ and $m_1 = 1$. And at ASER of $1.5 * 10^{-2}$, UE_1 with $M_1 = 32$ and $m_1 = 2$ provides an SNR gain of approximately 2 dB over $M_1 = 8$ and $m_1 = 1$. In Figure 2.9, the ASER is plotted for different non-integer fading parameters. Figure verify the ASER expression of UE_1 with non-integer fading parameter (2.15). It is observed that for $M_1 = 16$, at the ASER of 10^{-3}, UE_1 has a SNR gain of 5 dB by varying the fading parameter from $m_1 = 1.5$ to $m_1 = 2.5$. It is observed from the figure that at a high SNR value, the UE_1 with $M_1 = 16$ and $m_1 = 2.5$ performs better than $M_1 = 4$ and $m_1 = 1.5$. Thus higher constellation orders are highly preferred for high data rates for a fast communication when the channel conditions are good.

2.6 Summary

In this chapter, an analysis of the downlink NOMA system with two users is performed. Closed-form expressions for ASER of generalized M-ary HQAM for both the users are obtained. The ASER analysis is carried out using a symbol-level SIC

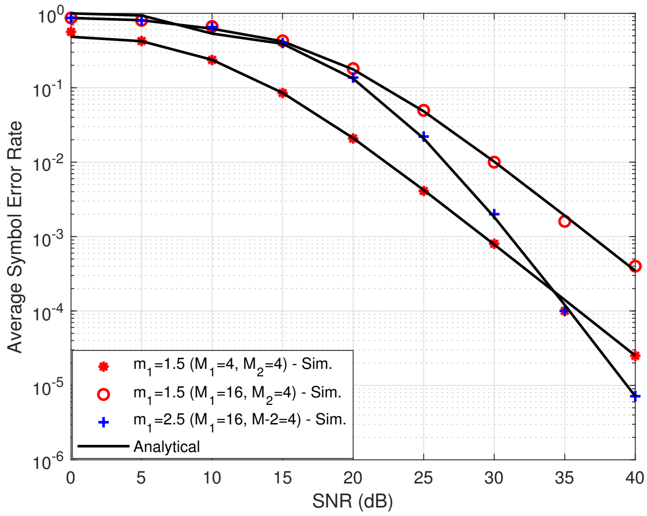

Figure 2.9: ASER of UE_1 w.r.t SNR with different non-integer fading parameter value (m)

detector. Based on the analytical results, it is shown that NOMA's performance is superior to OMA's performance for HQAM. Further, it is observed that at an ASER of HQAM provides a gain of 0.4 dB over SQAM scheme. For the feasibility of the HQAM constellation, the power allocation criterion is provided. It is shown that the proposed power allocation criteria for HQAM can avoid the error floor at high SNR, which can not be realized with arbitrary power allocation. Further, the impact of modulation orders on users with different channel conditions is analyzed. It is shown that users' ASER performance is unaltered with other user's constellation orders when the power allocation criterion is satisfied. To further analyze and enhance the performance of NOMA systems while achieving massive connectivity, the next chapter explores a multi-user NOMA system and proposes an algorithm to improve the overall system performance.

Chapter 3

Average Symbol Error Rate with Multiple Feedback Based SIC for Multiuser NOMA Systems

In the previous chapter, the significance of higher-order modulation schemes in the NOMA system is emphasized for power and spectral efficient transmissions to meet the needs of rocketing multi-media multi-data-rate high-speed communications in 5G and beyond. However, the analysis is confined to the two users of the NOMA system, and power allocation criteria are obtained for HQAM to remove the error floor and improve the performance of NOMA users. Thus, the impact of a multi-user in the NOMA system needs to be analyzed.

In this chapter, a novel multiple feedback-based SIC (MF-SIC) algorithm is investigated for an ultra-dense IoT device network. A multi-user downlink and uplink NOMA system is considered, and it is shown that the proposed algorithm outperforms conventional SIC. Further, the proposed algorithm's performance is analyzed under the practical case of imperfect CSI at the receiver node to validate the robustness.

3.1 Introduction

The fundamental idea behind NOMA is to accommodate multiple users in the same resource block by leveraging power diversity, thereby resulting in multi-user interference. SIC is the predominant algorithm for mitigating interference in NOMA. In SIC, decoding is carried out iteratively, starting with the strongest user signal and progressing to the weakest in succession. The SIC algorithm is prone to error propagation at each detection layer, stemming from inaccurate decisions made in earlier detection layers, leading to imperfect SIC decoding [58]. Consequently, imperfect SIC substantially degrades the performance of NOMA users [59]. To overcome the drawback, an MF-SIC algorithm for both the downlink and uplink NOMA system is proposed in this chapter.

Performance of the NOMA system in uplink and downlink scenario with the SIC algorithm is extensively analyzed in the literature, which mainly focuses on outage probability, sum rate, and error rate. The outage probability of the uplink NOMA system is analyzed in [60–62]. The outage probability and achievable sum-rate expression are derived in [60], considering a two-user uplink NOMA system. In [63, 64], the authors considered a downlink NOMA system with randomly deployed users, and a closed-form expression of outage probability is derived based on order statistics. In [65], the author introduces an advanced SIC technique for the NOMA system. The technique involves mapping the received signal into subgroups, enabling enhanced interference cancellation capabilities. The chapter delves into an in-depth analysis of the end-to-end outage probability. In [61], the authors considered a dynamic decoding order of SIC based on instantaneous CSI. A closed-form outage probability expression is derived considering three users' uplink NOMA system. In [62], the authors proposed an advanced SIC receiver and outage probability are investigated over the Rayleigh faded channel. The error rates of the NOMA system are analyzed in [41–46, 66–68]. In [66], the authors investigated an uplink NOMA system and analysed the system in terms of BER. In [69], the authors examine the NOMA systems, analyzing the BER performance while considering both perfect and imperfect SIC. In [70], the authors analyze the impact of co-channel interference on relay-aided NOMA networks and demonstrate that co-channel interference degrades the performance of the NOMA system. The outage probability and error rate reported in [60–62, 66, 67, 69] exhibits an error floor, diminishing the reliability of NOMA transmission. Conversely, strict conditions on the power allocation and number of users are considered in [71–74], to eliminate the error floor. In [73, 75], an uplink NOMA system is considered with a joint maximum likelihood (JML) detector. However, JML performs an exhaustive search over all the constellation points. However, as the modulation orders and the number of users increases, the number of constellation points grows exponentially, and therefore, the JML search becomes computationally impractical In [74], the noise floor in the error rate of the uplink and downlink NOMA system is eliminated by considering an adaptive decoding region, however, being limited to the quadrature phase shift key modulation scheme with three users.

Contributions

To this end, SIC forms an integral part of the detector module used in NOMA-based receiver [66, 67, 69]. In SIC, interference from the weak user is inevitable and leads to decoding errors, resulting in imperfect SIC. Thus, the significant interference in SIC detection results in an error floor [59, 69]. Constraining the number of users in a single resource block and with adequate power diversity between users are assumed to avoid the error floor [71, 74], which would defeat the main reason for introducing NOMA. Thus, a new design in the NOMA detection technique is required to achieve massive connectivity for massive IoT devices. This work introduces a novel MF-SIC algorithm for uplink NOMA detection. The receiver algorithm is based on the reliable decision of each user. Multiple neighbouring constellations (NC) points are generated at each detection layer if the constellation points are outside the reliable region. Thus, more constellation points in the decision tree are considered to mitigate the error propagation in each layer. Further, the proposed algorithm is analyzed in terms of ASER, revealing its significant outperformance compared to conventional SIC. The impact of different parameters on the user's performance is analyzed considering the proposed algorithm.

In a practical system, obtaining a perfect channel estimation at the receiver is not feasible due to inherent issues such as channel noise and imperfections in estimation algorithms. Imperfect channel estimation primarily results from factors like CEE and quantization errors. Moreover, the performance of channel estimation is influenced by the time-varying nature of the channel, the estimation technique employed, and the integration of signal detection with channel estimation. Thus, in the proposed work, simulations are performed considering the practical case of imperfect CSI to validate its robustness. Furthermore, the proposed algorithm's computational complexity (CC) is compared with that of conventional SIC. The performance-complexity trade-off and CC w.r.t different parameters of the proposed algorithm are also provided.

3.2 System Model

This section introduces the system model for the downlink and uplink NOMA system. Some notations and assumptions are presented in this section, with an introduction to SIC in the downlink and uplink NOMA system.

3.2.1 Downlink NOMA system

In the downlink NOMA system, a single-antenna BS and K-single antenna users $(UE_1, UE_2, \cdots, UE_K)$ are considered. The BS transmits the symbol intended for K-users employing superimposition coding. The superimposed signal at BS is given by

$$X = \sum_{k=1}^{K} \sqrt{a_k} x_k, \tag{3.1}$$

where a_k is the power allocation coefficient and x_k is a complex modulated symbol with unit energy for the k^{th} user respectively. Further, it is assumed that the data symbols x_k are modulated with M_k-QAM. Let vector $\mathbf{a} = [a_1, a_2, \cdots, a_K]$ where the condition on coefficients are given as $\sum_{k=1}^{K} a_k = 1$ and $a_k > 0$. The received signal at k^{th} user is given as

$$y_k = \sqrt{P} h_k X + n_k, \tag{3.2}$$

where P is total transmit power available at BS, h_k is the channel between the BS, and the k^{th} user. z_k is the AWGN at the k^{th} user. The link between BS and users experience an i.i.d Nakagami$-m$ distributed fading channel with m as the shape parameter. For reliable detection, it is assumed that the users are ordered based on the channel gain i.e. $|h_1|^2 \geq |h_2|^2 \geq \cdots \geq |h_K|^2$, the power is allocated in the opposite order of the channel gains $(a_1 < a_2 < \cdots < a_K)$ [43]. The user first nullify the effect of channel impairments from the received signal (y_k). The received signal

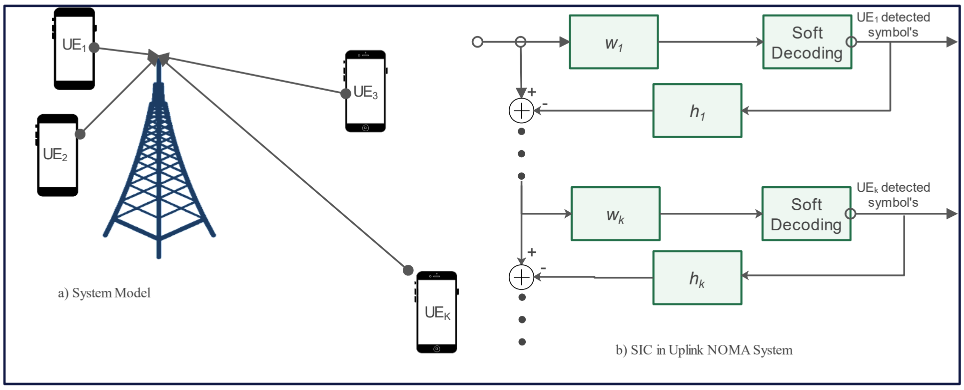

Figure 3.1: Uplink NOMA system (a) System model, (b) SIC technique.

at the k^{th} user after channel equalization is given as

$$\bar{x}_k = w_d y_k, \tag{3.3}$$

where $w_d = \frac{h_k^*}{|h_k|^2}$. In the downlink NOMA system, the SIC algorithm mitigates the multiple-user interference by exploiting the difference in the power among users. To detect the signal of the k^{th} user, the user's $U_K, \cdots, U_{k+2}, U_{k+1}$ signal needs to be detected first and cancelled from the received signal. Further, the user U_K directly detects its signal from the received signal, considering all other user signals as interference. A pseudo-code of the SIC technique is given in Algorithm 1.

Algorithm 1: Conventional SIC for downlink NOMA

Input: k, $\mathbf{a}$, y_k, h_k, K
Output: Soft output $\hat{x}_k$
$w_d = \frac{h_k^*}{|h_k|^2}$
$\bar{x}_k = w_d y_k$
for $i = K$: -1:k **do**
  $\hat{x}_i = Q(\bar{x}_k/\sqrt{a_i})$
  $\bar{x}_k = \bar{x}_k - \sqrt{a_i}\hat{x}_i$

3.2.2 Uplink NOMA system

An uplink NOMA system is considered as shown in Figure 3.1, consisting of the BS and K users $(UE_1, UE_2, \cdots, UE_K)$. The BS and users are equipped with a single antenna. At BS, the received signal is given by

$$y = \sum_{k=1}^{K} \sqrt{P_k} h_k x_k + n, \tag{3.4}$$

where h_k represents channel coefficient between the BS and the k^{th} user. The channel links are assumed to be Nakagami-m independent and identically distributed with shape parameter m_k and variance λ_k. The K users are ordered according to their channel gain [69, 76]. In the NOMA system, for reliable detection, it is assumed that users are ordered based on their average channel gain, with the first user having the highest average channel gain, the second user the second-highest average channel gain, and so on ($|h_1|^2 \geq |h_2|^2 \geq \cdots \geq |h_K|^2$). The transmitted power is P_k of the k^{th} user and x_k is the unit energy transmitted symbol of user k. x_k is taken from the signal constellation set $\mathbb{S} = \{s_1, s_2, \ldots, s_M\}$ of M-QAM, where the modulation order is given by $\mathbf{M}$, $\mathbf{M} \in \{M_1, M_2, \cdots M_K\}$ In the uplink NOMA scenario, each user transmits using their own power without the need for centralized power allocation by the base station [69, 77]. This self-management by users means that the base station does not need to schedule power allocation, as each device is responsible for its own battery and transmission power. Therefore, the power allocation issue primarily concerns downlink scenarios and is less relevant for uplink scenarios. For 4-QAM constellation, $\mathbb{S} = \{(\pm 1/\sqrt{2}, \pm 1/\sqrt{2})\}$. n is the additive white Gaussian noise assumed as complex normal with mean zero and variance σ_0^2.

- In a practical system, at the receiver, the perfect knowledge of CSI is unavailable and is estimated by the channel estimation, resulting in the CEE and deteriorating the system performance [78, 79]. Thus, according to the minimum mean square error estimation,

$$h_k = \hat{h}_k + \epsilon_k, \tag{3.5}$$

where $\hat{h}_k$ is the estimate of the k^{th} user channel and h_k is the actual channel gain of the k^{th} user. The ϵ_i is CEE, which is assumed to be complex normal with zero mean and variance σ_e^2. The estimated variance is given by $\hat{\lambda}_k = \lambda_k - \sigma_e^2$, assuming the $\hat{h}_k$ and ϵ_k are uncorrelated.

- Considering imperfect CSI due to the feedback delay, the estimation model is given as

$$h_k = \rho_i \hat{h}_k + \sqrt{1-\rho_k^2}\epsilon_k^f, \tag{3.6}$$

  where ϵ_k^f represents the estimation error and $\hat{h}_k$ is estimated CSI. ϵ_k and $\hat{h}_k$ are independent complex Gaussian random variable with zero mean and variance σ_e^2 and λ_k, respectively. $\rho_i \in (0,1)$, is the correlation coefficient between h_k and $\hat{h}_k$ and obtained using the Jakes' auto correlation model [80].

Since SIC decodes iteratively, $K-1$ iterations are required to detect all the K-users symbols as given in Algorithm 2. The SIC reduces the interference by cancelling out an undesired signal to yield reliably detected symbols. In SIC, to detect the k^{th} users' signal, the BS detects and cancels out the signal of users $UE_1, UE_2, \cdots, UE_{k-1}$. At the receiver, the received signal is processed as follows

$$\bar{x}_k = w_k y, \tag{3.7}$$

where $w_k = \frac{h_k^*}{|h_k|^2}$ is the channel inverse of the k^{th} user. The channel inverse of K users is given by vector $\mathbf{w} = \frac{\mathbf{h}^*}{|\mathbf{h}|^2}$, where $\mathbf{h}^*$ denotes the conjugate of $\mathbf{h}$, $|\mathbf{h}|$ is modulus of $\mathbf{h}$ and vector $\mathbf{h} = [h_1, h_2, \cdots, h_K]$ represents of K users channel. The soft decision $\bar{x}_k$ maps to the nearest constellation point and is expressed as

$$\mathrm{Q}(\bar{x}_k) = \arg\min_{j\in\mathbb{S}} |\bar{x}_k - s_j|^2. \tag{3.8}$$

Algorithm 2: Conventional SIC for uplink NOMA

Input: y, $\mathbf{h}$, K
Output: Soft output $\hat{x}$
$\mathbf{w} = \frac{\mathbf{h}^*}{|\mathbf{h}|^2}$
for $i = 1{:}1{:}K$ **do**
  $\bar{x}_i = w_i y$
  $\hat{x}_i = \mathrm{Q}(\bar{x}_i)$
  $y = y - h_i \hat{x}_i$

3.3 MF-SIC Algorithum

3.3.1 Uplink NOMA system

This section illustrates the proposed MF-SIC algorithm for the uplink NOMA system. The MF-SIC algorithm block diagram is shown in Figure 3.2. Since the conventional SIC suffers from multi-user interference, it results in degrading the NOMA users' performance [69]. An MF-SIC algorithm is proposed, where the optimal constellation point is selected from the multiple points available in the feedback. The pseudo-code of MF-SIC for the uplink NOMA system is presented in Algorithm 3. The MF-SIC algorithm is based on reliable detection at each detection layer. The reliability of the detected symbol is determined based on the shadow area constraint. The shadow area is the reliable region defined around the constellation point from the set $\mathbb{S}$. The shadow area is the sphere around the given constellation point based on the predefined radius $\mathbf{d_{th}}$, $\mathbf{d_{th}} \in \{d_{th-1}, d_{th-2}, \cdots, d_{th-K}\}$, d_{th-1} denoting the predefined radius for the first user, d_{th-2} for the second user, and so forth. The radius $\mathbf{d_{th}}$ reduces the CC of the algorithm by avoiding the processing of reliable detection.

The reliability of the soft output is checked based on the Euclidean distance d given as

$$d = |\bar{x}_k - \mathrm{Q}(\bar{x}_k)| \tag{3.9}$$

If the $d < d_{th-k}$, i.e. the $\bar{x}_k$ is in the reliable region, where $\mathrm{Q}(\bar{x}_k)$ is considered to be the reliable output of the k^{th} user. The symbol detection is done similarly to SIC. Thus, the MF-SIC algorithm follows the same approach as SIC if the condition $d < d_{th}$ is satisfied for all the users. The shadow region diagram for the two-user NOMA system is illustrated in Figure 3.3. Figure 3.3 (a) represents the constellation point of UE_1 in the presence of interference and the shadow area with radius d_{th-1}. The points which are outside the shadow region, i.e. the circle with radius d_{th-1}, will be considered unreliable points, and the MF-SIC algorithm will be applied to obtain the optimum point of UE_1. Further, the Figure 3.3 (b) represents the constellation point of UE_2 after SIC. The shadow area is represented for the UE_2 with radius d_{th-2}.

If the $d \geq d_{th-k}$, the $\bar{x}_k$ is considered to be in the unreliable region. The user's symbol will be decoded based on the MF-SIC algorithm. In MF-SIC, multiple NCs are used to find the optimal detected symbol. The NC are selected from the constellation set $\mathbb{S}$. Let $\mathbb{L} \in \{z_1, z_2, \cdots, z_S\}$ be the set of NC points selected based on the minimum distance between $\mathrm{Q}(\bar{x}_k)$, and the constellation points from the set $\mathbb{S}$.

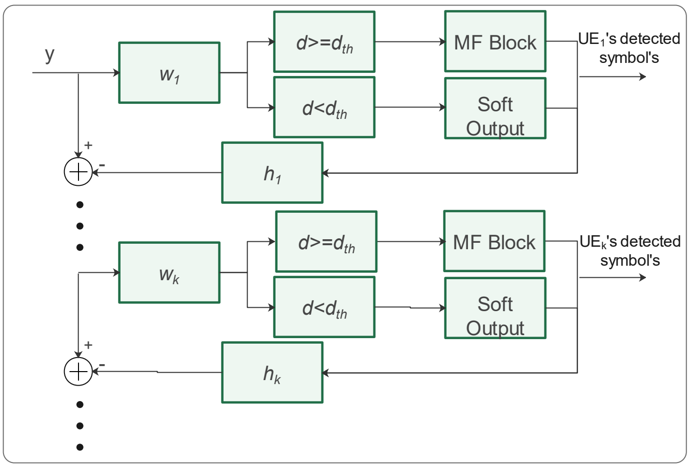

Figure 3.2: Multiple feedback SIC algorithm for the uplink NOMA system.

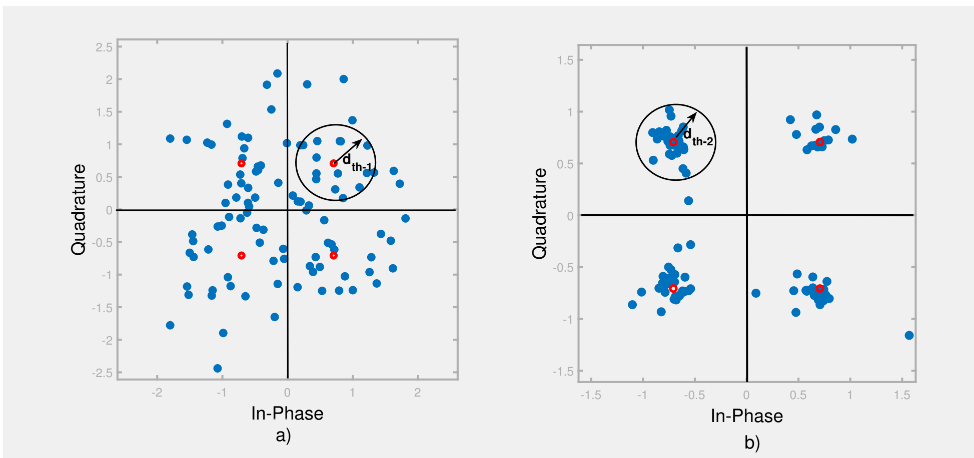

Figure 3.3: Shadow regions representation of two-user NOMA system.

When $d \geq d_{th}$, the routine MFloop as shown in Algorithm 4 is called. In the MFloop function, $\mathbb{L}$ is initialized with the NC point of $\bar{x}_k$. Such that the point z_1 is the nearest constellation point to $\mathrm{Q}(\bar{x})$, z_2 is the second nearest point to $\mathrm{Q}(\bar{x})$, and so on. The $\hat{x}_k^j$ is initialized with the optimal candidate constellation point z_j. Considering $\hat{x}_i^j$ as one of the optimal feedback constellation points selected from $\mathbb{L}$ for the k^{th} user, then the solution vector $\hat{x}^j$ is obtained using SIC algorithm to compute the symbols of subsequent users. The function MFloop recursively checks reliability conditions in all the subsequent layers to obtain the optimal constellation point. The remaining user signals, i.e. $k+1, k+2, \cdots, K$ users, are performed by symbol cancellation and checking the unreliability condition at each layer. Let $\mathbf{S}$ denotes the total NC points generated such that $\mathbf{S} \in \{S_1, S_2, \cdots, S_K\}$. Thus, a total set of S_k different solution $(\hat{\mathbf{x}}^1, \hat{\mathbf{x}}^2, \ldots, \hat{\mathbf{x}}^S)$ is obtained for the k^{th} user. The indexed value of the optimum solution is selected from the number of NC points generated, which minimizes the function below

$$\hat{j} = \arg \min_{j \in 1,2,\cdots,S} |y - \mathbf{h}\hat{\mathbf{x}}^j|^2, \tag{3.10}$$

Thus, the optimum detected symbol of the k^{th} user is given as

$$\hat{x}_k = \hat{x}_k^j \tag{3.11}$$

In the MF-SIC algorithm, the recursive checking of reliability conditions reduces the error propagation compared to the conventional SIC. However, recursive computation increases the CC. Hence, the MF-SIC algorithm is bounded by the NC points ($\mathbf{S}$), the reliability condition ($\mathbf{d_{th}}$) and the recursions allowed ($\mathbf{L}$). The value $\mathbf{L}$ defines the number of MFloop recursions in each user detection. For the value of $L_k = 1$, the NC points are generated in the first layer of the MF-SIC algorithm of the K^{th} users, and the detection of further layers is performed equivalent to a SIC technique. Thus, the choice of $\mathbf{d_{th}}$, $\mathbf{S}$ and $\mathbf{L}$ depends on the target error rate and tolerable CC. Further, the multiple iterations of each $\mathbf{S}$ neighbouring element can be performed in $\mathbf{S}$ parallel streams, thus increasing the overall algorithm speed.

3.3.2 Downlink NOMA system

This subsection presents the proposed MF-SIC technique for the downlink NOMA system. In the downlink NOMA system, symbols of the user U_k are detected after detecting and subtracting the subsequent users (U_{k+1} to U_K) symbols. Thus, the decoding order in the downlink NOMA system is in reverse order as that of the uplink NOMA system. With the increase in the number of users, the interference at users to detect its symbol increases, resulting in unreliable detection of symbols.

Algorithm 3: Proposed MF-SIC for uplink NOMA

```
Input: y, d_th, M, h, K, S, L
Output: Soft output x̂
Y = y
w = h* / |h|^2
for i = 1:1:K do
    x̄_i = w_i Y
    d = |x̄_i − Q(x̄_i)|
    if d ≥ d_th(i) then
        [x̂_i] = MFloop(x̄_i, y, Y, h, w, d_th, i, K, S L)
    else
        x̂_i = Q(x̄_i)
    Y = Y − h_i x̂_i
```

Algorithm 4: MFloop routine

```
function [x̂_i] = MFloop(x̄_i, y, Y, h, w, d_th, i, K, S, L)
𝕃 = [z_1, z_2, ··· , z_S]
for j=1:1:S(i) do
    x̂_i^j = z_j neighborhood set of x̄_i
    Y = Y − h x̂_i^j
    for l=i+1:1:K do
        x̄_l^j = w_l Y
        if l ≤ L(l) then
            d = |x̄_l^j − Q(x̄_l^j)|
            if d ≥ d_th(l) then
                [x̂_l^j] = MFloop(x̄_l^j, y, Y, h, w, d_th, l, K, S, L)
            else
                x̂_l^j = Q(x̄_l^j)
        else
            x̂_l^j = Q(x̄_l^j)
        Y = Y − h_l x̂_l^j
ĵ = arg min_{j∈1,2,··· ,S} |y − h x̂^j|^2
return x̂_i = x̂_i^ĵ
```

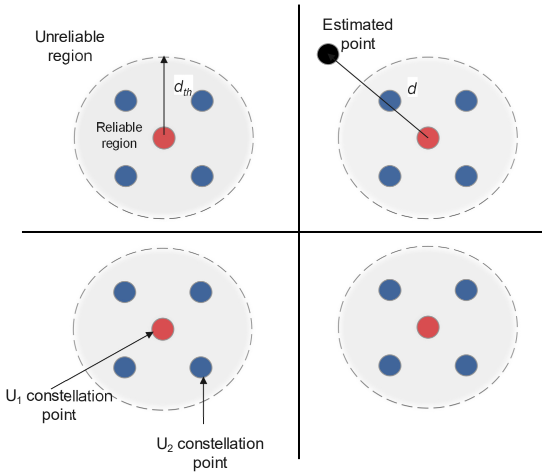

Figure 3.4: Reliable region for two users NOMA system with $M_1 = M_2 = 4$ constellation point in MF-SIC.

Hence, unreliable detection leads to error propagation in the subsequent layer of SIC detection. Thus, a low-complexity MF-SIC algorithm is proposed for the downlink NOMA system to achieve massive connectivity with reliable symbol detection. The pseudo-code of the proposed algorithm for downlink NOMA is given in Algorithm 5. Detection of symbol using the proposed algorithm for the k^{th} NOMA user is illustrated in this section. In the proposed algorithm, the multiple neighbouring constellation points are used in the decision feedback loop to find the optimal constellation point. The MF-SIC is based on the reliability of the constellation point. At the i^{th} loop the reliability condition is defined as

$$D = |\bar{x}_k - Q(\bar{x}_k/\sqrt{a_i})| \tag{3.12}$$

where $\bar{x}_k = w_d y_k$, if the D is less than the predefined threshold d_{th}, the detection is reliable detection and the soft output of the received signal is obtained as conventional SIC. However, if $D \geq d_{th}$, the detection is considered unreliable and multiple neighbouring constellation points are used to obtain the optimal detection. The neighbouring constellation points are obtained following the same procedure as the uplink NOMA system. Whereas, in the downlink NOMA system, the neighbouring constellations are not generated recursively in the i^{th} layer of detection. Unlink uplink NOMA where neighbouring constellations are generated recursively in each detection layer. The detection of subsequent users $i-1$ to 1 is performed in a similar way as that in a conventional SIC.

Algorithm 5: Proposed MF-SIC for downlink NOMA

Input: k, $\mathbf{a}$, y_k, d_{th}, h_k, K, S
Output: Soft output $\hat{x}_k$
$w_d = \frac{h_k^*}{|h_k|^2}$
$\bar{x}_k = w_d y_k$
$\bar{x} = w_d y_k$
for $i = K$:-1:k **do**
    $D = |\bar{x}_k - Q(\bar{x}_k/\sqrt{a_i})|$
    if $D \geq d_{th}$ **then**
        $\mathbb{L} = \{z_1, z_2, \cdots, z_S\}$
        for j=1:1:S **do**
            $\hat{x}_i^j = z_j$ neighborhood set of $\bar{x}_k$
            $\bar{x}_k = \bar{x}_k - \sqrt{a_i}\hat{x}_i^j$
            for l=i-1:-1:1 **do**
                $\hat{x}_l^j = Q(\bar{x}_i/\sqrt{a_i})$
                $\bar{x}_k = \bar{x}_k - a_l\hat{x}_l^j$
        $\hat{j} = \arg\min_{j\in 1,2,\cdots,S} |\bar{x} - \sqrt{\mathbf{a}}\hat{\mathbf{x}}^j|^2$
        return $\hat{x}_i = \hat{x}_i^{\hat{j}}$
    else
        $\hat{x}_i = Q(\bar{x}_k/\sqrt{a_i})$
    $\bar{x}_k = \bar{x} - \sqrt{a_i}\hat{x}_i$

3.4 Simulation Results and Discussion

In this section, simulation results are presented to assess the NOMA system performance, focusing on ASER. The ASER performance of MF-SIC is compared with that of conventional SIC across different numbers of users. The results are obtained through Matlab simulations with 10^4 Monte-Carlo iterations. The simulation is performed for different numbers of users $K = 2$ and 3. The modulation order of users $M_1 = M_2 = M_3 = 4$. The Nakagami parameters are considered as $m_1 = 3$, $m_2 = 2$, and $m_3 = 1$, with channel gains between the BS and users given by $\lambda_1 = \lambda_2 = 1$ and $\lambda_3 = 0.5$. In this setup, UE_1 is assigned the strongest channel, while the K^{th} user has the weakest channel such that the UE_1 is assigned the strongest and the K^{th} user with the weakest channel. The users' transmit powers are uniformly set to $P_1 = P_2 = P_3 = 1$. Unless otherwise specified, the algorithm parameters are assumed to be $d_{th} = d_{th-1} = d_{th-2} = d_{th-3}$, $L = L_1 = L_2 = L_3$ and $S = S_1 = S_2 = S_3$.

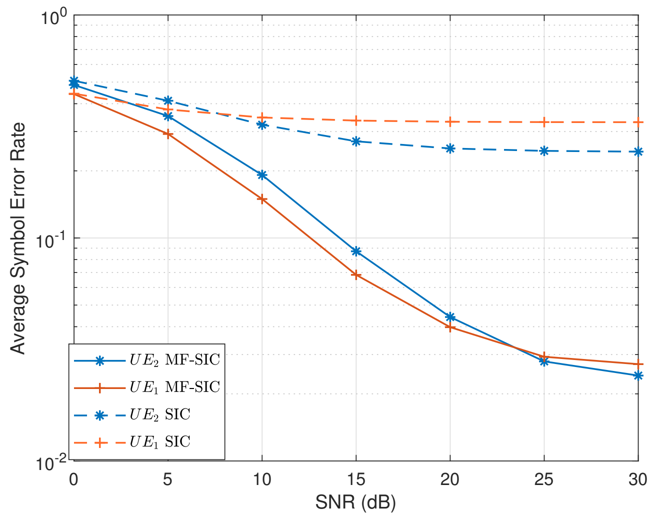

Figure 3.5: ASER w.r.t. the transmit SNR for a two-user uplink NOMA system.

Comparison of MF-SIC and SIC

In Figure 3.5, the ASER of the two-user uplink NOMA system is presented w.r.t. SNR. The MF-SIC algorithm parameters are set as $d_{th-1} = d_{th-2} = 0.2$, $S_1 = S_2 = 4$ and $L_1 = L_2 = 3$. The figure demonstrates the superiority of the proposed algorithm over the conventional SIC. It is observed from the figure that the proposed algorithm achieves a lower ASER than the conventional SIC, particularly at high SNRs. It is observed that the error floor at high SNR achieved in conventional SIC is eliminated by employing the MF-SIC algorithm. The proposed MF-SIC algorithm considers a neighbouring constellation concept, which effectively mitigates the interference caused by other users. In conventional SIC, as the SNR increases, the interference from other users also increases, leading to an ASER floor with an increase in SNR. However, in the proposed MF-SIC, the generation of neighbouring constellations while decoding at the BS effectively reduces the interference from other users, resulting in a decrease in the ASER as the SNR increases. Further, in the low and mid-range of SNR, it is observed that UE_1 shows better performance than UE_2, whereas, in the high SNR region, UE_2's performance is superior to UE_1. In UE_1, at high SNR, the interference from UE_2 dominates. Thus, the performance of UE_1 is limited because of interference, where the UE_2 symbols are detected after cancelling the interference from UE_1 symbols; thus, UE_2 shows lower ASER at high SNR.

In Figure 3.6, the ASER of the three user's uplink NOMA system are presented w.r.t. SNR. The MF-SIC parameters are set as $d_{th-1} = d_{th-2} = d_{th-3} = 0.2$, $S_1 = S_2 = S_3 = 4$ and $L_1 = L_2 = L_3 = 3$. The figure shows that when the conventional SIC is utilized to detect users' symbols, the ASER of all users shows a constant error floor with the increase in the SNR. However, the error floor is eliminated when the MF-SIC algorithm is utilized to detect symbols. It is observed that the ASER of users shows a linear decrease with the increase in the SNR.

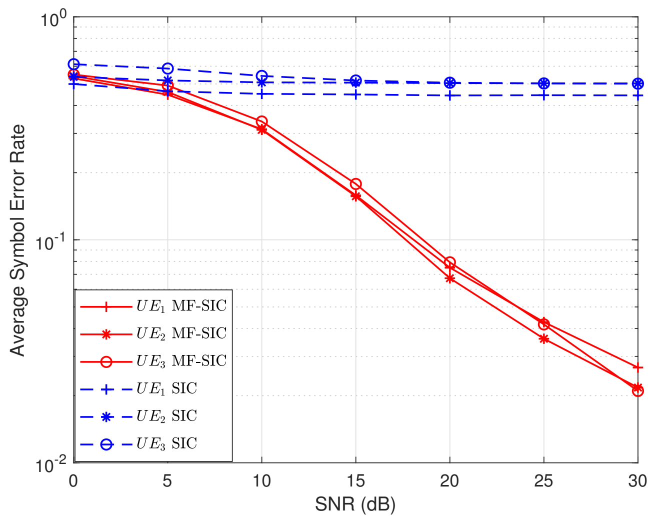

Figure 3.6: ASER w.r.t. the transmit SNR for a three-user uplink NOMA system.

In Figure 3.7, the ASER of the downlink NOMA system is presented considering three users with respect to SNR for different NOMA power allocation coefficients. Two different case of power allocation coefficients are considered for analysis given as $a_1 = 0.1$, $a_2 = 0.2$, $a_3 = 0.6$ and $a_1 = 0.05$, $a_2 = 0.15$, $a_3 = 0.7$. It is observed that the proposed algorithm does not show any performance improvement over the conventional SIC considering $a_3 = 0.7$, whereas with $a_3 = 0.6$, the ASER performance with the MF-SIC algorithm shows significant performance improvement compared to the SIC algorithm. The ASER of users using the SIC algorithm reaches a constant error floor with the increase in the SNR, whereas with the MF-SIC algorithm, a decrease in the ASER with an increase in the SNR is observed. Thus, utilizing the proposed algorithm, the desirable performance of users is achieved without any constraint on the power allocation of the NOMA users. The UE_3 can detect its signal directly without employing SIC. Hence, UE_3 performance analysis is not considered.

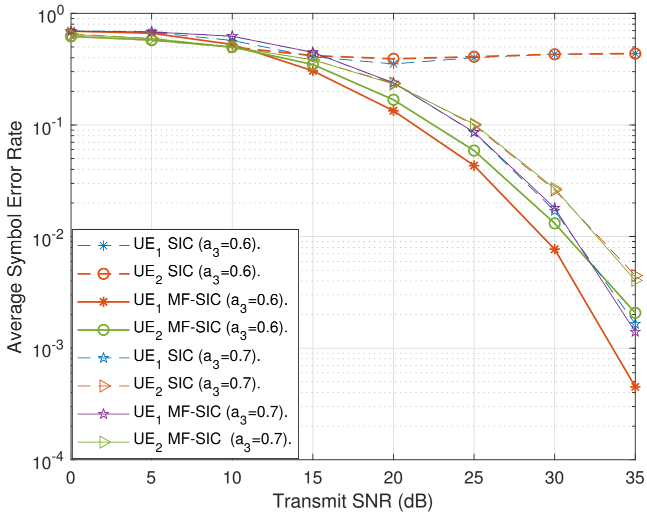

Figure 3.7: ASER w.r.t. transmit SNR for three user downlink NOMA system.

In Figure 3.8, ASER of four user downlink NOMA system is performed with respect to SNR. The power allocation coefficients are chosen as $a_1 = 0.08$, $a_2 = 0.12$, $a_3 = 0.2$ and $a_4 = 0.6$. It is observed that there is an improvement in the performance of all users with MF-SIC over the conventional SIC. At ASER of 5×10^{-3}, UE_1 with MF-SIC shows SNR gain of 3 dB over SIC. It is observed that the ASER performance of UE_2 and UE_3 with SIC shows a constant error floor with varying SNR, whereas with MF-SIC, the ASER of UE_2 and UE_3 decrease with the SNR increase. In MF-SIC, the optimal constellation point is selected from multiple constellation generations in the feedback loop, resulting in a decrease in the error propagation in each layer. Thus, the ASER of UE_2 and UE_3 show a significant improvement with the increase in SNR. Further, it is observed that at ASER of 6×10^{-2}, UE_1 has an SNR gain of 6 dB and 7dB over UE_2 and UE_3, respectively. Since users are ordered based on the channel gain such that UE_1 has a strong channel condition, resulting in reliable detection at the user UE_1 compared to UE_2 and UE_3. Thus, UE_1 shows better ASER performance than UE_2 and UE_3.

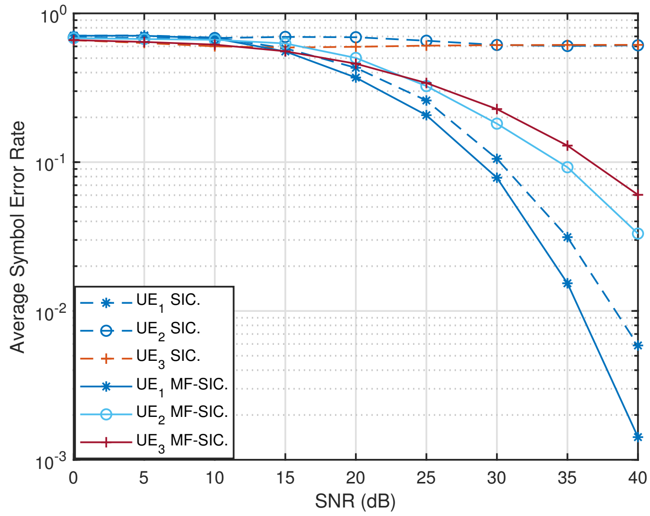

Figure 3.8: ASER w.r.t. transmit SNR for four user downlink NOMA system.

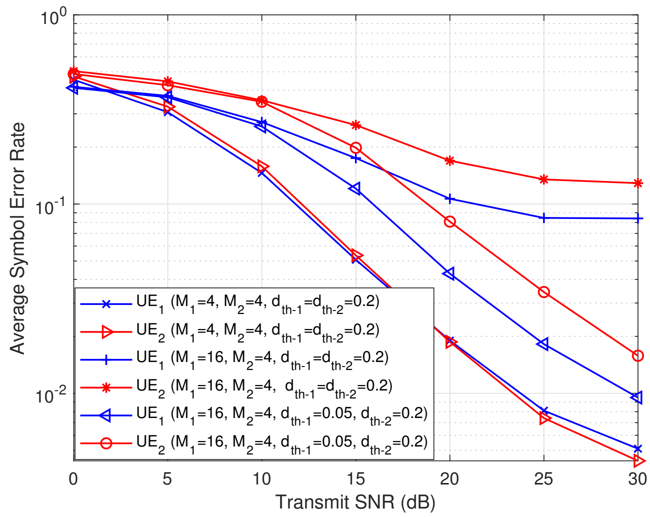

Figure 3.9: ASER w.r.t the transmit SNR for a two-user uplink NOMA system.

Impact of different modulation order (M)

In Figure 3.9, the ASER is plotted against the SNR for different modulation orders. It is assumed that the near user has $M_1 = 16$ and the far user has $M_2 = 4$. The modulation order is chosen based on the CSI estimated by the BS. UE_1, with good channel conditions, increases data rates by using a higher modulation order, while UE_2, with poorer channel conditions, uses a lower modulation order. It is observed that as the modulation order increases, the performance of the users degrades due to increased interference from the higher constellation order. Further, the results considering different d_{th} values for different users is also included. UE_1 with a higher modulation order is considered with $d_{th-1} = 0.05$, while UE_2 with a lower modulation order is considered with $d_{th-2} = 0.2$. Since the Euclidean distance between points decreases with higher modulation orders, thus for UE_1 with higher modulation order, a lower d_{th-1} value is chosen. It is observed from the figure that as d_{th-1} is reduced from 0.2 to 0.05, the performance of the user improves significantly. At an ASER of 10^{-1}, UE_1 with $d_{th-1} = 0.05$ shows an SNR gain of 5dB over $d_{th-1} = 0.2$ due to the smaller Euclidean distance for 16-QAM compared to 4-QAM.

Impact with respect to received SNR

In Figure 3.10, the ASER is plotted with respect to the received SNR for a three-user uplink NOMA system. The received SNR of the k^{th} user to the BS is given as [73], $\rho_{B,k} = \frac{P_k \mathbb{E}[|h_k|^2]}{N_0}$, where $\mathbb{E}$ is the expectation operator. It is observed from the figure that as the SNR increases, the ASER decreases for all three users.

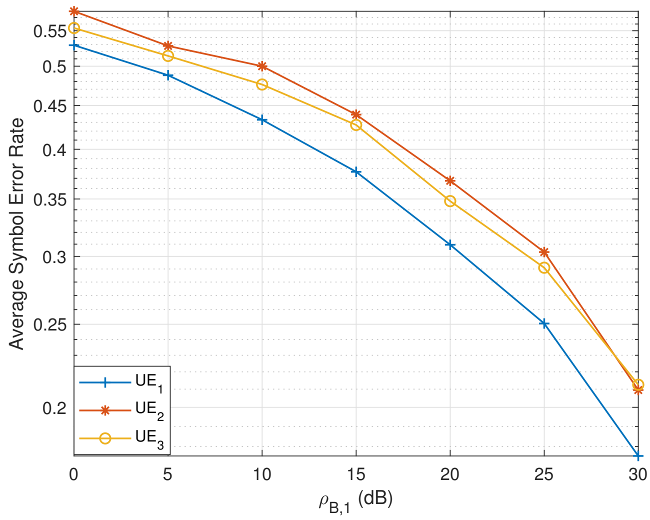

Figure 3.10: ASER w.r.t. the received SNR for a three-user uplink NOMA system.

Impact of number NC (S)

Figure 3.11 shows the ASER plotted against the SNR for different values of **S**, where **S** represents the number of neighbouring constellation points generated. It is observed that as S increases, the performance of the proposed algorithm improves significantly. Specifically, higher values of S correspond to a larger pool of neighbouring constellation points, which enhances the proposed algorithm's ability to decode the received symbols accurately. This leads to a reduction in ASER, demonstrating that the proposed algorithm's performance becomes more robust with an increase in S. The figure clearly illustrates that at any given SNR, increasing S results in a lower ASER, highlighting the trade-off between computational complexity and error performance.

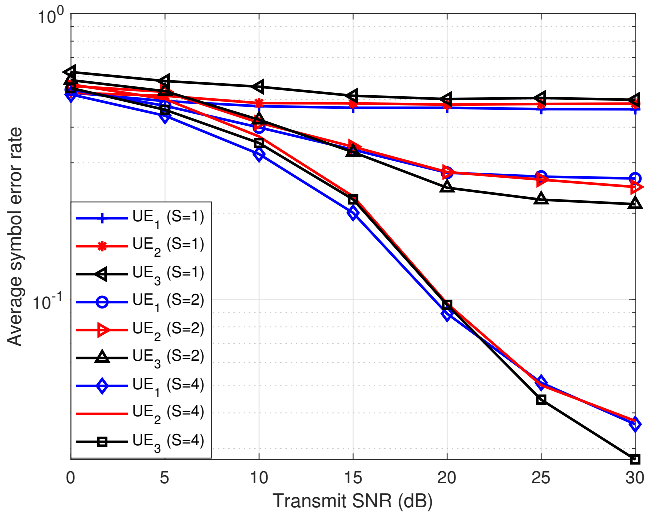

Figure 3.11: ASER w.r.t. the transmit SNR for a three-user uplink NOMA system with different $\mathbb{S}$.

Impact of number of recursions (L)

In Figure 3.12 and Figure 3.13, ASER of the two and three user's uplink NOMA system, respectively, are presented w.r.t SNR for different values of $\mathbf{L}$. It is observed from the figures that the performance of users increases with the increase in L value. In Figure 3.12, it is observed that at ASER of 2.4×10^{-3} of UE_1, MF-SIC with $L = 3$ provides an SNR gain of 1.5 dB over $L = 1$. For the same ASER of UE_2, the MF-SIC with $L = 3$ provides an SNR gain of 1.5 dB over $L = 1$. The L limits the number or recursion in each detection layer. Thus, with the increase in L, multiple constellation points are generated in each layer of MF-SIC detection to find the optimal constellation point. In Figure 3.13, it is observed that the ASER of users decreases significantly with an increase in L from 1 to 3. At ASER of 2.5×10^{-1}, UE_1 with $L = 3$ shows an SNR gain of 8 dB over $L = 1$. At high SNR, the ASER performance with $L = 1$ suffers from the error floor and reaches a constant value of 0.24, 0.19 and 0.15 for UE_1, UE_2 and UE_3, respectively. With increased SNR, each layer's multi-user interference and error propagation limit the user's performance. Meanwhile, with $L = 3$, multiple constellation points in each layer lead to a decrease in the user's ASER.

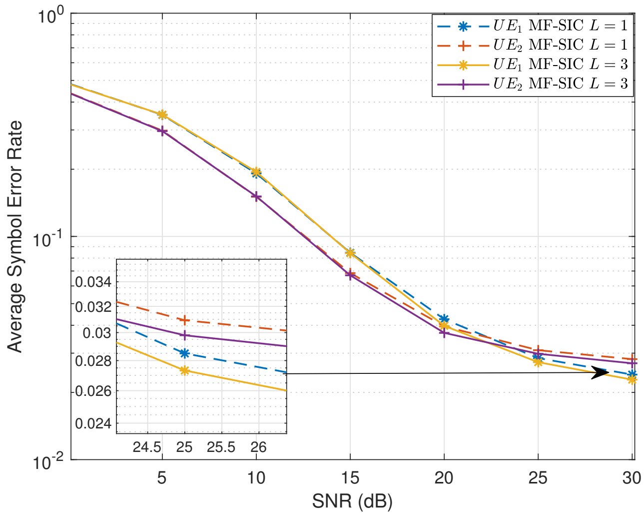

Figure 3.12: ASER w.r.t. the transmit SNR for a two-user uplink NOMA system.

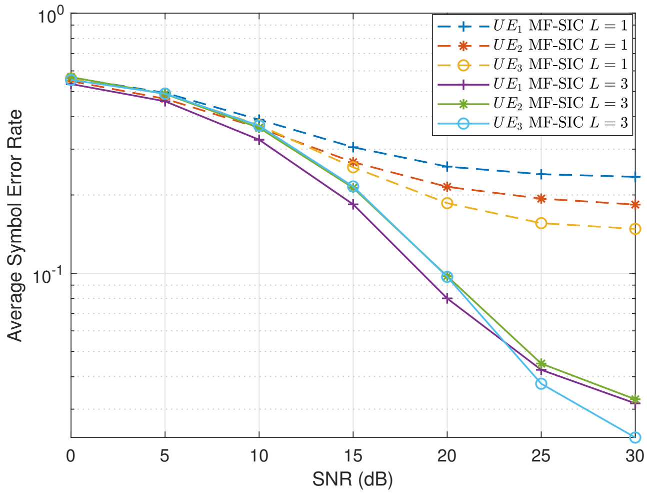

Figure 3.13: ASER w.r.t. the transmit SNR for a three-user uplink NOMA system.

Impact of reliable region ($\mathbf{d_{th}}$)

In Figure 3.14, ASER of the uplink NOMA system with three users is presented with different values of $\mathbf{d_{th}}$. The figure illustrates that users exhibit similar perfor-

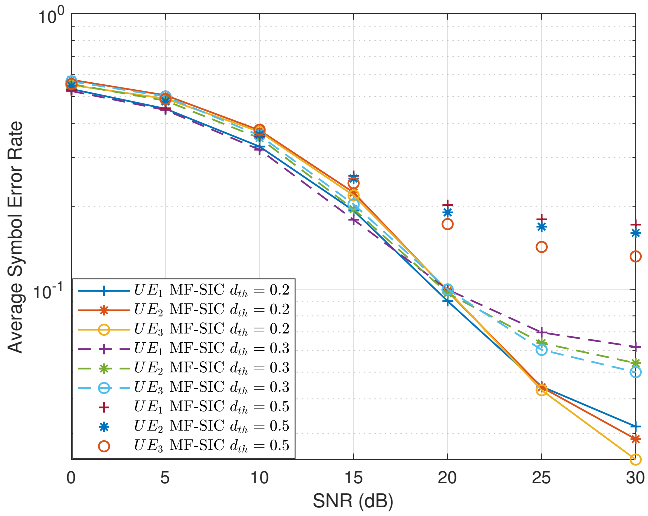

Figure 3.14: ASER w.r.t the transmit SNR for a three-user uplink NOMA system.

mance across various $\mathbf{d_{th}}$ values in the low SNR region. In contrast, a significant improvement in the ASER is observed in the high SNR region with a decrease in the d_{th}. At ASER of 1.4×10^{-1} with $d_{th} = 0.2$, UE_3 has an SNR gain of 7 dB over $d_{th} = 0.5$. And at ASER of 5×10^{-2} with $d_{th} = 0.3$, UE_3 has an SNR gain of 6 dB over $d_{th} = 0.5$. For a high value of d_{th} (0.5), the reliability region of the constellation point increases. Thus, the detected symbol is obtained the same way as it is performed in SIC, decreasing users' performance.

Comparison of MF-SIC with JML

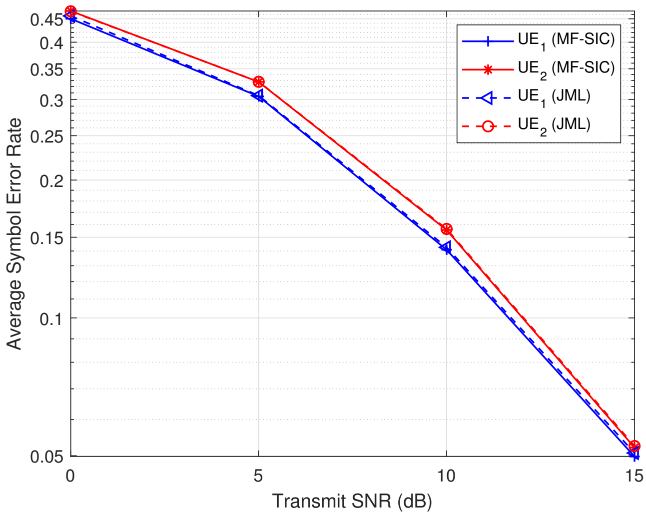

Figure 3.15: ASER w.r.t. the transmit SNR for a two-user uplink NOMA system.

Figure 3.15 illustrates the ASER of a two-user uplink NOMA system with the JML [73] and MF-SIC algorithms. It is observed from the figure that both algorithms provide similar ASER performance for NOMA detection. The JML performs an exhaustive search over all constellation points. However, as the modulation orders and the number of users increases, the number of constellation points grows exponentially, and therefore, the JML search becomes computationally impractical. The MF-SIC algorithm, on the other hand, considers only neighbouring constellation points and leaves the others. Further, the JML algorithm has a fixed computational complexity, whereas the proposed MF-SIC algorithm has a computational complexity that depends on the algorithm parameters $\mathbf{S}$, $\mathbf{L}$, and $\mathbf{d}_{\text{th}}$, as depicted in Table 3.1.

Impact of imperfect CSI

In Figure 3.16, ASER of the uplink NOMA system with three users is presented considering imperfect CSI at the receiver node with CEE. The ASER for users employing MF-SIC is compared under imperfect and perfect CSI conditions, highlighting a notable impact on user performance under imperfect CSI. At ASER of 2.6×10^{-1} with MF-SIC, UE_1 with perfect CSI provides a significant SNR gain of 4 dB over imperfect CSI. Further, the ASER of the MF-SIC is compared with conventional SIC. It is observed from the figure that the performance of the proposed algorithm with imperfect CSI is superior to that of the conventional SIC under perfect CSI. The results, plotted in Figure 3.16, demonstrate that the proposed algorithm consistently outperforms the SIC technique. Even as the channel estimation error increases, the proposed algorithm maintains a lower ASER compared to SIC. This improvement is due to the enhanced detection capability of the proposed algorithm, which effectively mitigates the impact of estimation errors. These findings confirm the robustness and reliability of our algorithm in practical wireless communication scenarios.

In Figure 3.17, the ASER experienced by downlink NOMA users with MF-SIC under imperfect CSI is compared with the perfect CSI condition. It is observed that the ASER performance of users degraded under the assumption of imperfect CSI compared to perfect CSI case. At ASER of 2.1×10^{-1} with MF-SIC, UE_1 with

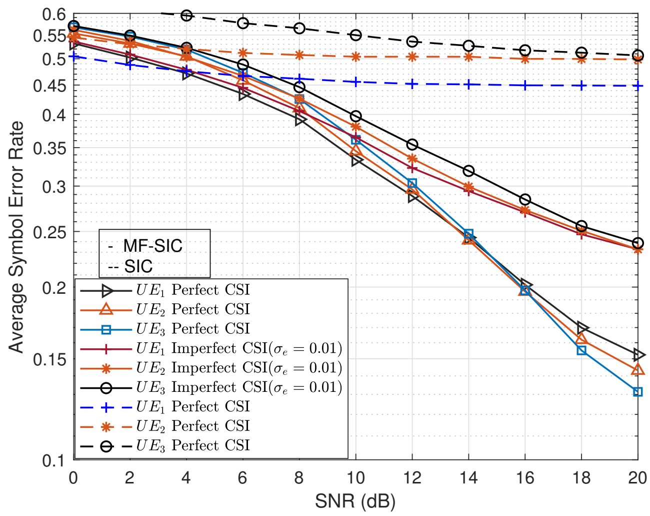

Figure 3.16: ASER w.r.t. the transmit SNR for a three-user uplink NOMA system with CEE.

perfect CSI provides an SNR gain of 4 dB over imperfect CSI. Further, at ASER of 5×10^{-1}, UE_1 with MF-SIC under imperfect CSI provides SNR gain of 3 dB over conventional SIC under perfect CSI. Thus, the performance of the proposed algorithm, even with imperfect CSI, is superior to that of the conventional SIC.

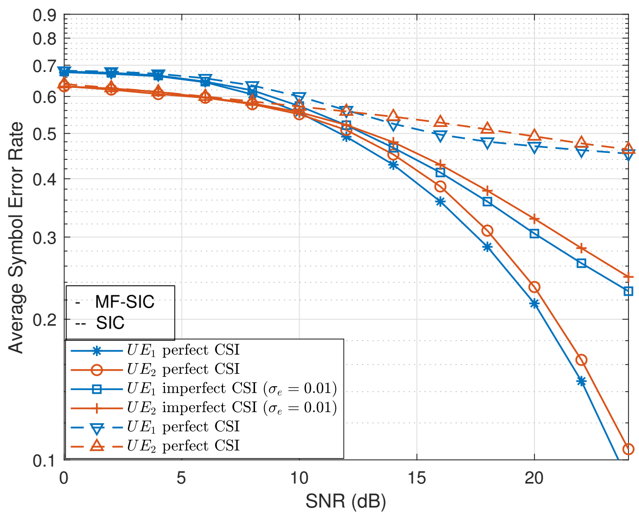

Figure 3.17: ASER w.r.t. transmit SNR for three user downlink NOMA system.

In Figure 3.18, the ASER is plotted against the SNR to compare the performance of MF-SIC with perfect CSI ($\rho = 1$) and MF-SIC with imperfect CSI ($\rho = 0.99$) due to feedback delay. The figure shows that as the SNR increases, MF-SIC with perfect CSI outperforms both the conventional SIC and MF-SIC with feedback delay. At

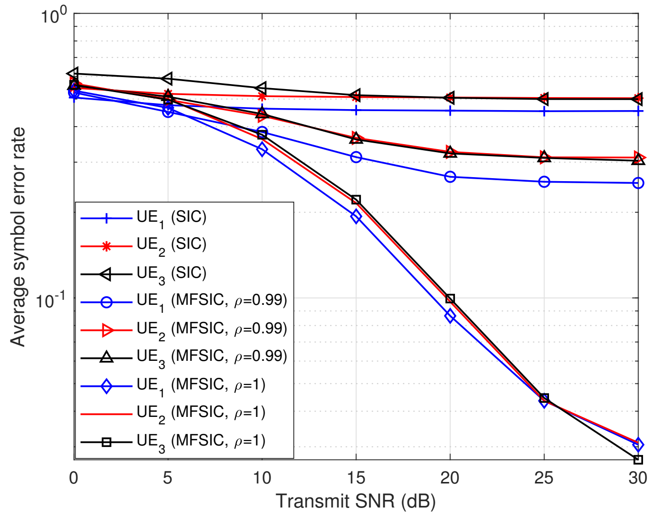

Figure 3.18: ASER w.r.t. the transmit SNR for a three-user uplink NOMA system with feedback delay.

an ASER of 0.3, it is observed that UE_1 with $\rho = 1$ shows an SNR gain of 5 dB over UE_1 with $\rho = 0.99$.

CC of MF-SIC Algorithm

The CC of the proposed algorithm is evaluated by taking the number of real-time floating point operations (FLOPS) as the standard of CC [81]. Table 3.1 illustrates the comparison of error rate (ASER) and average number of FLOPS between the proposed algorithm and the conventional SIC with N=10^5 at SNR of 25 dB. The CC is compared with the conventional SIC, revealing that the proposed algorithm exhibits higher complexity. However, this increased complexity is accompanied by an improved error rate. Further, the performance-complexity trade-off is presented in Table 3.1. Based on the target ASER, the parameters L, S, and d_{th} control the complexity of the proposed algorithm.

In Table 3.2, the complexity of the proposed algorithm is shown for different values of S, with all other parameters remaining constant. It is observed from the table that as the number of neighbouring constellation points increases, the performance of the users improves with the increase in complexity. This is due to the larger pool of constellation points in each layer of the decoding process.

Algorithm	ASER			FLOPS (10^5)
	U_1	U_2	U_3	
SIC	0.4537	0.4915	0.5033	0.1
MF-SIC ($L = 1, d_{th} = 0.2, S = 4$)	0.25	0.19	0.16	1.75272
MF-SIC ($L = 3, d_{th} = 0.2, S = 4$)	0.0450	0.0442	0.040	10.03928
MF-SIC ($L = 3, d_{th} = 0.3, S = 4$)	0.07	0.068	0.069	9.00604
MF-SIC ($L = 3, d_{th} = 0.5, S = 4$)	0.17	0.15	0.13	6.31976
MF-SIC ($L = 3, d_{th} = 0.2, S = 3$)	0.127	0.125	0.10	5.68647
MF-SIC ($L = 3, d_{th} = 0.2, S = 2$)	0.24	0.24	0.219	2.82918

Table 3.1: Comparison of complexity-performance of uplink NOMA system. (SNR = 25 dB, N=10^4)

Algorithm	ASER			FLOPS (10^5)
	U_1	U_2	U_3	
SIC	0.4537	0.4915	0.5033	0.10007
MF-SIC ($L = 4, d_{th} = 0.2, S = 4$)	0.04350	0.047	0.0.046	10.03928
MF-SIC ($L = 4, d_{th} = 0.2, S = 3$)	0.106	0.10800	0.0917	5.68647
MF-SIC ($L = 4, d_{th} = 0.2, S = 2$)	0.220	0.23	0.190	2.82918

Table 3.2: Comparison of complexity-performance of uplink NOMA system. (SNR = 25 dB, N=10^4)

3.5 Summary

The chapter analyzes the uplink and downlink NOMA system with multiple users. A multiple feedback-based SIC algorithm is proposed to mitigate the multi-user interference and error propagation in each layer of SIC. The interference suppression algorithm is developed by introducing multiple constellation points as an optimal constellation. The results show the superiority of the proposed algorithm over the conventional SIC. The proposed algorithm can avoid the error floor of the NOMA system at high SNR. The impact of different parameters on users' performance is also analyzed. Additionally, the CC of the proposed algorithm is compared with that of the conventional SIC. The impact of different parameters on the CC is also analyzed, and inferences are drawn. Further, to enhance the coverage, diversity, spectral efficiency, energy efficiency and reliability of wireless communication systems, cooperative relaying with an EH relay node is a key technology. The next chapter explores a NOMA network utilizing a cooperative EH relay node.

Chapter 4

Performance Analysis of Energy Harvested Cooperative NOMA System

In the previous two chapters, the NOMA system's error performance was analyzed with a focus on different modulation schemes. The work concentrated on enhancing error performance through optimized power constraints and algorithmic improvements. To further extend the coverage area of NOMA systems, it is essential to analyze cooperative relaying within the NOMA framework, exploring how it can enhance the reliability and performance of the system.

This chapter considers a multi-relay downlink cooperative NOMA system under practical constraints. To ensure the relay node remains efficient and sustainable, an EH-based relay is integrated into the analysis. The closed-form expression of outage probability and ergodic rate are derived for users under the assumption of imperfect CSI and imperfect SIC at the receiver node. Further, the asymptotic expression for the outage probability is also shown.

4.1 Introduction

Cooperative relaying and NOMA systems have garnered research attention due to their significant advantages in enhancing coverage and reliability [82–88]. In [83], authors investigated cooperative-NOMA with AF and DF relaying and derived the outage probability and asymptotic outage probability expressions. Considering the fact that multiple relays provide a significant performance gain in cooperative networks, special attention has been given to the cooperative NOMA with multiple relays and analysis of relay selection techniques [85–88]. In [85], the authors have provided a two-stage max-min relay selection scheme for the NOMA system with fixed power allocation at relays and different QoS requirements at users. In [85], the users are selected based on different QoS requirements, whereas in [86], authors have considered the users according to their channel condition, with fixed and adaptive power allocation at the relay node. In [87], the outage probability of cooperative NOMA with multiple half-duplex DF relays is analyzed. In [88], the outage probability and sum rate of cooperative NOMA with multiple half-duplex AF relays were studied, considering partial relay selection (PRS).

EH from radio frequency signals is considered a viable solution to provide additional lifespan to energy-constrained nodes. Hence, EH-based NOMA systems have gained research attention to meet the needs of 5G and beyond communications. In [89–94], the performance of cooperative NOMA has been studied with EH relaying. A cooperative NOMA with simultaneous wireless information and power transfer is studied in [89], where nearby users acting as EH relays assist the far away NOMA users. In [90], authors analyzed the performance of cooperative NOMA network with EH relaying over Rayleigh fading. In [91], a multi-user NOMA system is analyzed with an EH-powered relay node. In [92], the authors evaluated the NOMA system's performance with multiple EH relaying and derived the closed-form expressions of outage probability and ergodic capacity over the Rayleigh fading channel. In [93], the authors analyzed the NOMA system's outage probability with multiple EH AF relays with imperfect CSI and hardware impairment.

In the literature, most of the work assumes perfect knowledge of the CSI at the receiver, which is too idealistic for a practical system. However, in practice, knowledge of perfect CSI is unavailable at the receivers, which leads to CEE. CEE significantly deteriorates the performance of the system [51, 93, 95]. In [95], a closed-form expression of outage probability is derived from a downlink relay aided NOMA system with multiple users over Nakagami-m fading with imperfect CSI.

Contributions

To the best of the author's knowledge, the NOMA system's performance with DF-based multiple EH relays over Nakagami$-m$ fading channels has not been considered. Further, a detailed study on the impact of practical constraint, imperfect CSI at receiver nodes, and imperfect SIC is not available in the literature. Nakagami-m fading is considered due to its generalization to a variety of realistic fading channels, which includes Rayleigh fading channel with $m = 1$, recently for THz channels with $m = 3$ [96], and also for the UAV [97]. The main contributions of this work are:

- For the first time in EH-based multi-relay NOMA systems, the practical case of imperfect CSI at receiver nodes and imperfect SIC is considered, and its impact on system performance is analyzed.
- A DF-based cooperative multi-relay EH NOMA system employing relay selection is presented, and its performance is analyzed in terms of outage probability. Closed-form expressions are derived from the novel end-to-end (E2E) SNR of the system for both users, considering both perfect and imperfect cases.
- Further, the system performance at high SNR is analyzed by deriving the expression for the asymptotic outage probability, providing useful insights.
- The EH time fraction parameter (α) is optimized to maximize system throughput. The optimization problem is addressed using particle swarm optimization (PSO) under both perfect and imperfect CSI/SIC conditions.
- Rate analysis of the system is performed by deriving the closed-form expression of ergodic rate for both users, and the impact of imperfect CSI and SIC is analyzed.

4.2 System Model

A downlink cooperative NOMA system with EH-based multiple relays, as shown in Figure 4.1 is considered where a transmitter (S), i.e., the BS transmits messages to the downlink users, i.e., U_1 and U_2, with the help of cooperative relaying [85, 86]. Both users are ordered according to their channel condition. It is assumed that the

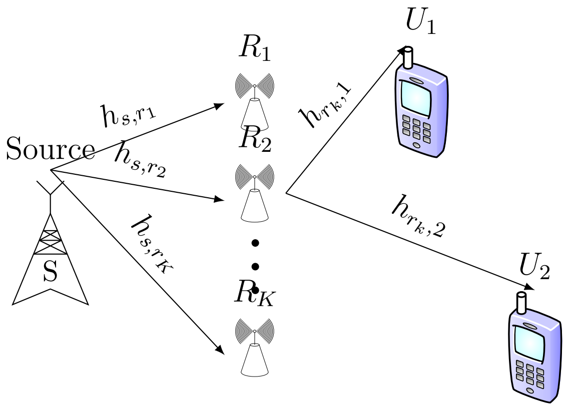

Figure 4.1: NOMA system with multiple EH relays

weak user (U_2) has a poor channel condition and the strong user (U_1) has a good channel condition. To facilitate cooperative relaying, it is also assumed that there are K numbers of relays in the system with DF relaying. Further, it is assumed that each node is equipped with a single antenna and operates in half-duplex mode. All the channel links are considered to be independent and identically distributed (i.i.d), which are modelled by Nakagami$-m$ fading, the channel coefficients corresponding to links are represented as $h_{i,j}$, $i \in (s, r_k)$ and $j \in (r_k, 1, 2)$, where the subscript $s, r_k, 1$ and 2 represent BS, R_k, U_1 and U_2 respectively. The $|h_{i,j}|$ is assumed to be Nakagami$-m$ with shape parameter $m_{i,j}$ and variance $\mathbb{E}[|h_{i,j}|^2] = \lambda_{i,j}$. Under imperfect CSI, according to minimum mean squared error (MMSE) estimation [22, 23, 98],

$$h_{i,j} = \hat{h}_{i,j} + \epsilon_{i,j}, \tag{4.1}$$

where $h_{i,j}$ is actual channel and $\hat{h}_{i,j}$ is the estimate of the channel $h_{i,j}$, where $h_{i,j}$ and $\hat{h}_{i,j}$ are jointly ergodic and stationary Gaussian process [24]. The $\epsilon_{s,r}$ is the CEE, which is assumed to be complex normal with mean zero and variance σ_e^2 [25]. The CEE arise due to the improper pilot pattern in channel estimation. A pilot pattern for estimating the channel should be performed as a function of coherence time and frequency. Otherwise, an irreducible error floor arises in the estimation.

Assuming that $\hat{h}_{i,j}$ and$\epsilon_{i,j}$ are independent[1], thus the estimated channel variance is given as $\hat{\lambda}_{i,j} = \lambda_{i,j} - \sigma_e^2$ [99]. In this work, the PRS is considered for the selection of the relay node, where the BS selects the relay that provides the best instantaneous channel gain between the BS and relays [100]. The BS continuously monitors the

[1]The independence of $\hat{h}_{i,j}$ and $\epsilon_{i,j}$ was not required, only that they were uncorrelated [22].

quality of the links between the BS and relays, and based on this information, the source selects the best link. The PRS scheme to select the best source to relay the link is expressed as

$$|\hat{h}_{s,r}|^2 = \arg \max_{k=1,2,\ldots,K} |\hat{h}_{s,r_k}|^2. \tag{4.2}$$

Furthermore, relays harvest the energy from the source transmitted signal. In this chapter, the TS protocol to harvest energy for αT block time is considered, where α $(0 \leq \alpha \leq 1)$ is the fraction of block time over which relay harvest the energy from a source transmitted signal. The remaining $(1-\alpha)T$ block time is assigned for the information transfer. The information transfer is completed in two blocks. The first half of time block $(1-\alpha)\frac{T}{2}$ is assigned for the source to relay transmission, and the remaining half $(1-\alpha)\frac{T}{2}$ for relay to users transmission. Thus, the harvested energy for αT time is given by [101]

$$E_H = P_s \mu |\hat{h}_{s,r}|^2 \alpha T, \tag{4.3}$$

where $0 \leq \mu \leq 1$ denotes energy conversion efficiency. The transmit power at R_k is expressed as $P_r = \frac{E_H}{(1-\alpha)T/2} = \frac{2P_s\mu|\hat{h}_{s,r}|^2\alpha}{1-\alpha}$. Initially, BS transmits the NOMA signal for users by performing power domain multiplexing and superposition coding. The transmitted signal is given by $x_s = \sum_{i=1}^{2} \sqrt{a_i} x_i$, where, x_i denotes complex modulated symbols with unit energy for U_i (i.e., $\mathbb{E}\left\{|x_i|^2\right\} = 1$). Further, a_i is the power allocation coefficients for x_i with $\sum_{i=1}^{2} a_i = 1$ and $a_i > 0$. The received signal at R_k is given by $y_{r_k} = (\hat{h}_{s,r} + \epsilon_{s,r_k})\sqrt{P_s} x_s + z_{s,r_k}$, where, P_s indicates the total transmit power at BS, $z_{s,r}$ represents AWGN with zero mean and variance σ_0^2. As DF transmission protocol is employed at the relay, R_k has to first decode both x_1 and x_2 before transmitting.The SINR at R_k to decode x_2 in the presence of imperfect CSI is given by

$$\gamma_{r_k,2} = \frac{|\hat{h}_{s,r}|^2 P_s a_2}{|\hat{h}_{s,r}|^2 P_s a_1 + P_s \sigma_e^2 + \sigma_0^2}. \tag{4.4}$$

According to SIC principle, x_1 is decoded by removing x_2 from y_{r_k}, the SIC is perfect, x_2 will be completely removed. Otherwise, decoding of x_1 will be carried out in the presence of residual interference due to imperfect SIC. Thus, SINR in the presence of imperfect CSI and imperfect SIC at R_k to decode x_1 is given by

$$\gamma_{r_k,1} = \frac{|\hat{h}_{s,r}|^2 P_s a_1}{|\hat{h}_{s,r}|^2 \beta P_s a_2 + P_s a_1 \sigma_e^2 + P_s \beta a_2 \sigma_e^2 + \sigma_0^2}. \tag{4.5}$$

where, β represents the residual interference due to imperfect SIC, $0 \leq \beta \leq 1$, and $\beta = 0$ refer to perfect SIC. After decoding x_2 and x_1, R_k will re-encode the information bit using superposition coding. Thus the transmitted signal by R_k is given by $x_r = \sum_{i=1}^{2} \sqrt{a_i} x_i$. The received signal at U_1 and U_2 is given as $y_l = (\hat{h}_{r_k,l} + \epsilon_{r_k,l})\sqrt{P_r} x_r + z_{r_k,l}$, $l = 1, 2$. Where P_r is harvested power at R_k, $z_{r_k,l}$ represent AWGN with zero mean and variance σ_0^2. Thereafter, U_1 will perform SIC to obtain its own symbol x_1. Thus, the SINR at U_1 to decode x_2 and x_1 under imperfect CSI and imperfect SCI are given as

$$\gamma_{1,2} = \frac{|\hat{h}_{r_k,1}|^2 P_r a_2}{|\hat{h}_{r_k,1}|^2 P_r a_1 + P_r \sigma_e^2 + \sigma_0^2}, \tag{4.6}$$

$$\gamma_{1,1} = \frac{|\hat{h}_{r_k,1}|^2 P_r a_1}{|\hat{h}_{r_k,1}|^2 \beta P_r a_2 + P_r a_1 \sigma_e^2 + P_r \beta a_1 \sigma_e^2 + \sigma_0^2}. \tag{4.7}$$

The SINR to decode x_2 at U_2 under imperfect CSI is given by

$$\gamma_{2,2} = \frac{|\hat{h}_{r_k,2}|^2 P_r a_2}{|\hat{h}_{r_k,2}|^2 P_r a_1 + P_r \sigma_e^2 + \sigma_0^2}. \tag{4.8}$$

4.3 Outage Probability Analysis

In this section, the outage probability expression for both NOMA users is derived. Outage probability gives the achievable maximum rate for error-free transmission [38]. The closed-form outage probability expressions for U_1 and U_2 under imperfect CSI/ SCI and perfect CSI/SIC are obtained in the following subsections.

4.3.1 Outage probability under imperfect CSI/SIC

Outage probability of U_1

U_1 is said to be in outage, when U_1 fails to detect either of the two symbols x_1 and x_2 at R_k and U_1. Therefore, the outage probability of U_1 is defined as

$$P_{out,1} = \Pr\left\{\gamma_{r_k,2} < \gamma_{th2},\, \gamma_{r_k,1} < \gamma_{th1},\, \gamma_{1,2} < \gamma_{th2},\, \gamma_{1,1} < \gamma_{th1}\right\}, \tag{4.9}$$

where, γ_{th1} and γ_{th2} are predefined SINR threshold. γ_{th1} and γ_{th2} can be represented as $\gamma_{th1} = 2^{\frac{2r_1}{1-\alpha}} - 1$ and $\gamma_{th2} = 2^{\frac{2r_2}{1-\alpha}} - 1$, where, r_1 and r_2 are the desired target rates.

Consider the outage probability definition given in (4.9). Substituting (4.4), (4.5), (4.6) and (4.7) in (4.9), on rearranging, the following expression is obtained

$$\begin{aligned} P_{out,1} =& 1 - \Pr\left\{|\hat{h}_{s,r}|^2 > \frac{\gamma_{th2}(P_s\sigma_e^2 + \sigma_0^2)}{(a_2 - a_1\gamma_{th2})P_s}, |\hat{h}_{r_k,1}|^2 > \frac{\gamma_{th2}(P_r\sigma_e^2 + \sigma_0^2)}{(a_2 - a_1\gamma_{th2})P_r},\right. \\ & \left. |\hat{h}_{s,r}|^2 > \frac{\gamma_{th1}(P_s\sigma_e^2(a_2 + \beta a_1) + \sigma_0^2)}{(a_1 - \beta a_2\gamma_{th1})P_s}, |\hat{h}_{r_k,1}|^2 > \frac{\gamma_{th1}(P_r\sigma_e^2(a_1 + \beta a_2) + \sigma_0^2)}{(a_1 - \beta a_2\gamma_{th1})P_r}\right\}, \end{aligned} \tag{4.10}$$

According to EH criteria, the transmitted power at the relay is given as $P_r = \frac{2P_s\mu|\hat{h}_{s,r}|^2\alpha}{1-\alpha}$. Substituting P_r in (4.10), and after some simplification (4.10) is given as

$$P_{out,1} = 1 - \Pr\left\{|\hat{h}_{s,r}|^2 > \psi,\, |h_{r_k,1}|^2 > \frac{\lambda_1}{|\hat{h}_{s,r}|^2} + \Omega_1,\, |h_{r_k,1}|^2 > \frac{\lambda_2}{|\hat{h}_{s,r}|^2} + \Omega_2\right\}, \tag{4.11}$$

where, $\Delta_1 = \frac{\gamma_{th2}(\sigma_e^2+(1/\rho))}{(a_2-a_1\gamma_{th2})}$, $\lambda_1 = \frac{\gamma_{th2}(1-\alpha)}{(a_2-a_1\gamma_{th2})\alpha\mu 2\rho}$, $\lambda_2 = \frac{\gamma_{th1}(1-\alpha)}{(a_1-a_2\beta\gamma_{th1})\alpha\mu 2\rho}$, $\Omega_1 = \frac{\gamma_{th2}\sigma_e^2}{a_2-a_1\gamma_{th2}}$, $\Omega_2 = \frac{\gamma_{th2}(a_1+a_2\beta)\sigma_e^2}{a_1-a_2\beta\gamma_{th2}}$, $\psi = \max\left[\Delta_1, \frac{\gamma_{th1}\left(P_s\sigma_e^2(a_1+a_2\beta)+\sigma_0^2\right)}{(a_1-a_2\beta\gamma_{th1})P_s}\right]$.

$$\begin{aligned} P_{out,1} =& 1 - \left[\Pr\left\{|\hat{h}_{s,r}|^2 > \psi,\, |h_{r_k,1}|^2 > \frac{\lambda_1}{|\hat{h}_{s,r}|^2} + \Omega_1,\, |\hat{h}_{s,r}|^2 > \frac{\lambda_2 - \lambda_1}{\Omega_1 - \Omega_2}\right\}\right. \\ & \left. + \Pr\left\{|\hat{h}_{s,r}|^2 > \psi,\, |h_{r_k,1}|^2 > \frac{\lambda_2}{|\hat{h}_{s,r}|^2} + \Omega_2,\, |\hat{h}_{s,r}|^2 < \frac{\lambda_2 - \lambda_1}{\Omega_1 - \Omega_2}\right\}\right]. \end{aligned} \tag{4.12}$$

Let $P_{out,1} = 1 - (A + B)$, where A and B are separately evaluated as follows. Assume the links in the network to be independent, $\gamma_{th1} < \frac{a_1}{a_2\beta}$, $\gamma_{th2} < \frac{a_2}{a_1}$, $\lambda_2 > \lambda_1$ and $\Omega_1 > \Omega_2$. Since i.i.d Nakagami fading is assumed, the channel power gains $|\hat{h}_{i,j}|$

are gamma functions. The PDF and CDF [102] of $|\hat{h}_{i,j}|^2$ with parameter $m_{i,j}$ and $\hat{\lambda}_{i,j}$ is given as

$$f_{|\hat{h}_{i,j}|^2}(x) = \left(\frac{m_{i,j}}{\hat{\lambda}_{i,j}}\right)^{m_{i,j}} \frac{x^{m_{i,j}-1}}{\Gamma(m_{i,j})} e^{\frac{-x m_{i,j}}{\hat{\lambda}_{i,j}}}, \tag{4.13}$$

$$F_{|\hat{h}_{i,j}|^2}(x) = 1 - e^{\frac{-x m_{i,j}}{\hat{\lambda}_{i,j}}} \sum_{n=0}^{m_{i,j}-1} \frac{1}{n!} \left(\frac{x m_{i,j}}{\hat{\lambda}_{i,j}}\right)^n, \tag{4.14}$$

Let $\hat{\beta}_{i,j} = \frac{m_{i,j}}{\hat{\lambda}_{i,j}}$, since PRS with K-relays is performed, the CDF and PDF of the $|\hat{h}_{s,r}|^2$ is given by

$$F_{|\hat{h}_{s,r}|^2}(x) = \left[1 - e^{-x\hat{\beta}_{s,r_k}} \sum_{n=0}^{m_{s,r_k}-1} \frac{1}{n!} \left(x\hat{\beta}_{s,r_k}\right)^n\right]^K, \tag{4.15}$$

$$\begin{aligned} f_{|\hat{h}_{s,r}|^2}(x) =& K\hat{\beta}_{s,r_k}^{m_{s,r_k}} \frac{x^{m_{s,r_k}-1}}{(m_{s,r_k}-1)!} e^{-x\hat{\beta}_{s,r_k}} \left[1 + \sum_{k=1}^{K-1} (-1)^k \binom{K-1}{k} e^{-kx\hat{\beta}_{s,r_k}}\right. \\ & \left.\left(\sum_{n=0}^{m_{s,r_k}-1} \frac{1}{n!} \left(x\hat{\beta}_{s,r_k}\right)^n\right)^k\right], \end{aligned} \tag{4.16}$$

By using the Binomial expression for the term $\left(\sum_{n=0}^{m_{s,r_k}-1} \frac{1}{n!} \left(x\hat{\beta}_{s,r_k}\right)^n\right)^k$, the Binomial expansion is given as [95]

$$\begin{aligned} =& \sum_{i_1=0}^{k} \sum_{i_2=0}^{k-i_2} \cdots \sum_{i_{m_{s,r_k}-1}=0}^{k-i_1 \cdots i_{m_{s,r_k}-2}} \binom{k}{i_1} \binom{k-i_1}{i_2} \cdots \\ & \binom{k-i_1-\ldots i_{m_{s,r_k}-2}}{i_{m_{s,r_k}-1}} \prod_{r=0}^{m_{s,r_k}-2} \left(\frac{(\hat{\beta}_{s,r_k}x)^r}{r!}\right)^{i_{r+1}} \left(\frac{\hat{\beta}_{s,r_k}^{m_{s,r_k}-1} x}{(m_{s,r_k}-1)!}\right)^{k-i_1-\ldots i_{m_{s,r_k}-1}} \end{aligned} \tag{4.17}$$

Substituting (4.17) in (4.16), the CDF is obtained. By utilizing the above equation, A is obtained as follows

$$A = \int_{x=\gamma}^{\infty} \left[1 - F_{r_k,1}\left(\frac{\lambda_1}{x} + \Omega_1\right)\right] f_{s,r_k}(x)dx, \tag{4.18}$$

$$A = \int_{x=\gamma}^{\infty} e^{-\hat{\beta}_{r_k,1}\left(\frac{\lambda_1}{x}+\Omega_1\right)} \sum_{n=0}^{m_{r_k,1}-1} \frac{K}{n!} \hat{\beta}_{s,r_k}^{m_{s,r_k}} e^{-x\hat{\beta}_{s,r_k}} \left(\hat{\beta}_{r_k,1}\left(\frac{\lambda_1}{x} + \Omega_1\right)\right)^n$$
$$\frac{x^{m_{s,r_k}-1}}{(m_{s,r_k}-1)!}\left[1 + \sum_{k=1}^{K-1}(-1)^k \binom{K-1}{k} e^{-kx\hat{\beta}_{s,r_k}} \bigcup_k \Xi_{1,k}\Xi_{2,k}x^{\bar{i}}\right] dx, \tag{4.19}$$

where $\gamma = \max\left[\psi, \left(\frac{\lambda_2-\lambda_1}{\Omega_1-\Omega_2}\right)\right]$, $\bigcup_k = \sum_{i_1=0}^{k}\sum_{i_2=0}^{k-i_2}\cdots\sum_{i_{m_{s,r_k}}=0}^{k-i_1\cdots i_{m_{s,r_k}-2}}$, $\Xi_{1,k} = \binom{k}{i_1}\binom{k-i_1}{i_2}\ldots\binom{k-i_1-\ldots i_{m_{s,r_k}-2}}{i_{m_{s,r_k}-1}}$, $\Xi_{2,k} = \prod_{r=0}^{m_{s,r_k}-2}\left(\frac{\hat{\beta}_{s,r_k}^{r}}{r!}\right)^{i_{r+1}}\left(\frac{\hat{\beta}_{s,r_k}^{m_{s,r_k}-1}}{(m_{s,r_k}-1)!}\right)^{k-i_1-\ldots i_{m_{s,r_k}-1}}$ and $\bar{i} = (m_{s,r_k}-1)(k-i_1) - (m_{s,r_k}-2)i_2 - (m_{s,r_k}-3)i_3 - \ldots i_{m_{s,r_k}-1}$. Using Binomial expansion on $\left(\frac{\lambda_1}{x} + \Omega_1\right)^n$, the above equation can further simplified as

$$A = e^{-\hat{\beta}_{r_k,1}\Omega_1} \sum_{n=0}^{m_{r_k,1}-1} \frac{1}{n!}\hat{\beta}_{r_k,1}^{n} K \hat{\beta}_{s,r_k}^{m_{s,r_k}} \frac{1}{(m_{s,r_k}-1)!} \sum_{j=0}^{n}\binom{n}{j}\lambda_1^j\Omega_1^{n-j}\left[\int_{x=\gamma}^{\infty} x^{m_{s,r_k}-j-1}\right.$$
$$e^{-x\hat{\beta}_{s,r_k}} e^{\frac{-\hat{\beta}_{r_k,1}\lambda_1}{x}} dx + \sum_{k=1}^{K-1}(-1)^k\binom{K-1}{k}\bigcup_k \Xi_{1,k}\Xi_{2,k}\int_{x=\gamma}^{\infty} e^{-x(k+1)\hat{\beta}_{s,r_k}} x^{m_{s,r_k}-j+\bar{i}-1}$$
$$\left. e^{\frac{-\hat{\beta}_{r_k,1}\lambda_1}{x}} dx\right]. \tag{4.20}$$

Now, using Taylor's series expansion, as $e^{\frac{-\hat{\beta}_{r_k,1}\lambda_1}{x}} = \sum_{l_1=0}^{N_t}\frac{(-1)^{l_1}}{l_1!}\left(\frac{\hat{\beta}_{r_k,1}\lambda_1}{x}\right)^{l_1}$ where $N_t \in \{2, 3, \ldots\infty\}$ and using [54, eq. (3.351.4)] the (4.20) can be simplified. Further, the B is simplified as follows

$$B = \int_{x=\psi}^{\frac{\lambda_2=\lambda_1}{\Omega_1-\Omega_2}} \left[1 - F_{r_k,1}\left(\frac{\lambda_2}{x} + \Omega_2\right)\right] f_{s,r}(x)dx. \tag{4.21}$$

The (4.21) can be simplified by following the same approach as used in (4.18), the obtained result $P_{out,1} = 1 - (A + B)$.

When $\gamma_{th2} < \frac{a_2}{a_1}$, $\gamma_{th1} < \frac{a_1}{\beta a_2}$, $\lambda_2 > \lambda_1$ and $\Omega_1 > \Omega_2$. The outage probability of U_1

under imperfect CSI and imperfect SIC is defined as

$$\begin{aligned} P_{out,1} =& 1 - \Bigg[e^{-\Omega_1 \hat{\beta}_{r_k,1}} A_1 \Omega_1^{n-j} \lambda_1^j \Big[\iota_1 \Big(\hat{\beta}_{r_k,1}\lambda_1 \Big)^{l_1} \hat{\beta}_{s,r_k}^{(j+l_1)} \Gamma\left(\kappa_1, \hat{\beta}_{s,r_k}\gamma\right) + A_2 \left(\hat{\beta}_{r_k,1}\lambda_1\right)^{l_2} \\ & \times \hat{\beta}_{s,r_k}^{(j+l_2-\bar{i})} \Gamma\left(\kappa_2, \hat{\beta}_{s,r_k}(k+1)\gamma\right) \iota_2 \left(k+1\right)^{-\kappa_2} \Big] + e^{-\Omega_2 \hat{\beta}_{r_k,1}} A_1 \Omega_2^{n-j} \lambda_1^j \\ & \times \Bigg[\iota_1 \left(\hat{\beta}_{r_k,1}\lambda_1\right)^{l_1} \hat{\beta}_{s,r_k}^{(j+l_1)} \Big[\Gamma\left(\kappa_1, \hat{\beta}_{s,r_k}\psi\right) - \Gamma\Big(\kappa_1, \frac{\hat{\beta}_{s,r_k}(\lambda_2-\lambda_1)}{\Omega_1-\Omega_2}\Big)\Big] \\ & + A_2 \iota_2 \left(\hat{\beta}_{r_k,1}\lambda_1\right)^{l_2} (k+1)^{-\kappa_2} \hat{\beta}_{s,r_k}^{(j+l_2-\bar{i})} \Big[\Gamma\Big(\kappa_2, (k+1)\hat{\beta}_{s,r_k}\psi\Big) \\ & - \Gamma\Big(\kappa_2, \frac{(k+1)\hat{\beta}_{s,r_k}(\lambda_2-\lambda_1)}{(\Omega_1-\Omega_2)}\Big)\Big]\Bigg]\Bigg]. \end{aligned} \tag{4.22}$$

where, $A_1 = \frac{K}{(m_{s,r_k}-1)!} \sum_{n=0}^{m_{r_k,1}-1} \sum_{j=0}^{n} \frac{1}{n!} \hat{\beta}_{r_k,1}^{n} \binom{n}{j}$, $A_2 = \sum_{k=1}^{K-1} \bigcup_k \Xi_{1,k} \Xi_{2,k} (-1)^k \binom{K-1}{k}$, $\kappa_1 = m_{s,r_k} - j - l_1$, $\kappa_2 = m_{s,r_k} - j - l_2 + \bar{i}$, $\lambda_1 = \frac{\gamma_{th2}\sigma_0^2(1-\alpha)}{(a_2-a_1\gamma_{th2})\alpha\mu 2\rho}$, $\lambda_2 = \frac{\gamma_{th1}(1-\alpha)}{(a_1-a_2\beta\gamma_{th1})\alpha\mu 2\rho}$, $\Omega_1 = \frac{\gamma_{th2}\sigma_e^2}{a_2-a_1\gamma_{th2}}$, $\Omega_2 = \frac{\gamma_{th2}(a_1+a_2\beta)\sigma_e^2}{a_1-a_2\beta\gamma_{th2}}$, $\gamma = \max\left[\psi, \left(\frac{\lambda_2-\lambda_1}{\Omega_1-\Omega_2}\right)\right]$, $\rho = \frac{P_s}{\sigma_0^2}$, $\hat{\beta}_{r_k,1} = \frac{m_{r_k,1}}{\hat{\lambda}_{r_k,1}}$, $\hat{\beta}_{s,r_k} = \frac{m_{s,r_k}}{\hat{\lambda}_{s,r_k}}$, $\psi = \max\left[\Delta_1, \frac{\gamma_{th1}\left(\sigma_e^2(a_1+a_2\beta)+(1/\rho)\right)}{(a_1-a_2\beta\gamma_{th1})}\right]$, $\Delta_1 = \frac{\gamma_{th2}\left(\sigma_e^2+(1/\rho)\right)}{(a_2-a_1\gamma_{th2})}$, $\iota_1 = \sum_{l_1=0}^{N_t} \frac{(-1)^{l_1}}{l_1!}$, $\iota_2 = \sum_{l_2=0}^{N_t} \frac{(-1)^{l_2}}{l_2!}$,$\bigcup_k = \sum_{i_1}^{k} \sum_{i_2}^{k-i_2} ... \sum_{i_{m_{s,r_k}}}^{k-i_1''' i_{m_{s,r_k}}-2}$,
$\Xi_{1,k} = \binom{k}{i_1} ... \binom{k-i_1-...i_{m_{s,r_k}}}{i_{m_{s,r_k}}}$, $\Xi_{2,k} = \prod_{n=0}^{m_{s,r_k}-2} \left(\frac{\hat{\beta}_{s,r_k}^{n}}{n!}\right)^{i_n+1} \left(\frac{\hat{\beta}_{s,r_k}^{m_{s,r_k}-1}}{(m_{s,r_k}-1)!}\right)^{k-i_1-...i_{m_{s,r_k}}-1}$ and $\bar{i} = (m_{s,r_k}-1)(k-i_1) - (m_{s,r_k}-2)i_2 - (m_{s,r_k}-3)i_3 - ...i_{m_{s,r_k}-1}$. Further, when $\gamma_{th2} > \frac{a_2}{a_1}$, $\gamma_{th1} > \frac{a_1}{\beta a_2}$, $P_{out,1} = 1$.

Outage probability of U_2

U_2 is said to be in outage, when U_2 fails to detect x_2 at R_k and U_2.

$$P_{out,2} = \Pr\left\{\gamma_{r_k,2} < \gamma_{th2},\ \gamma_{2,2} < \gamma_{th2}\right\}, \tag{4.23}$$

Substitute (4.4) and (4.8) in (4.23), after some manipulation (4.23) can be simplified as

$$P_{out,2} = 1 - \Pr\left\{|\hat{h}_{s,r}|^2 > \frac{\gamma_{th2}(P_s\sigma_e^2+\sigma_0^2)}{(a_2-a_1\gamma_{th2})P_s}, |\hat{h}_{r_k,2}|^2 > \frac{\gamma_{th2}(P_r\sigma_e^2+\sigma_0^2)}{(a_2-a_1\gamma_{th2})P_r}\right\}, \tag{4.24}$$

Substituting $P_r = \frac{2P_s\alpha\mu|\hat{h}_{s,r}|^2}{1-\alpha}$, (4.24) can be further reduced as

$$P_{out,2} = 1 - \Pr\left\{|\hat{h}_{s,r}|^2 > \Delta_1, |\hat{h}_{r_k,1}|^2 > \frac{\lambda_1}{|\hat{h}_{s,r}|^2} + \Omega_1\right\}, \tag{4.25}$$

$$P_{out,2} = 1 - \int_{x=\Delta_1}^{\infty} \left[1 - F_{r_k,2}\left(\frac{\lambda_1}{x} + \Omega_1\right)\right] f_{s,r}(x)dx. \tag{4.26}$$

The integration in (4.26) can be simply simplified by following the same approach as of (4.18) of Appendix A. The obtained closed-form expression is given as The outage probability of U_2 under imperfect CSI is given as

$$\begin{aligned} P_{out,2} = &1 - e^{-\Omega_1 \hat{\beta}_{r_k,2}} A_3 \Omega_1^{n-j} \lambda_1^j \Big[\iota_1 \left(\hat{\beta}_{r_k,2}\lambda_1\right)^{l_1} \hat{\beta}_{s,r_k}^{(j+l_1)} \Gamma\left(\kappa_1,\, \hat{\beta}_{s,r_k}\Delta_1\right) \\ &+ A_2 \iota_2 \left(\hat{\beta}_{r_k,2}\lambda_1\right)^{l_2} \hat{\beta}_{s,r_k}^{(j+l_2-\bar{\iota})} (k+1)^{-\kappa_2}\, \Gamma\left(\kappa_2,\, (k+1)\hat{\beta}_{s,r_k}\Delta_1\right)\Big], \end{aligned} \tag{4.27}$$

where $A_3 = \frac{K}{(m_{s,r_k}-1)!} \sum_{n=0}^{m_{r_k,2}-1} \sum_{j=0}^{n} \frac{1}{n!} \left(\frac{m_{r_k,2}}{\lambda_{r_k,2}}\right)^n \binom{n}{j}$. Further when $\gamma_{th2} > \frac{a_2}{a_1}$, $P_{out,2} = 1$.

4.3.2 Outage probability under perfect CSI/SIC

Outage probability of U_1

The outage probability of U_1 under perfect CSI and perfect SIC is obtained by considering the perfect channel estimation and perfect SIC at all nodes. The $|\hat{h}_{i,j}|^2 = |h_{i,j}|^2$ i.e., the CEE $\epsilon_{i,j} = 0$ and residual interference due to imperfect SIC $\beta = 0$.

Considering the perfect CSI and perfect SIC condition on the SINR's equation (4.4), (4.5), (4.6) and (4.7). The outage probability of U_1 under perfect SIC and perfect CSI is given as

$$\begin{aligned} P_{out,1}^{P} = &1 - \Pr\Big\{\frac{|h_{s,r}|^2 P_s a_2}{|h_{s,r}|^2 P_s a_1 + \sigma_0^2}. > \gamma_{th2}, \frac{|h_{r_k,1}|^2 P_r a_2}{|h_{r_k,1}|^2 P_r a_1 + \sigma_0^2} > \gamma_{th2}, \frac{|h_{s,r}|^2 P_s a_1}{\sigma_0^2} \\ &> \gamma_{th1}, \frac{|h_{r_k,1}|^2 P_r a_1}{\sigma_0^2}. > \gamma_{th1}\Big\}. \end{aligned} \tag{4.28}$$

substituting $P_r = \frac{2P_s\mu|h_{s,r}|^2\alpha}{1-\alpha}$ and after some manipulation, (5.16) further simplified as

$$P_{out,1}^{P} = 1 - \Pr\left\{|h_{s,r}|^2 > \Delta_3, |h_{r_k,1}| > \frac{\Delta_2}{|h_{s,r}|^2}\right\}, \tag{4.29}$$

where $\Delta_3 = \max[\frac{\gamma_{th2}\sigma_0^2}{(a_2-a_1\gamma_{th2})P_s}, \frac{\gamma_{th1}\sigma_0^2}{a_1 P_s}]$, $\Delta_2 = \max[\lambda_1, \frac{\gamma_{th1}(1-\alpha)}{a_1\alpha 2\mu P_s}]$. Let $P_{out,1}^{P} = 1 - D$, where D is evaluated as follow

$$D = \int_{x=\Delta_3}^{\infty} \left[1 - F_{r_k,1}\left(\frac{\Delta_2}{x}\right)\right] f_{s,r_k}(x)dx, \tag{4.30}$$

$$= \sum_{n=0}^{m_{r_k,1}-1} \frac{1}{(m_{s,r_k}-1)!}\left(\frac{m_{r_k,1}\Delta_2}{\lambda_{r_k,1}}\right)^n \left(\frac{m_{s,r_k}}{\lambda_{s,r_k}}\right)^{m_{s,r_k}} \frac{K}{n!}\Bigg[\int_{x=\Delta_3}^{\infty} x^{m_{s,r_k}-n-1} e^{\frac{m_{s,r_k}x}{\lambda_{s,r_k}}}$$
$$e^{\frac{-m_{r_k,1}\Delta_2}{\lambda_{r_k,1}x}} dx + \sum_{k=1}^{K-1}(-1)^k \binom{K-1}{k} \bigcup_k \Xi_{1,k}\Xi_{2,k} \int_{x=\Delta_3}^{\infty} e^{\frac{-x(k+1)m_{s,r_k}}{\lambda_{s,r_k}}} x^{m_{s,r_k}-n+\bar{i}-1}$$
$$e^{\frac{-m_{r_k,1}\Delta_2}{\lambda_{r_k,1}x}} dx\Bigg]. \tag{4.31}$$

The integration in (4.31), is same as in (4.20) in appendix A. Hence, D can be obtained following the similar procedure as adopted in (4.20). The outage probability of U_1 under perfect CSI/SIC is expressed as

$$P_{out,1}^{P} = 1 - B_1\left(\beta_{r_k,1}\Delta_2\right)^n \Big[\iota_1\left(\beta_{r_k,1}\Delta_2\right)^{l_1}\Gamma\left(\kappa_3,\ \beta_{s,r_k}\Delta_3\right)\beta_{s,r_k}^{(n+l_1)} + A_2\iota_2\left(\beta_{r_k,1}\Delta_2\right)^{l_2}$$
$$(k+1)^{-\kappa_4}\ \beta_{s,r_k}^{(n+l_2-\bar{i})}\Gamma\left(\kappa_4,\ (k+1)\beta_{s,r_k}\Delta_3\right)\Big], \tag{4.32}$$

where $B_1 = \frac{K}{(m_{s,r_k}-1)!}\sum_{n=0}^{m_{r_k,1}-1}\frac{1}{n!}$, $\kappa_3 = m_{s,r_k} - n - l_1$, $\kappa_4 = m_{s,r_k} - n - l_2 + \bar{i}$, $\Delta_3 = \max[\frac{\gamma_{th2}}{(a_2-a_1\gamma_{th2})\rho}, \frac{\gamma_{th1}}{a_1\rho}]$, $\Delta_2 = \max[\lambda_1, \frac{\gamma_{th1}(1-\alpha)}{a_1\alpha 2\mu\rho}]$.

Outage probability of U_2

The outage probability of U_2 under perfect CSI is obtained by considering the perfect CSI assumption as used in $P_{out,1}^{P}$. Thus, the outage probability of U_2 under perfect CSI is given as

$$P_{out,2}^{P} = 1 - B_2\left(\beta_{r_k,2}\lambda_1\right)^n \Big[\iota_1\left(\beta_{r_k,2}\lambda_1\right)^{l_1}\left(\beta_{s,r_k}\right)^{n+l_1}\Gamma\left(\kappa_3,\chi\right) + A_2\iota_2\left(k+1\right)^{\kappa_4}\left(\beta_{r_k,2}\lambda_1\right)^{l_2}$$
$$\left(\beta_{s,r_k}\right)^{n+l_2-\bar{i}}\Gamma\left(\kappa_4,(k+1)\chi\right)\Big], \tag{4.33}$$

where $B_2 = \frac{K}{(m_{s,r_k}-1)!}\sum_{n=0}^{m_{r_k,2}-1}\frac{1}{n!}$, $\chi = \frac{m_{s,r_k}\gamma_{th2}}{\lambda_{s,r_k}(a_2-a_1\gamma_{th2})\rho}$. Further, when $\gamma_{th2} > \frac{a_2}{a_1}$, $P_{out,2}^{P} = 1$.

4.4 Asymptotic Outage Probability Analysis

In this section, an approximation of the outage probability at a high SNR region is provided. The asymptotic outage probability is obtained by considering the $\rho \to \infty$. Further, at high SNR, the approximated CDF is given as $F(x) \underset{x\to 0}{\approx} \frac{1}{m_{i,j}!}\left(\beta_{i,j}x\right)^{m_{i,j}}$ [93].

4.4.1 Asymptotic outage probability under imperfect CSI/SIC

Asymptotic outage probability of U_1

At high SNR, the asymptotic outage probability of U_1 is obtained by utilizing the approximated CDF equation in (4.11) and equating $\frac{1}{\rho} \to 0$ in λ_1 and λ_2. The asymptotic outage probability of U_1 under imperfect CSI/SIC is given as

$$P_{out,1}^{asy} = 1 - \left[\left(1 - \frac{1}{m_{s,r_k}!}\left(\hat{\beta}_{s,r_k}\psi\right)^{m_{s,r_k}}\right)^{K} e^{-\hat{\beta}_{r_k,1}a}\sum_{n=0}^{m_{r_K,1}-1}\frac{1}{n!}\left(\hat{\beta}_{r_k,1}a\right)^{n}\right], \quad (4.34)$$

where, $a = \max[\Omega_1, \Omega_2]$.

Asymptotic outage probability of U_2

The asymptotic outage probability of U_2 is obtained by approximating the CDF equation and equating $\frac{1}{\rho} \to 0$ in λ_1. The asymptotic outage probability of U_2 under imperfect CSI is given as

$$P_{out,2}^{asy} = 1 - \left[\left(1 - \frac{1}{m_{s,r_k}}\left(\hat{\beta}_{s,r_k}\Delta_1\right)^{m_{s,r_k}}\right)^{K} e^{-\hat{\beta}_{r_k,2}\Omega_1}\sum_{n=0}^{m_{r_K,2}-1}\frac{1}{n!}\left(\hat{\beta}_{r_k,2}\Omega_1\right)^{n}\right]. \quad (4.35)$$

4.4.2 Asymptotic outage probability under perfect CSI/SIC

Asymptotic outage probability of U_1

The asymptotic outage probability of U_1 under perfect CSI and SIC is obtained by utilizing the approximated CDF. The asymptotic outage probability of U_1 under perfect CSI/SIC is given by

$$P_{out,1}^{P,asy} = \left(\frac{1}{m_{s,r_k}!} \left(\beta_{s,r_k}\Delta_3\right)^{m_{s,r_k}} \right)^K + \frac{\left(\beta_{r_k,1}\Delta_2\right)^{m_{r_k,1}}}{(m_{s,r_k}-1)!} \frac{K}{m_{r_k,1}!} \big[\beta_{s,r_k}^{m_{r_k,1}} \Gamma\left(\kappa_5, \beta_{s,r_k}\Delta_3\right) + A_2 \beta_{s,r_k}^{(m_{r_k,1}-\bar{i})} \left(k+1\right)^{-(\kappa_5+\bar{i})} \Gamma\left(\kappa_5+\bar{i}, (k+1)\beta_{s,r_k}\Delta_1\right) \big]. \tag{4.36}$$

where $\kappa_5 = m_{s,r_k} - m_{r_k,1}$.

Asymptotic outage probability of U_2

The asymptotic outage probability of U_2 under perfect CSI is obtained by approximating CDF. The asymptotic outage probability of U_2 under perfect CSI is given by

$$P_{out,2}^{P,asy} = \left(\frac{1}{m_{s,r_k}!} \chi^{m_{s,r_k}} \right)^K + \frac{K\left(\beta_{r_k,2}\lambda_1\right)^{m_{r_k,2}}}{(m_{s,r_k}-1)! m_{r_k,2}!} \big[\beta_{s,r_k}^{m_{r_k,2}} \Gamma\left(\kappa_6, \chi\right) + A_2 \left(k+1\right)^{-(\kappa_6+i)} \left(\beta_{s,r_k}\right)^{m_{r_k,2}-\bar{i}} \Gamma\left(\kappa_6+\bar{i}, (k+1)\chi\right) \big]. \tag{4.37}$$

where $\kappa_6 = m_{s,r_k} - m_{r_k,2}$.

4.5 Optimization of fraction of EH time

In this section, the fraction of EH time (α) is optimized in order to maximize the throughput of the system. The system throughput of a dual-hop system in a delay-limited transmission mode for a fixed transmission rate from the outage probability is given as [103]

$$\tau = \frac{(1-P_{out,1})r_1(1-\alpha)}{2} + \frac{(1-P_{out,2})r_2(1-\alpha)}{2}, \tag{4.38}$$

where $\lambda_{th1} = 2^{\frac{2r_1}{1-\alpha}} - 1$ and $\lambda_{th2} = 2^{\frac{2r_2}{1-\alpha}} - 1$ are the threshold SNR for a fixed rate r_1 and r_2 respectively. Maximum throughput can be attained by optimizing α. The objective function for maximizing throughput can be formulated as follows

$$\begin{aligned} \alpha^* &= \arg\max_{\alpha} \tau \quad \text{subject to} \quad 0 < \alpha < 1, \\ \alpha^* &= \arg\max_{\alpha} \quad \frac{(1-P_{out,1})R_1(1-\alpha)}{2} \\ &\qquad + \frac{(1-P_{out,2})R_2(1-\alpha)}{2} \\ &\text{subject to} \quad 0 < \alpha < 1 \end{aligned} \tag{4.39}$$

The objective function in (4.39) is nonlinear and non-convex. Thus, a low-complexity optimum fraction of EH time that maximizes the system throughput based on a PSO algorithm [104] is proposed, wherein the optimal solution from each iteration in the search space is based on a swarm of particles. It is noteworthy that PSO is chosen due to its fast convergence and stability [105, 106]. The algorithm for determining the PSO-based solution is shown in Algorithm 1. Let $\tau(\alpha)$ denote the objective value of solution α as given in (4.38). Let α_i denotes the position of particle i $(1 \le i \le MAX_{particles})$, where $MAX_{particles}$ denotes the number of particles.

4.6 Ergodic Rate Analysis

In this section, the ergodic rate expression for NOMA users is derived. The achievable rate for error-free transmission is given as

$$\begin{aligned} R_i &= E\left[\frac{1-\alpha}{2}\log_2(1+\gamma_{i,j})\right], \\ &= \frac{1-\alpha}{2\ln 2}\int_{z=0}^{\infty}\frac{1-F_{i,j}(z)}{1+z}dz. \end{aligned} \tag{4.40}$$

where $F_{i,j}$ represents CDF of SNR $\gamma_{i,j}$. The closed-form ergodic rate expressions for U_1 and U_2 are obtained in the following subsections.

Algorithm 6: PSO algorithms

Input: Lower Bound of Decision Variables = 0, Upper Bound of Decision Variables = 1,

Output: the best fitness value (optPosition) and the corresponding solution (optcost)

Initialize $GlobalBest = -Infinity$

for *each particle* $i \leq MAX_{particles}$ **do**

  initialize α_i, in the interval of $[0, 1]$ randomly

  initialize velocity, $v_i = 0$

  Compute the fitness value of particle i, $\tau(\alpha_i)$ and set the best solution of particle i as $BestCost_i$ and corresponding position $BestPosition_i$.

  if *the* $BestCost_i$ *is greater than the* $GlobalBest$ **then**

    set current value as the new $GlobalBest$ value and corresponding position $GlobalPosition$

  end

end

for $t \leq 20$ **do**

  for *each particle* $i \leq MAX_{particles}$ **do**

    calculate the velocity of particle i

    $v_i = v_i + 2*$random function in the interval of $[0, 1] \times (BestPosition_i - \alpha_i) + 2\times$random function in the interval of $[0,\ 1]*(GlobalPosition - \alpha_i)$

    update the particle position

    $\alpha_i = \alpha_i + v_i$;

    $\alpha_i = max(\alpha_i, 0)$;

    $\alpha_i = min(\alpha_i, 1)$

    calculate the fitness value $\tau(\alpha_i)$ according to new position

    if *the fitness value is greater than the best fitness value in history* **then**

      set current value as the new $BestCost_i$ of particle

    end

    if *the fitness value is greater than the global best value in history* **then**

      set current value as the new $GlobalBest$ value and corresponding position $GlobalPosition$

    end

  end

  set optcost= $GlobalBest$ and optPosition= $GlobalPosition$

end

4.6.1 Ergodic rate under imperfect CSI/SIC

Ergodic rate of U_1

The ergodic rate of U_1 is defined as

$$R_1 = E\left[\frac{1-\alpha}{2}\log_2\left(1+\min(\gamma_{r_k,1},\gamma_{1,1})\right)\right], \tag{4.41}$$

$$\begin{aligned}R_1 =& E\Bigg[\frac{1-\alpha}{2}\log_2(1+\min(\frac{|\hat{h}_{s,r}|^2 P_s a_1}{|\hat{h}_{s,r}|^2\beta P_s a_2 + P_s\sigma_e^2(\beta a_2 + a_1)+\sigma_0^2},\\ &\frac{|\hat{h}_{r_k,1}|^2 P_r a_1}{|\hat{h}_{r_k,1}|^2\beta P_r a_2 + P_r\sigma_e^2(\beta a_2 + a_1)+\sigma_0^2})\Bigg].\end{aligned} \tag{4.42}$$

Considering the practical scenario, the harvested energy at the relay is always small. Hence, the transmit power of the relay is much lower than that of the source. Thus, it is assumed that the SINR at the destinations is lower than the SINR at the relay [92].

$$\frac{|\hat{h}_{s,r}|^2 P_s a_1}{|\hat{h}_{s,r}|^2\beta P_s a_2 + P_s\sigma_e^2(\beta a_2 + a_1)+\sigma_0^2} > \frac{|\hat{h}_{r_k,1}|^2 P_r a_1}{|\hat{h}_{r_k,1}|^2\beta P_r a_2 + P_r\sigma_e^2(\beta a_2 + a_1)+\sigma_0^2}. \tag{4.43}$$

Therefore, (4.42) will reduce to

$$R_1 = E\left[\frac{1-\alpha}{2}\log_2\left(1+\frac{|\hat{h}_{r_k,1}|^2 P_r a_1}{|\hat{h}_{r_k,1}|^2\beta P_r a_2 + P_r\sigma_e^2(\beta a_2 + a_1)+\sigma_0^2}\right)\right], \tag{4.44}$$

After some manipulation and by using (4.40), the above equation can be further simplified as

$$R_1 = \frac{1-\alpha}{2\ln 2}\int_{z=0}^{\infty}\frac{1-F_P(z)}{1+z}dz - \frac{1-\alpha}{2\ln 2}\int_{z=0}^{\infty}\frac{1-F_Q(z)}{1+z}dz, \tag{4.45}$$

where $P = |\hat{h}_{r_k,1}|^2 P_r(\beta a_2 + a_1) + P_r\sigma_e^2(\beta a_2 + a_1)$ and $Q = |\hat{h}_{r_k,1}|^2\beta P_r a_2 + P_r\sigma_e^2(\beta a_2 + a_1)$. After some manipulation and using [54, eq.(3.471.9)], the CDF of P and Q are given as follow

$$F_P(z) = 1 - 2e^{\hat{\beta}_{r_k,1}\sigma_e^2} A_1 (-\sigma_e^2)^{n-j} \hat{\beta}_{s,r_k}^{m_{s,r_k}} \left(\frac{z}{\zeta}\right)^j \Bigg[\Big(\frac{\hat{\beta}_{r_k,1} z}{\hat{\beta}_{s,r_k}\zeta}\Big)^{\frac{\tau_1}{2}} K_{\tau_1}\left(2\sqrt{\xi_1 z}\right) + A_2 \Big(\frac{\hat{\beta}_{r_k,1}}{\hat{\beta}_{s,r_k}}\Big)^{\frac{\tau_1+\bar{i}}{2}} \left(\frac{z}{\zeta(k+1)}\right)^{\frac{\tau_1+\bar{i}}{2}} K_{\tau_1+\bar{i}}\left(2\sqrt{\xi_1 z(k+1)}\right)\Bigg], \tag{4.46}$$

where $\tau_1 = m_{s,r_k} - j$, $\xi_1 = \frac{\hat{\beta}_{r_k,1}\hat{\beta}_{s,r_k}}{\zeta}$ and $\zeta = \frac{2\rho\mu\alpha(a_1+\beta a_2)}{1-\alpha}$.

$$F_Q(z) = 1 - 2e^{\hat{\beta}_{r_k,1}\xi_3} A_1 (-\xi_3)^{n-j} \hat{\beta}_{s,r_k}^{m_{s,r_k}} \left(\frac{z}{\bar{\zeta}}\right)^j \Bigg[K_{\tau_1}\left(2\sqrt{\xi_2 z}\right) \Big(\frac{\hat{\beta}_{r_k,1} z}{\hat{\beta}_{s,r_k}\bar{\zeta}}\Big)^{\frac{\tau_1}{2}} + A_2 \Big(\frac{\hat{\beta}_{r_k,1}}{\hat{\beta}_{s,r_k}}\Big)^{\frac{\tau_1+\bar{i}}{2}} \left(\frac{z}{\bar{\zeta}(k+1)}\right)^{\frac{\tau_1+\bar{i}}{2}} K_{\tau_1+\bar{i}}\left(2\sqrt{\xi_2 z(k+1)}\right)\Bigg], \tag{4.47}$$

where $\xi_2 = \frac{\hat{\beta}_{r_k,1}\hat{\beta}_{s,r_k}}{\bar{\zeta}}$, $\xi_3 = \frac{\sigma_e^2(a_1+\beta a_2)}{\beta a_2}$ and $\bar{\zeta} = \frac{2\rho\mu\alpha\beta a_2}{1-\alpha}$. Further, substituting (4.46) and (4.47) in (4.45), and using [54, eq. (7.811.5), (9.34.3)], after some manipulation the ergodic rate of U_1 is given as

$$R_1 = \frac{1-\alpha}{2\ln 2} I_1 \tag{4.48}$$

where I_1 is defined as

$$I_1 = e^{\hat{\beta}_{r_k,1}\sigma_e^2} A_1 (-\sigma_e^2)^{n-j} \left(\frac{1}{\zeta}\right)^j \Bigg[\left(\frac{\hat{\beta}_{r_k,1}}{\zeta}\right)^{-j} G^{1\,3}_{3\,1}\left({}^{0}_{0,m_{s,r_k},j}\,\middle|\,\xi_1\right) + A_2 \left(\frac{\hat{\beta}_{r_k,1}}{\zeta}\right)^{-j} \left(\frac{1}{k+1}\right)^{m_{s,r_k}+\bar{i}} \hat{\beta}_{s,r_k}^{-\bar{i}} G^{1\,3}_{3\,1}\left({}^{0}_{0,m_{s,r_k}+\bar{i},j}\,\middle|\,\xi_1(k+1)\right)\Bigg] - e^{\xi_3\hat{\beta}_{r_k,1}} A_1 (-\xi_3)^{n-j} \left(\frac{1}{\bar{\zeta}}\right)^j \Bigg[\left(\frac{\hat{\beta}_{r_k,1}}{\bar{\zeta}}\right)^{-j} G^{1\,3}_{3\,1}\left({}^{0}_{0,m_{s,r_k},j}\,\middle|\,\xi_2\right) + A_2 \left(\frac{\hat{\beta}_{r_k,1}}{\bar{\zeta}}\right)^{-j} \left(\frac{1}{k+1}\right)^{m_{s,r_k}+\bar{i}} \hat{\beta}_{s,r_k}^{-\bar{i}} G^{1\,3}_{3\,1}\left({}^{0}_{0,m_{s,r_k}+\bar{i},j}\,\middle|\,\xi_2(k+1)\right)\Bigg]. \tag{4.49}$$

Ergodic rate of U_2

The ergodic rate of U_2 is defined as

$$R_2 = E\left[\frac{1-\alpha}{2}\log_2\left(1+\min(\gamma_{r_k,2},\gamma_{2,2})\right)\right], \tag{4.50}$$

Substituting (4.4) and (4.8) in (4.50), and by employing the same approach as of U_1, the ergodic rate of U_2 is given by

$$R_2 = \frac{1-\alpha}{2\ln 2} J_1, \tag{4.51}$$

where J_1 is defined as

$$\begin{aligned} J_1 =& e^{\hat{\beta}_{r_k,2}\sigma_e^2} A_3 (-\sigma_e^2)^{n-j} \left(\frac{1}{\nu}\right)^j \Bigg[\left(\frac{\hat{\beta}_{r_k,2}}{\nu}\right)^{-j} G^{\,1\,3}_{\,3\,1}\left({}^{\;\;0}_{0,m_{s,r_k},j} \middle| \xi_5 \right) + A_2 \\ & \left(\frac{\hat{\beta}_{r_k,2}}{\nu}\right)^{-j} \left(\frac{1}{k+1}\right)^{m_{s,r_k}+\bar{i}} \hat{\beta}_{s,r_k}^{-\bar{i}} G^{\,1\,3}_{\,3\,1}\left({}^{\;\;0}_{0,m_{s,r_k}+\bar{i},j} \middle| \xi_5(k+1) \right) \Bigg] - e^{\frac{\hat{\beta}_{r_k,2}\sigma_e^2}{a_1}} A_3 \\ & \left(\frac{-\sigma_e^2}{a_1}\right)^{n-j} \left(\frac{1}{\bar{\nu}}\right)^j \Bigg[G^{\,1\,3}_{\,3\,1}\left({}^{\;\;0}_{0,m_{s,r_k},j} \middle| \xi_6 \right) \left(\frac{\hat{\beta}_{r_k,2}}{\bar{\nu}}\right)^{-j} + A_2 \left(\frac{\hat{\beta}_{r_k,2}}{\bar{\nu}}\right)^{-j} \left(\frac{1}{k+1}\right)^{m_{s,r_k}+\bar{i}} \\ & \hat{\beta}_{s,r_k}^{-\bar{i}} G^{\,1\,3}_{\,3\,1}\left({}^{\;\;0}_{0,m_{s,r_k}+\bar{i},j} \middle| \xi_6(k+1) \right) \Bigg]. \end{aligned} \tag{4.52}$$

where $\nu = \frac{2\rho\mu\alpha}{1-\alpha}$ and $\bar{\nu} = \frac{2\rho a_1 \mu\alpha}{1-\alpha}$.

4.6.2 Ergodic rate under perfect CSI/SIC

Ergodic rate of U_1

The ergodic rate of U_1 is obtained by employing the same approach as of U_1 under imperfect CSI/SIC. Under the assumption of perfect CSI/SIC, the $|\hat{h}_{i,j}|^2 = |h_{i,j}|^2$ i.e., the CEE $\epsilon_{i,j} = 0$ and residual interference due to imperfect SIC $\beta = 0$. Substituting the SNR equation under the assumption of perfect CSI/SIC in (4.41), and employing the same approach as of U_1 under imperfect CSI/SIC, the following expression is obtained

$$R_1^P = \mathbb{E}\left[\frac{1-\alpha}{2} \log_2\left(1 + \frac{|h_{r_k,1}|^2 P_r a_1}{\sigma_0^2}\right)\right], \tag{4.53}$$

After some simplification and by using (4.40), the above equation can be further simplified as

$$R_1^P = \frac{1-\alpha}{2\ln 2} \int_{z=0}^{\infty} \frac{1-F_S(z)}{1+z} dz \tag{4.54}$$

where $S = |h_{r_k,1}|^2 P_r a_1$.

$$F_S(z) = P\{S < z\},$$
$$= P\{|h_{r_k,1}|^2 P_r a_1 < z\}, \tag{4.55}$$

Substituting $P_r = \frac{2P_s\mu|h_{s,r}|^2\alpha}{1-\alpha}$ and after simplification, (4.55) further simplified as

$$F_S(z) = 1 - P\{|h_{s,r_k}|^2|h_{r_k,1}|^2\bar{\nu} > z\}. \tag{4.56}$$

After simplification and utilizing [54, eq. (3.471.9)], the CDF of S is given as follows

$$F_S(z) =1 - 2B_1\beta_{r_k,1}^{n}\beta_{s,r_k}^{m_{s,r_k}}\left(\frac{z}{\bar{\nu}}\right)^n\Bigg[\left(\frac{\beta_{r_k,1}z}{\beta_{s,r_k}\bar{\nu}}\right)^{\frac{\tau_2}{2}}K_{\tau_2}\left(2\sqrt{\xi_4 z}\right)+A_2\left(\frac{\beta_{r_k,1}}{\beta_{s,r_k}}\right)^{\frac{\tau_2+\bar{i}}{2}}$$
$$\left(\frac{z}{\bar{\nu}(k+1)}\right)^{\frac{\tau_2+\bar{i}}{2}}K_{\tau_2+\bar{i}}\left(2\sqrt{\xi_4 z(k+1)}\right)\Bigg], \tag{4.57}$$

where $\tau_2 = m_{s,r_k} - n$, $\xi_4 = \frac{\beta_{s,r_k}\beta_{r_k,1}}{\bar{\nu}}$. Further, substituting (4.57) in (4.54), and using [54, eq. (7.811.5), (9.34.3)], after simplification, the ergodic rate of U_1 under perfect CSI/SIC is given as

$$R_1^P =\frac{1-\alpha}{2\ln 2}B_1\Bigg[G_{3\ 1}^{1\ 3}\left({}_{0,m_{s,r_k},n}^{\quad 0}\Big|\xi_4\right)+A_2\beta_{s,r_k}^{-\bar{i}}\left(\frac{1}{k+1}\right)^{m_{s,r_k}+\bar{i}}G_{3\ 1}^{1\ 3}\left({}_{0,m_{s,r_k}+\bar{i},n}^{\quad 0}\Big|\xi_4\right)\Bigg].$$

Ergodic rate of U_2

The ergodic rate of U_2 under perfect CSI is obtained by substituting the SINR under the perfect CSI assumption in (4.50). By employing the same approach as of U_1, the ergodic rate of U_2 under perfect CSI is given as

$$R_2^P =\frac{1-\alpha}{2\ln 2}\int_{z=0}^{\infty}\frac{1-F_U(z)}{1+z}dz - \frac{1-\alpha}{2\ln 2}\int_{z=0}^{\infty}\frac{1-F_V(z)}{1+z}dz, \tag{4.58}$$

where $U = |h_{r_k,2}|^2 P_r$ and $V = |h_{r_k,2}|^2 a_1 P_r$. By employing the same approach as of U_1 under perfect CSI/SIC, and after simplification, the ergodic rate of U_2 under perfect CSI is given as

$$
\begin{aligned}
R_2^P =& \frac{1-\alpha}{2\ln 2}\Bigg[B_2\Bigg(G_{3\,1}^{1\,3}\left({}_{0,m_{s,r_k},n}^{0}\middle|\xi_5\right) + A_2\beta_{s,r_k}^{-\bar{i}}\left(\frac{1}{k+1}\right)^{m_{s,r_k}+\bar{i}} \\
& G_{3\,1}^{1\,3}\left({}_{0,m_{s,r_k}+\bar{i},n}^{0}\middle|\xi_5(k+1)\right)\Bigg) - B_2\Bigg(G_{3\,1}^{1\,3}\left({}_{0,m_{s,r_k},n}^{0}\middle|\xi_6\right) + A_2\left(\frac{1}{k+1}\right)^{m_{s,r_k}+\bar{i}} \\
& \beta_{s,r_k}^{-\bar{i}}G_{3\,1}^{1\,3}\left({}_{0,m_{s,r_k}+\bar{i},n}^{0}\middle|(k+1)\xi_6\right)\Bigg)\Bigg],
\end{aligned} \tag{4.59}
$$

where $\xi_5 = \frac{\beta_{s,r_k}\beta_{r_k,2}}{\nu}$ and $\xi_6 = \frac{\beta_{s,r_k}\beta_{r_k,2}}{\bar{\nu}}$.

4.7 Numerical and Simulation Results

In this section, numerical and simulation results are presented to evaluate the impact of imperfect CSI/SIC, the number of relays, EH time fraction (α) and σ_e^2 on the considered NOMA system. Unless specified, the system parameters are as follows. The target data rate $r_2 = r_1 = 0.5$ bpcu, $\alpha = 0.35$, energy conversion efficiency $\mu = 0.9$, $m_{i,j} = 2$, $\beta = 0.15$, the channel gains $\lambda_{s,r_k} = \lambda_{r_k,1} = 1$, $\lambda_{r_k,2} = 0.5$, $\sigma_e^2 = 0.01$, $a_1 = 0.3$ and $MAX_{particles} = 30$. [92]. The correctness of the derived analytical expressions is validated through Monte-Carlo simulations. Simulations are performed using Matlab, and analytical results are obtained using Mathematica. In the figures, (Sim.) denotes the Matlab simulation result.

Analysis of outage probability of U_1 and U_2

Impact imperfect CSI/SIC

In Figure 4.2, the outage probability experienced by U_1 and U_2 under imperfect CSI/SIC is compared with perfect CSI/SIC for the considered NOMA system. Results show a significant impact on the outage probability of both users due to imperfect CSI/SIC. It is observed that at the outage of 10^{-1} with K=2, U_1 with perfect CSI/SIC provides SNR gain of 5 dB over imperfect CSI/SIC case and U_2 with perfect CSI/SIC provides SNR gain of 10 dB over imperfect CSI/SIC. Whereas, at a high SNR regime, the outage probability of users with imperfect CSI/SIC suffers an outage floor and reaches a constant value of 0.038 and 0.12 for U_1 and U_2, respectively. With the increase in SNR, CEE increases and thus limits outage probability to further decrease and maintains a constant value for both users under imperfect CSI. However, in U_1, the residual interference due to imperfect SIC also increases with the increase in the SNR, thus causing degradation in the outage probability of U_1.

Impact of number of relays (K)

Figure 4.3 investigates the impact of the total number of active relay nodes in the network on U_1 and U_2. From the figure, a performance gain is observed as the K increases. A gain of 3 dB is observed for both users under perfect CSI/SIC, with the increase in relays from 2 to 5 for an outage probability of 10^{-2}. In the case of imperfect CSI/SIC, an SNR gain of 2 dB is observed at an outage probability of 0.1 and 0.2 for U_1 and U_2, respectively. Whereas at a high value of SNR, due to the presence of CEE and residual interference due to imperfect SCI performance, the gain is not observed with the increase in K. It is also observed that the analytical results are perfectly matching with the simulation result. Further, the derived asymptotic outage results match the derived analytical and simulation results at a high SNR value, which validates our results.

Impact of CEE

Figure 4.4 investigates the impact of CEE σ_e^2 on U_1 and U_2 with the fixed residual interference due to SIC error β. It is observed the outage floor decreases with a decrease in σ_e^2 and approaches towards perfect CSI/SIC case for both the users. In U_1, for high CEE values $\sigma_e^2 = 0.01$ and $\sigma_e^2 = 0.005$, perfect CSI/SIC has an SNR gain of 4 dB and 3 dB for an outage of 10^{-1}. However, for smaller values of CEE ($\sigma_e^2 = 0.001$), the gain is 5 dB for an outage of 10^{-3}. Thus, the outage probability is more limited by CEE than SIC error, as high CEE shows degradation in outage probability with the same value of β.

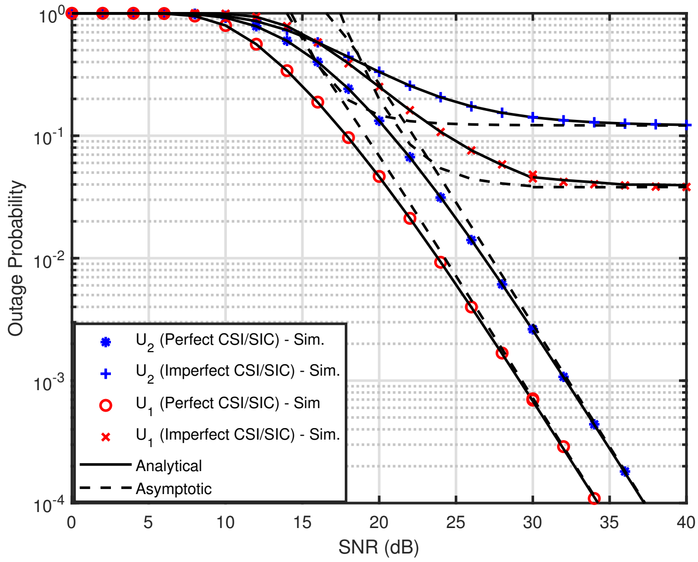

Figure 4.2: Outage probability of U_1 and U_2 with respect to transmit SNR ($a_2 = 0.7$, $\alpha = 0.35$).

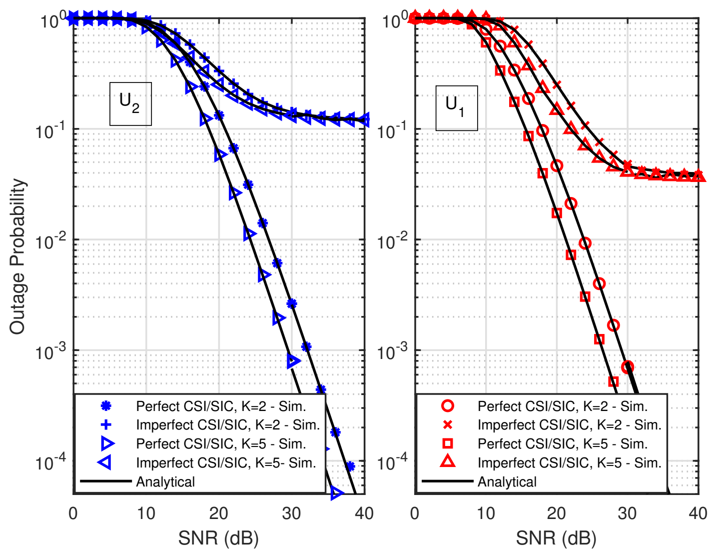

Figure 4.3: Outage probability of U_1 and U_2 with respect to transmit SNR for different values of K ($a_2 = 0.7$, $\alpha = 0.35$).

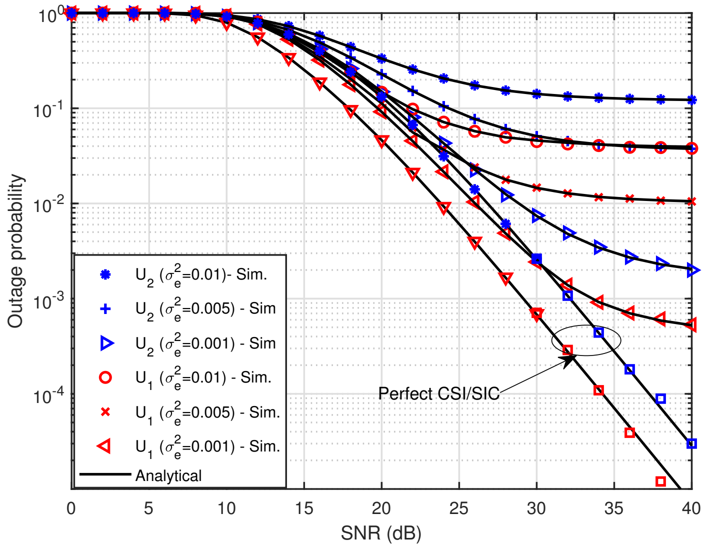

Figure 4.4: Outage probability of U_1 and U_2 under imperfect CSI/SIC with respect to transmit SNR for different value of σ_e^2 ($a_2 = 0.7$, $\alpha = 0.35$).

Impact of α

Figure 4.5 and Figure 4.6 illustrate the impact of α, the fraction of EH time, on the outage probability of U_1 and U_2. In the given scenario, the α is ranged between 0.1 and 0.7, whereas the ρ and σ_e^2 are fixed at 20 dB and 0.01, respectively. In Figure 4.5, the system's performance comparison under perfect CSI/SIC and imperfect CSI/SIC are shown. With the increase in α, the EH time increases, thus reducing the information processing time and hence outage probability of users increases for the entire time duration. The plot shows that the optimum value of α, which minimizes the outage probability, lies in the range of 0.2 to 0.3 for both perfect and imperfect CSI/SIC. Further, it is observed that at a high value of α, i.e., above 0.45, the outage probability of users becomes one. With the increase in the α, the threshold SNR, i.e., γ_{th1} and γ_{th2}, also increases to maintain the constant target data rates r_1 and r_2, respectively. Thus, the outage probability criteria $\gamma_{th2} < \frac{a_2}{a_1}$ and $\gamma_{th1} < \frac{a_1}{\beta a_2}$ does not satisfied and makes the outage probability $P_{out,1} = P_{out,2} = 1$. In Figure 4.6, the impact of a_1 and β on the outage probability of users under imperfect CSI/SIC is analyzed. In the case of U_2, it is observed that the outage probability with $a_1 = 0.1$ shows significant improvement over $a_1 = 0.3$ since more power is allocated to the symbol intended for U_2. However, in U_1, $P_{out,1}$ tends to unity due to failure of outage criteria $\gamma_{th1} < \frac{a_1}{\beta a_2}$ and $\gamma_{th2} < \frac{a_2}{a_1}$. Considering the high residual

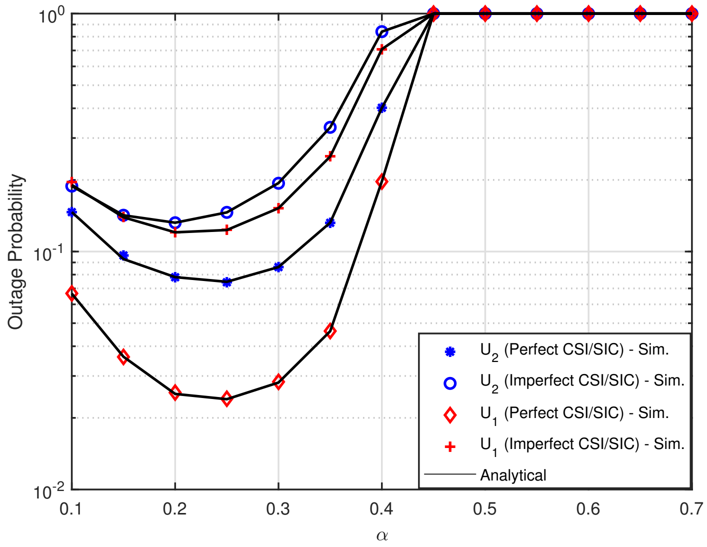

Figure 4.5: Outage probability of U_1 and U_2 w.r.t. α (K=2, $\rho = 20$ dB, $a_2 = 0.7$)

interference due to imperfect SIC, i.e., $\beta = 0.16$ and $\beta = 0.1$, the outage criteria are not satisfied and lead to a constant noise error floor. With a further decrease in residual interference i.e. $\beta = 0.01$, the outage probability of U_1 reduces. Hence, the selection of a_1 and β plays a crucial role in the outage performance of U_1.

Analysis of system throughput

Figure 4.7 shows the system throughput under optimized and non-optimized, i.e., (arbitrary) $\alpha = 0.3$ value. It is observed that the system throughput of the optimized NOMA scheme under both perfect and imperfect SIC/CSI is enhanced compared to the non-optimized value. It is observed that at the system throughput of 0.3 bps/Hz, the optimized value provides an SNR gain of 3 dB over the non-optimized fixed value.

Analysis of ergodic rate of U_1 and U_2

Impact imperfect CSI/SIC

In Figure 4.8, both users' ergodic rates under perfect CSI/SIC and imperfect CSI/SIC are plotted against SNR. It is observed from the figure that the ergodic rate of U_1 under perfect CSI/SIC outperforms the ergodic rate of all other cases. The ergodic

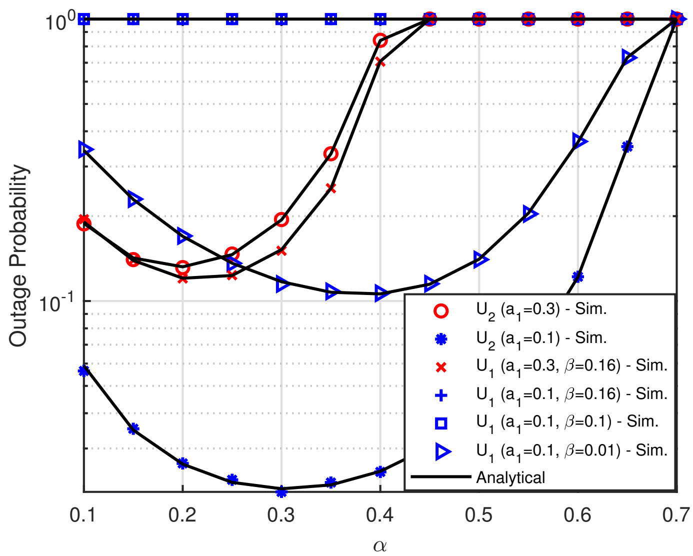

Figure 4.6: Outage probability of U_1 and U_2 under imperfect CSI/SIC w.r.t. α (K=2, $\rho = 20$ dB, $\sigma_e^2 = 0.01$)

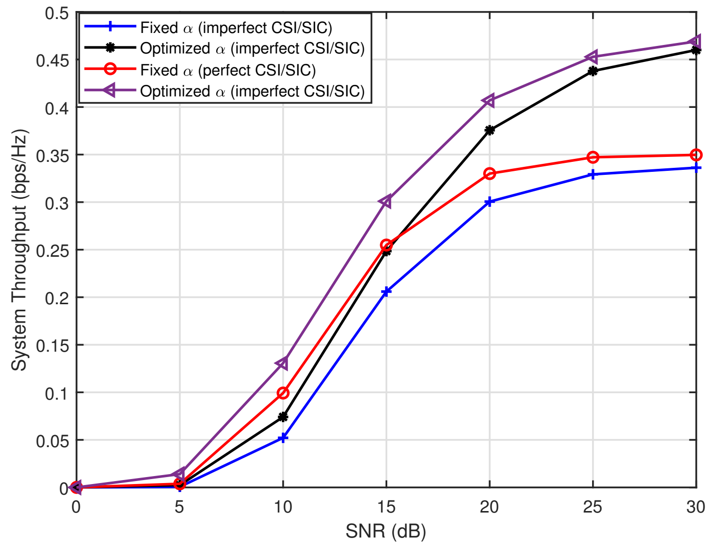

Figure 4.7: System throughput w.r.t. transmit SNR, comparison study of optimized and non-optimized fraction of EH time (K=2, $a_1 = 0.3$)

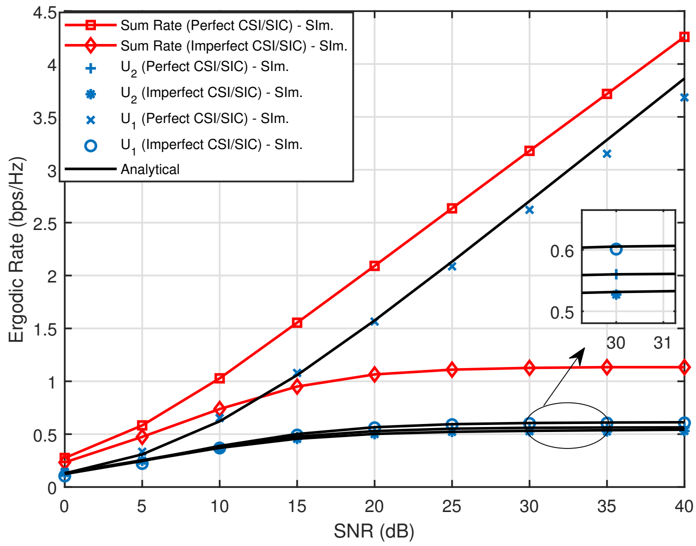

Figure 4.8: Ergodic rate of U_1 and U_2 w.r.t. transmit SNR (K=2, $a_1 = 0.3$)

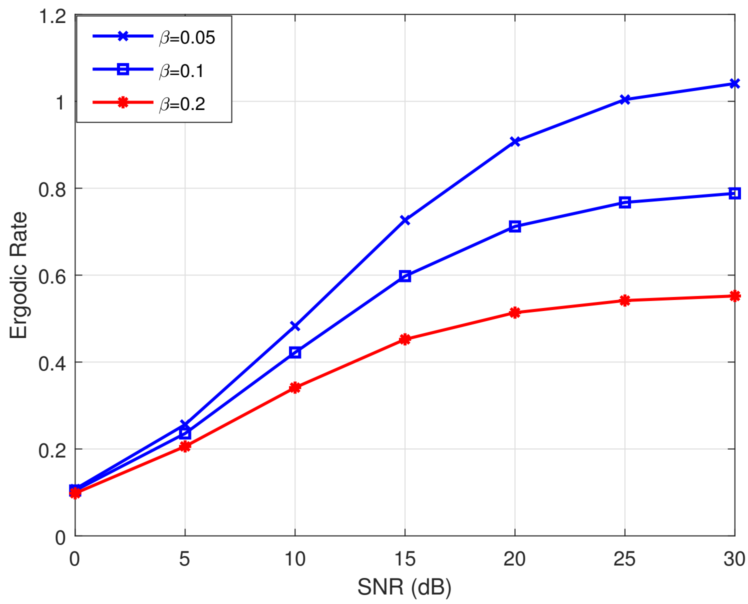

Figure 4.9: Ergodic rate of U_1 w.r.t. transmit SNR (K=2, $a_1 = 0.3$)

rate of U_1 under perfect CSI/SIC increases linearly with the SNR, whereas in case of U_2, the ergodic rate saturate at a high SNR region. The ergodic rate of 0.5 bps/Hz the U_1 provides an SNR gain of 7 dB over U_2 with perfect CSI/SIC. With the increase in SNR, the interference generated by the symbol of U_1 increases and leads to saturation in the ergodic rate plot. It is also observed that both users under imperfect CSI/SIC show a marginal increasing trend at low SNR region and saturates at high SNR region. This is due to the increase in SNR, the interference due to imperfect CSI/SIC increases, and the ergodic rate reduces effectively. Further, the NOMA system's sum rate (i.e., $r_1 + r_2$) is also presented under perfect CSI/SIC and imperfect CSI/SIC. For the ergodic rate of 1 bps/Hz, the perfect CSI/SIC case provides an SNR gain of 10dB over imperfect CSI/SIC. It is observed that at high SNR values, there is a marginal gap between the analytical and simulated curve for U_1, which is because of the approximation used in the analytical expression.

Impact of β

Figure 4.9 illustrates the impact of β, on the ergodic rate of U_1 under imperfect CSI/SIC. It is observed from the figure as the β increases, the interference due to the imperfect SIC increases; thus, the ergodic rate of U_1 decreases. It is observed that at the ergodic rate of 0.4 bps/Hz, the $\beta = 0.05$ provides an SNR gain of 5 dB over $\beta = 0.2$.

4.8 Summary

In this chapter, the analysis of a downlink multiple EH relay-based NOMA system over Nakagami$-m$ fading is performed. The practical assumption of imperfect SIC and imperfect CSI were taken into consideration for investigation. The closed-form expressions for the outage probability, asymptotic outage probability, and ergodic rate of the users under imperfect CSI/SIC are obtained. The analytical results showed that the system under imperfect CSI/SIC provides massive performance degradation compared to the perfect CSI/SIC NOMA system. It is observed that the users' performance improved with increasing the total number of active relay nodes in the system. The significance of channel estimation error over the performance of users is analyzed. The impact of the power allocation coefficient and a fraction of block time on user performance is also analyzed. Further, the impact of SIC error over the performance of U_1 is analyzed. It is also observed that there is an optimum value of α for users' minimum outage probability. To further make the relay node self-sustainable, in the next chapter, a backscatter-based NOMA system is analyzed.

Chapter 5

Performance Analysis of Backscatter Cooperative NOMA System

In the previous chapter, a cooperative NOMA system with an EH relay node was considered to enhance coverage and energy efficiency. The system performance was analyzed under the assumption of linear EH; however, in practice, the EH processes are inherently nonlinear and subject to significant inefficiencies, which can degrade the overall performance of the NOMA system. To address these challenges, BC technology emerges as a viable solution for achieving self-sustainability in low-power wireless networks. This approach not only aligns with the constraints of energy-limited scenarios but also enhances spectral efficiency, making it an effective strategy for next-generation NOMA systems.

In this chapter, a NOMA-based cooperative transmission system that utilizes a hybrid backscatter relay is considered. The hybrid backscatter relay consists of passive information transmission via backscatter, EH, and active information reception. novel and simple hybrid protocol is presented, where the relay operates in EH mode and active mode in the first phase, while in the second phase, it operates in passive mode. The chapter investigates the outage probability of the backscatter NOMA systems, considering realistic assumptions of nonlinear EH, channel estimation errors, and residual hardware impairments. Moreover, to gain deeper insights into the considered system, asymptotic outage probability, system throughput, and energy efficiency are derived.

5.1 Introduction

Along with EH, BC is also an emerging technique that has the potential to address the energy requirement of wireless networks. In EH, the node utilizes the harvested energy from the received RF signal for active transmission, whereas BC transmits the information by modulating it on the incident RF signal and reflects it toward the receiver. Thus, BC does not require any active components, e.g., oscillators, analog-to-digital/digital-to-analog converters, and others [107]. In a practical system, nonlinear EH circuits result in nonlinear wireless power transfer. Hence, the harvested energy is insufficient for information transmission, leading to performance degradation. Recently, to enhance the system's performance, a hybrid backscatter has been proposed by combining both BC and EH [108, 109]. In the hybrid mode, the node can operate in either passive mode, active mode or EH mode. In [108], cooperative communication with hybrid BC is considered, where the hybrid relay node switches its operating mode. In [109], hybrid BC is considered with a battery that stores the harvested energy and switches the operating mode according to the CSI.

The integration of cooperative communication with NOMA has garnered considerable attention due to its ability to expand coverage and enhance spectral efficiency [89, 110]. In particular, coordinated direct and relay transmission (CDRT) is one of the promising approach [111]. In [111], the performance of the CDRT-NOMA system is analyzed where an EH relay is deployed to assist the far user. In [112], authors considered an EH-based IoT device to assist the far user and the performance is analyzed in terms of outage probability and system throughput. In [111, 112], the authors considered a pure EH-based relay node, where the harvested energy is utilized for the information transmission and the power utilized by the relay circuit has not been considered for the analysis. In [107, 113–115], the authors analysed the performance of the NOMA system considering a cooperative backscatter relaying. In [114], authors considered a backscatter-based cooperative communication and showed that backscatter-based cooperative NOMA enhances the outage and rate performance compared to a non-cooperative NOMA system. In [107], authors considered a backscatter-based relaying, where a dedicated relay assists the NOMA users, and performance is analyzed in terms of error rate. The authors in [115] examined a backscatter-based NOMA system and demonstrated its performance gain compared to an OMA. However, their study was limited to ideal hardware with a linear EH model.

In this chapter, a novel and simple hybrid backscatter relay-based CDRT-NOMA system is proposed. In the first phase, the relay acts as an active device and performs EH and information reception. In the second phase, the relay acts as a passive node and backscatters the weak user's symbol by considering the source signal as an ambient signal. The harvested energy is only used to energize and operate the embedded circuit. In the proposed hybrid BC, the switching of mode is fixed rather than dependent on CSI, which reduces the system complexity. Further, in practical communications, all RF front-ends are susceptible to different types of HIs. Although these impairments can usually be mitigated through compensation techniques, some RHIs may still exist [116]. Thus, the performance of the considered system is analyzed by deriving closed-form outage probability expressions for both users, assuming practical imperfect cases, i.e. non-linear EH, RHIs, and CEE. The overall summary of contributions and novelty are as follows:

- For the first time in a hybrid backscatter-based CDRT NOMA system, the practical case of imperfect CSI and hardware impairment at receiver nodes is considered, and its impact on the system is analyzed. The proposed system features a hybrid relay that utilizes EH for its circuit operation and the backscatter principle for information transmission.

- The system performance is analyzed in terms of outage probability by deriving its closed-from expression from the novel E2E SNR of the considered system for both users for the imperfect case.

- The system performance is analyzed at high SNR by deriving the expression of asymptotic outage probability, and useful insights were drawn. The obtained results indicate that there are error floors for the outage probability due to the imperfect CSI and hardware impairment.

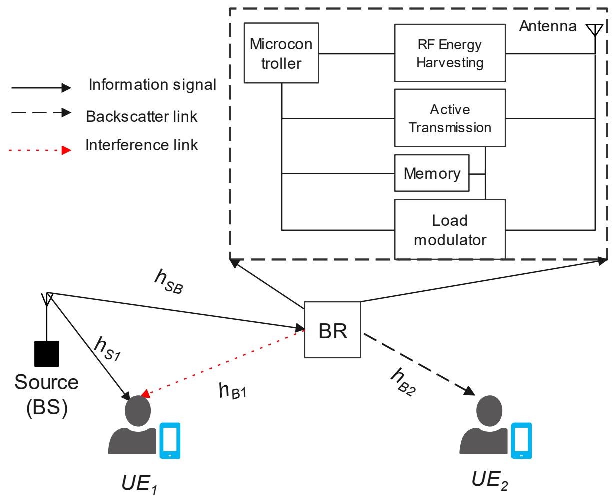

Figure 5.1: Hybrid backscatter-based CDRT NOMA.

- Extensive evaluations of the impact of imperfect CSI and hardware impairments on the outage performance of the users are presented. Furthermore, results for the system throughput and energy efficiency are also presented.
- The performance gain of the considered backscatter-based CDRT NOMA system has been compared against that of EH-based CDRT NOMA system and the conventional OMA based CDRT system. Analytical results are corroborated by extensive Monte-Carlo simulation.
- Further, it is demonstrated that there exists a unique value of the power splitting coefficient parameter that minimizes the outage probability.

5.2 System Model

In this work, a downlink hybrid backscatter-based CDRT NOMA system is considered, where the BS communicates directly with the strong user UE_1 and indirectly with the weak user UE_2 through the assistance of hybrid backscatter relay (BR) as shown in Figure 5.1. All the nodes work in half-duplex mode and are equipped with one antenna. As in [117], it is assumed that the direct link between the BS and UE_2 is absent due to severe path loss, which forces the communication only through the relay nodes. It is assumed that the channel links between the nodes are frequency flat block fading, where Rayleigh fading is assumed for each link. Under a practical scenario, the perfect CSI is unavailable, which leads to CEE. According to linear

MMSE estimation, the channel can be modelled as

$$h_{ij} = \hat{h}_{ij} + \epsilon_{ij}, \tag{5.1}$$

where $i = \{S, B\}$ and $j = \{B, 1, 2\}$, where the subscript $S, B, 1$ and 2 represents BS, BR, UE_1, and UE_2, respectively. The ϵ_{ij} is the CEE, where $\epsilon_{ij} \sim \mathcal{CN}(0, \sigma_{ij}^2)$ [79]. The h_{ij} is the actual channel, and $\hat{h}_{ij}$ is the estimated channel with variance given as $\bar{\lambda}_{ij} = \lambda_{ij} - \sigma_{ij}^2$.

The communication between BS, and UE_1 and UE_2 takes place in two phases (τ_1 and τ_2). In the first phase (τ_1), the BS broadcasts superimposed NOMA signal intended for UE_1 and UE_2. The superposition signal is given as

$$s^1 = \sqrt{P_s a_1} s_1^1 + \sqrt{P_s a_2} s_2^1, \tag{5.2}$$

where P_s is the total transmit power at BS, a_1 and a_2 are the NOMA power allocation coefficients of UE_1 and UE_2, respectively such that $a_1 < a_2$[1] and $a_1 + a_2 = 1$. Transmitted signal of UE_1 and UE_2 are denoted by s_1^1 and s_2^1, respectively in the first phase with $\mathbb{E}\{|s_1^1|^2\} = \mathbb{E}\{|s_2^1|^2\} = 1$. Meanwhile, the hybrid BR will work in active mode, where the BR dynamically splits the received signal into two streams with power splitting coefficient β and $(1-\beta)$ for EH and information processing, respectively. The harvested energy is utilized to energize the circuit. To characterize the harvested power, a practical nonlinear EH model is considered at the relay node given as [118]

$$E_H = \frac{P_{max} \left(1 - \exp\left(-\tau P_{in} + \tau P_{sen}\right)\right)}{1 + \exp\left(-\tau P_{in} + \mu\right)} \tau_1, \tag{5.3}$$

where $P_{in} = P_s \beta |\hat{h}_{SB}|^2$ is input power at BR, maximum harvested power is P_{max}, P_{sen} is the sensitivity threshold, the parameters τ and μ are fixed determined by resistance, capacitor and diode, and τ_1 is the time phase of the transmission. The received signal at i ($i \in \{B, 1\}$) in the first phase is given as

$$y_i^1 = \left(\hat{h}_{Si} + \epsilon_{Si}\right) \left(s^1 + \eta_{Si}\right) + n_i, \tag{5.4}$$

[1]More power is allocated to the weaker user to improve user(s) fairness.

where $n_i \sim \mathcal{CN}(0, N_0)$ is the complex AWGN, the RHI is modelled by a Gaussian random variable $\eta_{Si} \sim CN(0, \kappa_{Si}^2 P_s)$, where κ_{Si} denotes the level of RHI at the transceivers [116].

According to the NOMA protocol, UE_1 decodes the signal s_1^1 with the aid of SIC, and BR decodes signal s_2^1 considering s_1^1 as interference. The received SINR at l ($l \in \{1, B\}$) to decode s_2^1 is given as

$$\gamma_l^{s_2^1} = \frac{P_l a_2 |\hat{h}_{Sl}|^2}{P_l a_1 |\hat{h}_{Sl}|^2 + P_l \sigma_{Sl}^2 (1 + \kappa_{Sl}^2) + P_l |\hat{h}_{Sl}|^2 \kappa_{Sl}^2 + N_0}, \tag{5.5}$$

where $P_1 = P_s$ and $P_B = P_s(1 - \beta)$. The received SINR at UE_1 to decode s_1^1 is given as

$$\gamma_1^{s_1^1} = \frac{P_s a_1 |\hat{h}_{S1}|^2}{P_s \sigma_{S1}^2 (1 + \kappa_{S1}^2) + P_s |\hat{h}_{S1}|^2 \kappa_{S1}^2 + N_0}. \tag{5.6}$$

In the second phase, the BS transmits a new signal intended for the UE_1 (s_1^2). Meanwhile, BR acts as a passive node and backscatters the received signal from the BS by modulating s_2^1. The received signal at UE_1 in the second phase is given as

$$y_1^2 = h_{S1} \left(\sqrt{P_s} s_1^2 + \eta_{S1} \right) + \sqrt{P_s \eta \delta} \hat{h}_{SB} \hat{h}_{B1} s_1^2 s_2^1 + n_1, \tag{5.7}$$

where the term $\sqrt{P_s \eta \delta} \hat{h}_{SB} \hat{h}_{B1} s_1^2 s_2^1$ is the interference from the BR, which can be estimated and eliminated using s_2^1 obtained during the SIC process in the first phase. The δ represents the residual interference cancellation coefficient of the BR signal at UE_1. The backscatter efficiency is given by η, which denotes the signal being effectively reflected by the BR. The UE_1 directly decode its desired signal from the received signal.

$$\gamma_1^{s_1^2} = \frac{P_s |\hat{h}_{S1}|^2}{P_s \eta \delta |\hat{h}_{SB}|^2 |\hat{h}_{B1}|^2 + P_s M_0 + P_s |\hat{h}_{S1}|^2 \kappa_{S1}^2 + N_0}, \tag{5.8}$$

where $M_0 = \sigma_{S1}^2 (1 + \kappa_{S1}^2)$. The received signal at UE_2 in the second phase is given as

$$y_2^2 = P_s \eta h_{SB} h_{B2} \left(s_1^2 s_2^1 + \eta_{S2} \right) + n_2. \tag{5.9}$$

The corresponding SINR in the second phase is given as

$$\gamma_2^{s_2^2} = \frac{P_s \eta |\hat{h}_{SB}|^2 |\hat{h}_{B2}|^2}{P_s \left[\eta |\hat{h}_{SB}|^2 |\hat{h}_{B2}|^2 \kappa_{S2} + |\hat{h}_{SB}|^2 M_2 + |\hat{h}_{B2}|^2 C_2 + \psi \right] + N_0}, \tag{5.10}$$

where, $B_2 = \eta\,(1 + \kappa_{S2}^2)$, $\psi = B_2 \sigma_{SB}^2 \sigma_{B2}^2$, $M_2 = \sigma_{B2}^2 B_2$ and $C_2 = \sigma_{SB}^2 B_2$.

5.3 Performance Analysis

5.3.1 Outage probability analysis

Outage probability of UE_1

The UE_1 is in an outage when, in the first phase, UE_1 fails to detect the symbols s_1^1 and s_2^1. The UE_1 also fails to detect the symbols s_1^2 in the second phase. Thus, the outage probability of UE_1 in the first phase is defined as

$$\mathrm{P}_{UE_1}^1 = \Pr\left\{ \gamma_1^{s_2^1} \leq \gamma_{th,2}, \gamma_1^{s_1^1} \leq \gamma_{th,1} \right\}, \tag{5.11}$$

where $\gamma_{th,1} = 2^{R_1} - 1$ and $\gamma_{th,2} = 2^{R_2} - 1$ are predefined SINR threshold, where R_1 and R_2 are the desired target rate of UE_1 and UE_2, respectively. Closed-form expression of (5.13) is derived by substituting $\gamma_1^{s_2^1}$ and $\gamma_1^{s_1^1}$ in (5.11). After solving, the outage probability of UE_1 is given as

$$\begin{aligned} \mathrm{P}_{UE_1}^1 = \Pr\{& P_s a_2 |\hat{h}_{S1}|^2 \leq \gamma_{th,2}(P_s a_1 |\hat{h}_{S1}|^2 + P_s |h_{S1}|^2 \kappa_{S1}^2 + N_0 + P_s \sigma_{S1}^2 (1 + \kappa_{S1}^2)), \\ & P_s a_1 |\hat{h}_{S1} |P_s|^2 \leq \gamma_{th,1}(N_0 + P_s \sigma_{S1}^2 (1 + \kappa_{S1}^2) + P_s \hat{h}_{S1}|^2 \kappa_{S1}^2)\}. \end{aligned} \tag{5.12}$$

Given the assumption of Rayleigh fading, the channel gains $|h_{i,j}|^2$ are exponential functions. By utilizing the CDF, the closed-form expression of outage probability for UE_1 in the first phase under imperfect CSI with RHI is given as

$$\mathrm{P}_{UE_1}^1 = 1 - \exp^{\left(-\frac{1}{\bar{\lambda}_{S1}} \mathrm{Max}\left\{ \frac{A_1}{\rho A_2}, \frac{A_1 \gamma_{th,1}/\gamma_{th,2}}{\rho\left(a_1 - \kappa_{S1}^2 \gamma_{th,1}\right)} \right\} \right)}, \tag{5.13}$$

where $A_1 = (\kappa_{S1}^2 + 1)\,\rho\sigma_{S1}^2\gamma_{th,2} + \gamma_{th,2}$, $A_2 = (a_2 - a_1\gamma_{th,2} - \kappa_{S1}^2\gamma_{th,2})$, $\rho = P_s/N_0$. The outage probability of UE_1 in the second phase is defined as

$$\mathrm{P}_{UE_1}^2 = \Pr\left\{\gamma_1^{s_1^2} \leq \gamma_{th,1}\right\}. \tag{5.14}$$

Substituting $\gamma_1^{s_1^2}$ in (5.14), after further simplification, the following expression is obtained

$$\mathrm{P}_{UE_1}^2 = \Pr\left\{D_o|\hat{h}_{S1}|^2 \leq C_0|\hat{h}_{SB}|^2|\hat{h}_{B1}|^2 + B_0\right\}, \tag{5.15}$$

where $D_0 = (a_1 - \kappa_{S1}^2\gamma_{th,1})\,, C_0 = \eta\delta\gamma_{th,1}$ and $B_0 = \gamma_{th,1}\,(M_0 + 1/\rho)$. Further, utilizing CDF, the outage probability is given as

$$\begin{aligned}\mathrm{P}_{UE_1}^1 = 1 - &\int_{x=0}^{\infty}\int_{y=0}^{\infty}\frac{\exp\left(-\frac{B_0}{D_0\bar{\lambda}_{S1}}\right)}{\bar{\lambda}_{SB}\bar{\lambda}_{B1}}\exp\left(-\frac{xyC_0}{D_0\bar{\lambda}_{S1}}\right)\exp\left(-\frac{x}{\bar{\lambda}_{SB}}\right)\\ &\exp\left(-\frac{y}{\bar{\lambda}_{B1}}\right)dydx,\end{aligned} \tag{5.16}$$

The integral in (5.16) is solved by utilizing [54, eq. 3.352.4], and the closed-form expression is given in (5.17). The analytical expression of outage probability for UE_1 in the second phase under imperfect CSI with RHI is given as

$$\mathrm{P}_{UE_1}^2 = 1 - A_3\exp^{\left(-\frac{B_0}{\bar{\lambda}_{S1}D_0}\right)}\exp^{\left(\frac{A_3}{\bar{\lambda}_{SB}}\right)}\mathrm{E}_1\left(\frac{A_3}{\bar{\lambda}_{SB}}\right), \tag{5.17}$$

where $A_3 = \frac{\bar{\lambda}_{S1}D_0}{C_0\bar{\lambda}_{B1}}$.

Outage probability of UE_2

The outage event occurs at UE_2 when the harvested energy at BR falls below the minimum energy requirement by the BR circuit, BR fails to decode s_2^1, and UE_2 fails to decode s_2^1. Thus, the outage probability at UE_2 is given as

$$P_{UE_2} = 1 - \left[\Pr\left\{\gamma_{BR}^{s_2^1} \geq \gamma_{th,2}\right\}\left(1 - \Pr\left\{E_H < P_c\tau_1\right\}\Pr\left\{E_H \geq P_c\tau_1, \gamma_{UE_2}^{s_2^1} \leq \gamma_{th,2}\right\}\right)\right], \tag{5.18}$$

where P_c denotes the BR circuit power consumption. Let $\mathrm{P}_{UE_2} = 1-[I_1 \times (1 - I_2 \times I_3)]$, after substituting $\gamma_{BR}^{s_2^1}$ in I_1 and simplification, I_1 is given as

$$I_1 = \Pr\{P_s a_2(1-\beta)|\hat{h}_{SB}|^2 > \gamma_{th,2} P_s(1-\beta)(a_1|\hat{h}_{SB}|^2 + \kappa_{SB}^2|\hat{h}_{SB}|^2 + \sigma_{SB}^2(1+\kappa_{SB}^2)) + 1\}. \tag{5.19}$$

By using the CDF, the obtained I_1 is as follows

$$I_1 = \exp^{\left(-\frac{(1-\beta)C_1\rho\gamma_{th,2}+\gamma_{th,2}}{(1-\beta)\bar{\lambda}_{SB}\rho\left(a_2-a_1\gamma_{th,2}-\kappa_{SB}^2\gamma_{th,2}\right)}\right)}. \tag{5.20}$$

Further, by substituting E_H, I_2 can be written as

$$I_2 = \Pr\left\{P_{max}\left(1-e^{-\tau P_{in}+\tau P_{sen}}\right) < P_c(1+e^{-\tau P_{in}+\mu)}\right\}, \tag{5.21}$$

By using the CDF, the obtained I_2 is as follows

$$I_2 = 1 - \frac{1}{\bar{\lambda}_{SB}} \exp\left(-\frac{A}{\bar{\lambda}_{SB}}\right), \tag{5.22}$$

where $A = \frac{\ln\left(\frac{P_c\exp(\mu)+P_{max}\exp(-P_{sen}\tau)}{P_{max}-P_c}\right)}{\beta\rho\tau}$. Further, substituting E_H and $\gamma_{UE_2}^{s_2^1}$ in I_3, the following expression is obtained

$$I_3 = \Pr\left\{P_{max}\left(1-e^{-\tau P_{in}+\tau P_{sen}}\right) > P_c(1+e^{-\tau P_{in}+\mu}), P_s\eta|\hat{h}_{SB}|^2|\hat{h}_{B2}|^2 < \gamma_{th,2}P_s[\eta|\hat{h}_{SB}|^2|\hat{h}_{B2}|^2\kappa_{S2} + |\hat{h}_{SB}|^2 M_2 + |\hat{h}_{B2}|^2 C_2 + \psi] + 1\right\}, \tag{5.23}$$

Now, the I_3 is simplified as follow

$$I_3 = \int_{x=A}^{\infty} \left(1-\exp\left(-S1\right)\right) \frac{\exp\left(-\frac{x}{\bar{\lambda}_{SB}}\right)}{\bar{\lambda}_{SB}} dx,$$

where $S1 = \frac{xM_2\rho+\psi\rho+1}{\zeta_1 x - C_2\rho}$.

$$I_3 = \frac{1}{\bar{\lambda}_{SB}} \exp\left(-\frac{A}{\bar{\lambda}_{SB}}\right) - \int_{x=A}^{\infty} \frac{\exp\left(-S1-\frac{x}{\bar{\lambda}_{SB}}\right)}{\bar{\lambda}_{SB}} dx. \tag{5.24}$$

The integral above is challenging to solve. Therefore, GCQ is used. $\int_a^b f(y)dy \approx \frac{(b-a)\pi}{2V}\sum_{m=1}^{V}\sqrt{1-x_m^2}f(y_m)$, where $y_m = \frac{(b-a)x_m}{2} + \frac{b-a}{2}$, $x_m = \cos\left(\frac{(2m-1)\pi}{2V}\right)$ to obtained an approximation for the integral. After some simplification and substituting I_1, I_2 and I_3 in P_{UE_2}, the analytical expression of outage probability for UE_2 under imperfect CSI with RHI is given as

$$\mathrm{P}_{UE_2} \approx \exp^{\left(-\frac{(1-\beta)C_1\rho\gamma_{th,2}+\gamma_{th,2}}{(1-\beta)\bar{\lambda}_{SB}\rho A_2}\right)} \times \left(1 - \sum_{k=1}^{N_1}\sqrt{1-\phi_k^2}\exp^{\left(-\frac{\gamma_{th,2}(M_2 y+\psi+1/\rho)}{\zeta_1 y - C_2} - \frac{y}{\bar{\lambda}_{SB}}\right)} \frac{\pi(\delta_1 - A)}{2\bar{\lambda}_{SB}N_1}\right), \tag{5.25}$$

where $C_1 = \sigma_{SB}^2(1+\kappa_{SB})$, $\phi_k = \cos\left(\frac{(2k-1)\pi}{2N_1}\right)$, $\zeta_1 = \eta\left(1 - \gamma_{th,2}\kappa_{S2}^2\right)$ and $y = \frac{1}{2}\phi_k(\delta_1 - A) + \frac{A+\delta_1}{2}$.

5.3.2 Asymptotic outage probability

The asymptotic outage probability is analyzed to improve analytical tractability and gain valuable insights. At high SNR region, by considering the approximation, $\frac{1}{x} \approx 0$, as $x \to \infty$, The asymptotic outage probability of UE_1 in the first phase is given as

$$\mathrm{P}_{UE_1}^{1,A} = 1 - \exp^{\left(\frac{-1}{\bar{\lambda}_{S1}}\mathrm{Max}\left\{\frac{\left(\kappa_{S1}^2+1\right)\sigma_{S1}^2\gamma_{th,2}}{A_2}, \frac{\left(\kappa_{S1}^2+1\right)\sigma_{S1}^2\gamma_{th,1}}{\left(a_1 - \kappa_{S1}^2\gamma_{th,1}\right)}\right\}\right)}. \tag{5.26}$$

The asymptotic outage probability of UE_1 in the second phase is given as

$$\mathrm{P}_{UE_1}^{2,A} = 1 - A_3\mathrm{E}_1\left(\frac{A_3}{\bar{\lambda}_{SB}}\right)\exp^{-\frac{\gamma_{th,1}M_0}{\bar{\lambda}_{S1}D_0} + \frac{A_3}{\bar{\lambda}_{SB}}}. \tag{5.27}$$

The analytical expression of asymptotic outage probability for UE_2 under imperfect CSI with RHI is given as

$$\mathrm{P}_{UE_2}^{A} \approx \exp^{\left(-\frac{(1-\beta)C_1\gamma_{th,2}}{(1-\beta)\bar{\lambda}_{SB}A_2}\right)} \times \left(1 - \sum_{k=1}^{N_1}\sqrt{1-\phi_k^2}\frac{\pi\delta_1}{2\bar{\lambda}_{SB}N_1}\exp^{\left(-\frac{\gamma_{th,2}(M_2 y+\psi)}{\zeta_1 y - C_2} - \frac{y}{\bar{\lambda}_{SB}}\right)}\right).$$

5.3.3 System throughput

The system throughput in a delay-limited transmission mode based on outage probability or a fixed transmission rate is defined as

$$R_{sys} = \frac{(1 - P^1_{UE_1})}{2} R_1 + \frac{(1 - P^2_{UE_1})}{2} R_1 + \frac{(1 - P_{UE_2})}{2} R_2. \tag{5.28}$$

5.3.4 Energy efficiency

Energy efficiency serves as a crucial performance metric that facilitates high-speed data rates while optimizing power consumption to support sustainable technologies. In the context of the given system, energy efficiency is defined as the ratio of the total transferred data to the total consumed power. The energy efficiency of the considered system is given as

$$EE_s = \frac{R_{sys}}{P_s + P_c}. \tag{5.29}$$

5.4 Numerical and Simulation Results

This section presents results for evaluating the proposed system's performance. Unless stated otherwise, the system parameters used in the evaluation are as follows. $P_c = 8.9 \times 10^{-3}$, $\tau = 274$, $\mu = 0.29$, $P_{max} = 0.001$,[118] target rate $R_1 = 1$ bpcu, $R_2 = 0.5$ bpcu, $a_1 = 0.2$, λ_{B1}, $\lambda_{S1} = \lambda_{SB} = \lambda_{B2} = 1$, $\sigma_e = \sigma^2_{S1} = \sigma^2_{SB} = \sigma^2_{B2} = 0.01$, $\kappa = \kappa_{S1} = \kappa_{S2} = \kappa_{SB} = 0.1$ [119]. The results are obtained through extensive simulations using Matlab with 10^5 Monte Carlo iterations. In the figures, (Sim.) denotes the Matlab simulation results.

In Figure 5.2, the outage probability experienced by UE_2 of the proposed backscatter-based CDRT-NOMA system is compared with the existing EH-based NOMA system [111]. Results show a significant improvement of the proposed backscatter-based model over the EH-based model. It is observed that, at an outage of 10^{-2}, the proposed system provides an SNR gain of 4 dB over an EH-based CDRT-NOMA with linear EH. Further, compared to the nonlinear EH case, the proposed model significantly improves performance due to the insufficient harvested power at the relay node for the IT due to the nonlinear EH. Further, Figure 5.2 shows the comparison of the proposed system with the benchmark OMA system. It is observed from the Figure 5.2 that the backscatter-based NOMA system outperforms the OMA system. At an outage of 2×10^{-2}, the backscatter-based NOMA system shows an SNR gain of 2 dB over the OMA system for UE_2. Further, at outage of 4×10^{-2}, the backscatter-based NOMA system shows a considerable SNR gain of 4 dB over the OMA system for UE_1.

Figure 5.3 compares the outage probability experienced by the two users, UE_1 and UE_2, with different CEE (σ_e) and RHI level (κ). The results indicate that there is a significant impact on the outage probability of both users due to the imperfections in CSI with RHI. For instance, at an outage probability of 5×10^{-2}, UE_1 experiences a 10 dB SNR gain in the first phase with perfect CSI without RHI ($\sigma_e = 0, \kappa = 0$) over the imperfect CSI with RHI ($\sigma_e = 0.01, \kappa = 0.1$), and the UE_2 with perfect CSI without RHI provides an SNR gain of 2.5 dB over imperfect CSI with RHI ($\sigma_e = 0.01, \kappa = 0.1$). Furthermore, it is observed that the performance degradation of the imperfect CSI case worsens as the SNR increases due to an increase in CEE and RHI, which limits the outage probability from decreasing further and ultimately reaching a floor. Furthermore, the asymptotic outage probability of users is plotted, and it is observed that the asymptotic outage probability perfectly matches the outage probability at a high SNR region. It is also observed that the outage probability approaches fixed constant floors due to the CEE in the high SNR region. Thus, the diversity order of the considered system is zero.

In Figure 5.4, depict the outage probability of UE_2 against the transmit SNR for various values of maximum harvested energy (P_{max}) and power splitting coefficient (β). It is observed that for the low value of $P_{max} = 10^{-4}$, the UE_2 is in an outage for the entire SNR range. Since at a low value of P_{max}, the harvested energy at BR is insufficient to energize the BR circuit to operate, leading the outage probability to unity. However, the power consumption of the BR circuit is usually very low [108], resulting in the circuit working with small harvested energy. Thus, with $P_{max} = 10^{-3}$, the outage probability shows a significant improvement in the outage probability as the BR successfully backscatter the information. Further, results show the improvement in outage probability with $\beta = 0.3$ over $\beta = 0.5$, at an outage

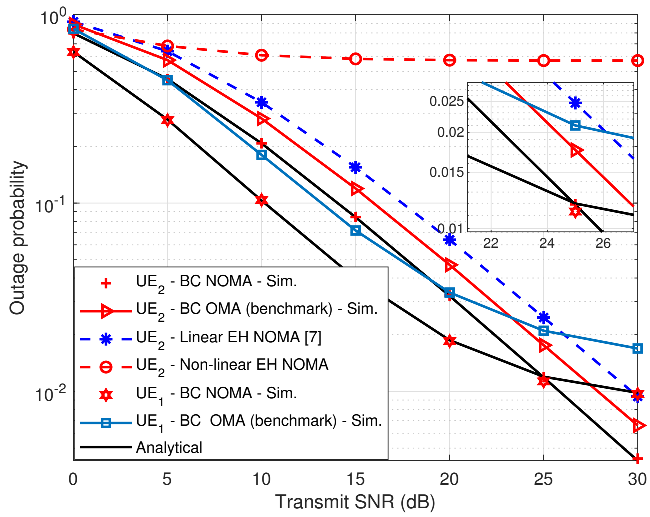

Figure 5.2: Outage probability of UE_2 w. r. t. SNR

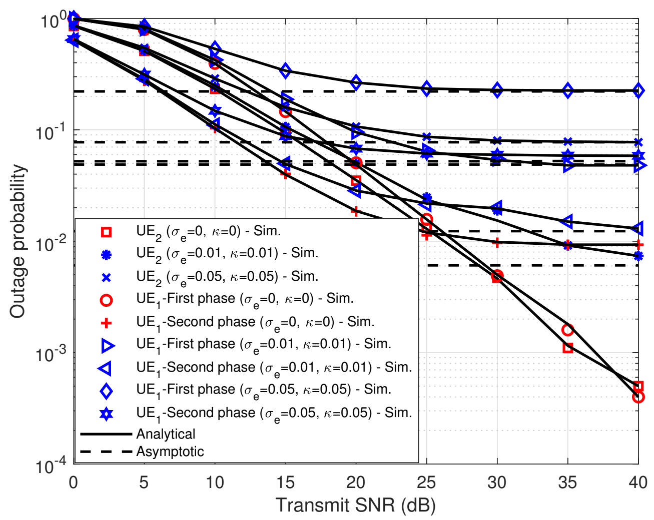

Figure 5.3: Outage probability of UE_2 w.r.t. SNR

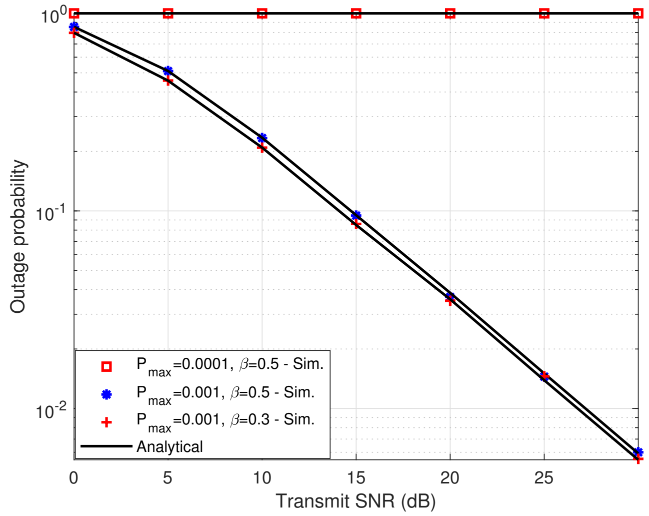

Figure 5.4: Outage probability of UE_2 w.r.t. SNR with different β and P_{max}

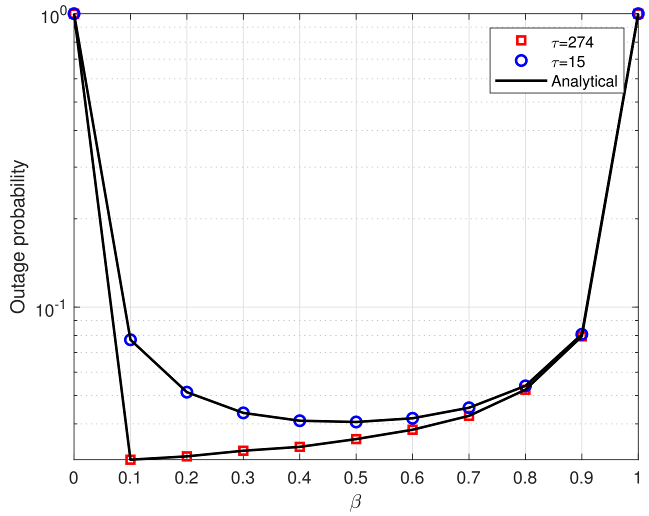

Figure 5.5: Outage probability of UE_2 w.r.t. β.

probability of 10^{-1}, UE_2 with $\beta = 0.3$ provides an SNR gain of 1 dB over $\beta = 0.5$. With the decrease in the β, a higher fraction of power is given for information decoding at BR, resulting in improved performance.

In Figure 5.5, the variation of outage probability of UE_2 w.r.t. β for different EH parameter τ is shown. In this scenario, β is taken between 0 and 1, while ρ is fixed at 20 dB. As β increases, the EH time increases, resulting in a reduction in backscattering time and, consequently, a degradation in OP. It is observed that at $\tau = 15$, the optimal value of β ranges between 0.4 and 0.6. It is also noted that when $\beta = 0$ and $\beta = 1$, the outage probability becomes one, as with $\beta = 1$, the BR will not be able to backscatter the information to UE_2, leading to the outage

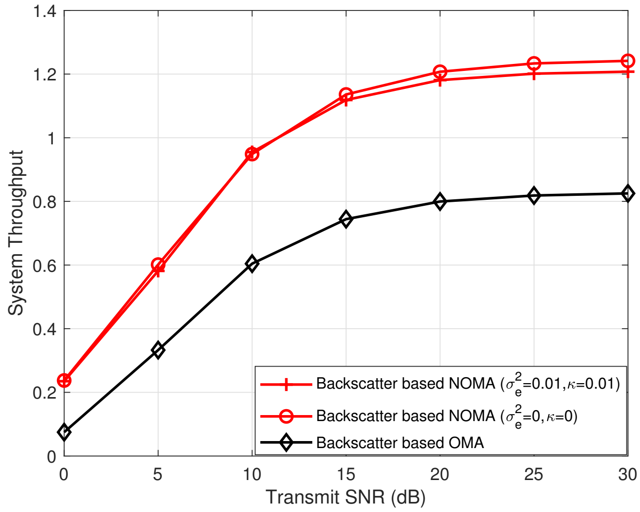

Figure 5.6: System throughput w.r.t. SNR.

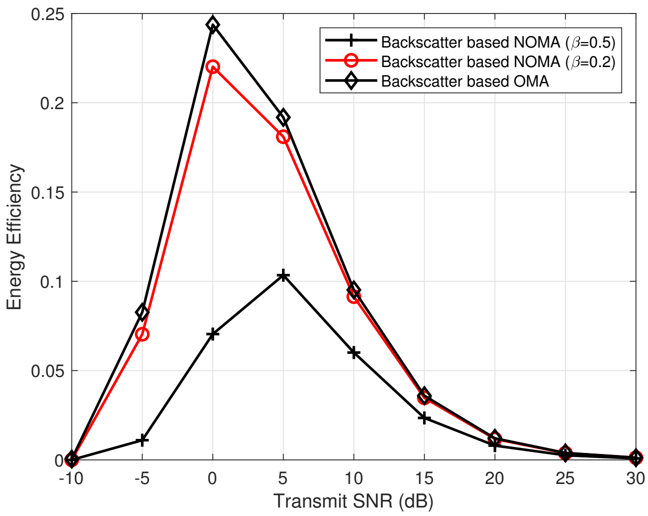

Figure 5.7: Energy Efficiency w.r.t. SNR.

probability reaching unity.

In Figure 5.6, the system throughput is plotted w.r.t. the SNR. It is observed that as the SNR increases, the throughput increases and attains a constant saturated value. The saturated value is the maximum achievable throughput for a specific threshold data rate. Further, it is also observed that the proposed NOMA system outperforms the OMA system. At a throughput of 0.6 bps/Hz, the NOMA system shows an SNR gain of 5 dB over an OMA system. Figure 5.7, illustrates the relationship between energy efficiency and SNR. It is evident that energy efficiency increases as SNR rises and reaches its maximum value at a specific SNR corresponding to a particular β. Notably, a specific SNR value exists at which maximum energy efficiency is achieved. Additionally, the energy efficiency decreases in the high SNR regime due to higher consumed energy compared to the achievable throughput. Furthermore, the proposed system model exhibits a substantial improvement over the OMA system.

5.5 Summary

This chapter primarily revolves around the analysis of a hybrid backscatter-based CDRT-NOMA. The investigation takes into account practical scenarios, such as non-linear EH, imperfect CSI, and RHI. Closed-form expressions of outage probability for both users' imperfect cases are derived. The asymptotic OP, system throughput and energy efficiency of the considered system are derived. The results demonstrate that the CDRT-NOMA system with a self-sustainable backscatter relay node outperforms EH-based systems, providing a significant improvement in performance. The study highlights the potential of backscatter-based systems in enabling self-sustainable wireless communication networks.

The rapid growth of IoT devices demands more efficient use of the wireless spectrum to support the vast amounts of data transmission and connectivity required. SR is crucial in this context, as it enables cooperative communication between devices, improving spectral efficiency and reducing energy consumption in IoT networks. Thus, in the next chapter, a symbiotic communication approach for IoT devices is considered for a backscatter NOMA system.

Chapter 6

Performance of Backscatter-NOMA Systems: Symbiotic Communication for IoT Devices

In the previous chapter, the performance of a backscatter-based NOMA system was analyzed. Analytical expressions for outage probability, asymptotic outage probability, system throughput, and energy efficiency were derived, focusing on a cooperative NOMA system utilizing BC to enhance performance. Further, the exponential growth of IoT devices demands a communication paradigm that can efficiently manage massive connectivity, minimize energy consumption, and utilize spectrum resources effectively. SR addresses these challenges by enabling IoT devices to communicate through backscattering ambient signals, significantly reducing power requirements and extending device lifetimes. Additionally, SR facilitates dynamic spectrum sharing between the primary network and IoT network, thereby improving spectral efficiency and supporting seamless coexistence in ultra-dense networks.

In this chapter, instead of using a dedicated relay to enhance NOMA system performance, an SR system tailored for IoT devices is proposed. This innovative framework integrates backscatter-based IoT devices into the NOMA network, employing an SR approach to serve IoT receivers while simultaneously boosting NOMA user performance cooperatively. The chapter provides an in-depth analysis of outage probabilities for both NOMA and IoT networks, leveraging existing infrastructure to improve performance and optimize resource utilization, thereby reducing the need for additional dedicated relays.

6.1 Introduction

The SR technique has emerged as a solution for battery-less IoT devices, employing BC [17, 18]. SR establishes a cooperative relationship between the two networks, namely the primary and the IoT networks, enabling them to share resources and exchange information within the same radio spectrum. Thus, in the SR system, the primary transmitter or the primary BS plays a dual role, supporting transmission from the primary and the IoT devices. IoT devices, also referred to as backscatter devices, employ load modulation techniques to convey their messages by riding on the RF signal emitted by the BS, ensuring efficient data transfer to the designated receivers. The SR is divided into parasitic SR and commensal SR, based on the symbol rate of the IoT device compared to the transmission rate of the BS [17]. In parasitic SR, the symbol rates of both BS and IoT device transmission are equal, whereas, in commensal SR, the symbol rate of IoT transmission is much lower as compared to the BS transmission, resulting in the IoT transmission as an additional multipath component at the primary receivers [120]. In [113], the authors considered a symbiotic system of cellular and IoT networks, and the performance of the SR-NOMA system under a parasitic setup was analyzed by deriving the closed-form expression of the outage probability and ergodic rate. In [121], the authors considered the system model as in [113] and derived the coexistence outage probability for the symbiotic system. In [122], the author considered a downlink NOMA SR system consisting of one backscatter device and one receiver. The outage probability expressions were derived to analyze the system performance under the Nakagami-m fading channel. In [123], the author considered a primary NOMA network with a backscatter device and optimized the system performance and power efficiency. In [124], a BS serves two NOMA primary users and a tag in a commensal SR setup. The power allocation factor and the tag's reflection coefficient were jointly optimized to maximise the system rate under imperfect SIC. However, the majority of these works primarily emphasize parasitic SR communication [113, 121–123, 125]. Moreover, BC operates on the same spectrum as the RF source, aligning with the vision for green IoT technology. The BC may suffer from severe direct-link interference (DLI) due to its spectrum-sharing nature [126]. Different schemes have been proposed to mitigate the DLI issue and improve the system reliability over DLI. In [127], the authors proposed a DLI cancellation method for BC over ambient digital video broadcasting signals and demonstrated its effectiveness in suppressing the DLI. Similarly, in [17, 120], the authors applied the cancellation methods to suppress the DLI and analyzed the system considering perfect DLI cancellation at the receiver.

Contribution

Drawing inspiration from incorporating BC into NOMA, which has demonstrated significant enhancements in both spectral and energy efficiency, furthering the goal of establishing a self-sustainable wireless network. Remarkably, to the best of the author's knowledge, no existing literature analysed the integration of commensal SR communication within the NOMA system. The existing literature appears to lack a comprehensive analysis of performance evaluation metrics, encompassing critical aspects such as outage probability, system throughput, and energy efficiency. Therefore, a symbiotic system of primary NOMA and IoT networks is considered in this work. In the considered system, the BS transmits the superimposed signal to the two NOMA users, i.e., the near and far users. Meanwhile, IoT devices independently transmit their signals to their dedicated IoT receivers through BC, which involves reflecting the signal received from the BS. This proposed model is versatile and can be applied to various scenarios. For instance, in a scenario where the primary network, like WiFi or cellular, communicates with a smartphone, IoT sensors or devices can employ backscattering to transmit signals to their designated IoT receivers by reflecting the signal received from the BS. Since commensal SR is the key component of this work, the path from the IoT transmitter acts as a multipath, benefiting the far users and contributing to performance improvement. This is particularly beneficial for the far users who often experience severe path loss and shadowing, where the additional multipath from the SR device helps mitigate these challenges and further enhances overall performance. The main contributions of the work are summarized as follows:

- A novel system model built on commensal SR for the IoT network to serve the IoT receiver while simultaneously enhancing the performance of the far NOMA users.
- The aim of the work is to characterize the impact of SR (commensal SR) on the NOMA system. To achieve this, the analytical expressions for the outage probability of the NOMA and IoT networks are derived.
- Further, the outage probability of the far user is obtained for both cases with and without a direct link from the BS. Additionally, system throughput and energy efficiency of the system under consideration is obtained.
- Furthermore, analytical results are developed to identify the impact of imperfect DLI cancellation on the performance of the considered IoT receivers.
- The proposed system is compared with the benchmark OMA-based system.
- The theoretical results obtained in the analysis are validated through simulation results, and valuable insights are drawn from the obtained results.

6.2 System Model

An SR communication consisting of NOMA and IoT network is considered as shown in Figure 6.1. The network consists of a BS serving two NOMA users, UE_1 and UE_2, where the UE_1 is the near (strong) user and UE_2 is the far (weak) user. The BS transmits information directly to the NOMA users and meanwhile enables the IoT transmitter ($\mathrm{IoT_T}$) to backscatter its own information to its receiver ($\mathrm{IoT_R}$) and simultaneously assist the NOMA far user. All the nodes are assumed to work in the half-duplex mode with a single antenna. The $\mathrm{IoT_T}$ is an energy-constrained node equipped with a backscatter circuit. All the channel power gains are assumed to stay constant within each transmission block. The channel links corresponding to BS-UE_1, BS-UE_2, BS-$\mathrm{IoT_T}$, $\mathrm{IoT_T}$-UE_2 and $\mathrm{IoT_T}$-$\mathrm{IoT_R}$, are h_1, h_2, f, g_1 and g_2,

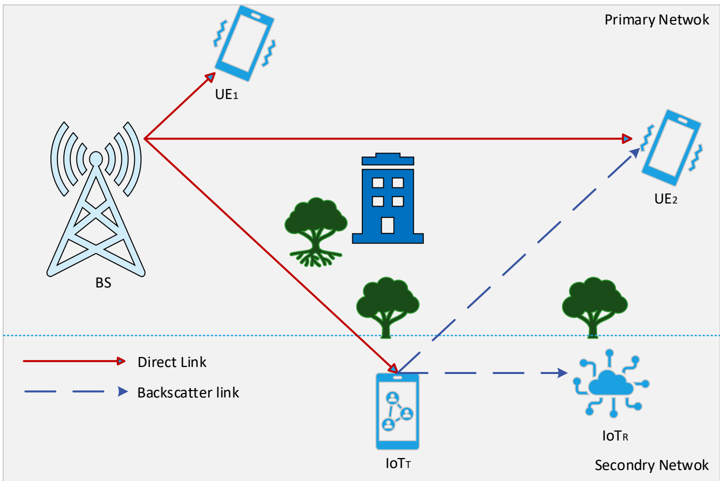

Figure 6.1: Proposed system model

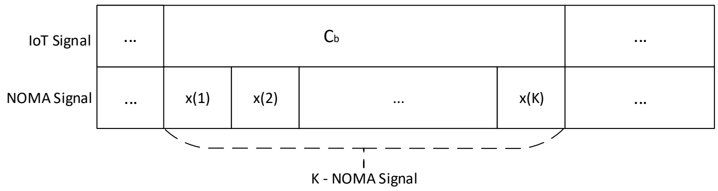

Figure 6.2: Transmission frame for commensal SR

respectively. Note that it is assumed that perfect CSI is available at the BS and the receiver nodes.

From NOMA, the BS superimposes UE_1 and UE_2 signals as $x = \sqrt{a_1}x_1 + \sqrt{a_2}x_2$, where x_1 and x_2 are signal intended for UE_1 and UE_2 with unity power, respectively. NOMA power allocation coefficients are denoted by a_1, a_2 with $a_1 + a_2 = 1$, and $a_2 > a_1$.

In the considered system, the $\mathrm{IoT_T}$ transmits its own information to $\mathrm{IoT_R}$ utilizing the same resource as of the BS. The $\mathrm{IoT_T}$ node works in a cooperative mode, transmitting its own information to $\mathrm{IoT_R}$ by modulating on the incident signal from the BS and at the same time assisting the far user. Let $C_b \sim \mathcal{CN}(0, 1)$ denote the backscatter signal with symbol period T_b. According to the symbiotic principle, it is assumed that $T_b = KT_x$, where T_x is the symbol period of x and $K >> 1$ is a positive integer. C_b spans over K-BS symbol period [17, 120]. Thus, in the k^{th} BS symbol period within one $\mathrm{IoT_T}$ symbol period, for $k = 1, \cdots, K$, the received signals at UE_1 and $\mathrm{IoT_T}$ are given as

$$y_1(k) = \sqrt{P_s}x(k)h_1 + z_1, \tag{6.1}$$

$$y_T(k) = \sqrt{P_s}x(k)f + z_i, \tag{6.2}$$

The transmitted power at BS is denoted by P_s, z_1, and z_i are additive white Gaussian noise with zero mean and σ_0^2 variance. The UE_1 directly receives the signal from the BS and decodes its own information using SIC. The SINR to decode x_2, and x_1 at UE_1 is given by $\gamma_1^2 = \frac{P_s a_2 |h_1|^2}{P_s a_1 |h_1|^2 + \sigma^2}$, and $\gamma_1^1 = \frac{P_s a_1 |h_1|^2}{\sigma^2}$, respectively. Meanwhile, the $\mathrm{IoT_T}$ modulates and backscatter information C_b to the UE_2 and $\mathrm{IoT_R}$. Accordingly, the received signals at UE_2 and $\mathrm{IoT_R}$ are given by

$$y_2(k) = \sqrt{P_s \delta}x(k)h_2 + \sqrt{P_s \alpha}C_b x(k) f g_1 + z_2, \tag{6.3}$$

$$y_R(k) = \sqrt{P_s}x(k)h_3 + \sqrt{P_s \alpha}C_b x(k) f g_2 + z_i, \tag{6.4}$$

where the power reflection coefficient is given by α, $\delta = \{0, 1\}$ is the coefficient that represents the direct link between the BS and the UE_2. The $\delta = 1$ is taken as the direct link, and $\delta = 0$, otherwise.

As $KT_x = T_b$, thus the symbol period of $\mathrm{IoT_T}$ symbol spans K x's symbols resulting C_b to remains unchanged for $k = 1, 2, \ldots, K$. The term $\sqrt{P_s \alpha}C_b x f g_1$ in (6.3) for a given C_b can be considered as the output of BS passing through the slowly varying channel $\sqrt{\alpha}C_b f g_1$ [17, 120]. Accordingly, the SINR at UE_2 is given by

$$\gamma_2 = \frac{P_s \delta |h_2|^2 a_2 + P_s \alpha a_2 |f|^2 |g_1|^2 |C_b|^2}{P_s \delta |h_2|^2 a_1 + P_s \alpha a_1 |f|^2 |g_1|^2 |C_b|^2 + \sigma^2}. \tag{6.5}$$

Meanwhile, the $\mathrm{IoT_R}$ receives its own signal from the $\mathrm{IoT_T}$. $\mathrm{IoT_R}$ first decodes the primary signal x(k) by treating the BD signal as a multipath component. After decoding x(k), the $\mathrm{IoT_R}$ also applies the SIC technique to remove the DLI. Assuming that the primary signal component is removed perfectly, the obtained intermediate signal as

$$y_R^D(k) = \sqrt{P_s \alpha}C_b x(k) f g_2 + z_i, \tag{6.6}$$

Due to the symbiotic setup, one IoT_R symbol is transmitted using K successive BS symbols. Since $\mathbb{E}[|s(n)|^2] = 1$, and one C_b modulated into K consecutive $x(k)'s$ symbols, for $k = 1, \cdots, K$, thus maximal ratio combing can be performed on $y_R(k)$, for $k = 1, \cdots, K$, which are received in K consecutive $x(k)'s$ symbol periods, to decode IoT_R symbol. The SNR for decoding C_b is increased by K times, at the cost of symbol rate decrease by K [120]. Thus an approximated SNR at IoT_R is given by

$$\gamma_i = \frac{P_s K \alpha |f|^2 |g_2|^2}{\sigma^2}, \tag{6.7}$$

However, according to the SIC principle, if the direct link is cancelled from the y_r, the SIC is perfect, and the direct link signal can be completely removed. Otherwise, decoding of C_b will be carried out in the presence of residual interference due to imperfect DLI cancellation. Thus SINR in the presence of imperfect DLI cancellation at IoT_R to decode C_b is given by

$$\gamma_i^D = \frac{P_s K \alpha |f|^2 |g_2|^2}{P_s \beta |h_3|^2 + \sigma^2}, \tag{6.8}$$

where β represents the residual interference due to imperfect SIC, $0 \leq \beta \leq 1$, i.e., $\beta = 0$ refers to perfect SIC.

6.3 Performance Analysis

This section analyses the performance analysis of UE_2 and IoT_R in terms of outage probability, system throughput and energy efficiency. In the considered model, the performance of UE_1 is the same as that of two users' NOMA systems as depicted by γ_1^2 and γ_1^1. Thus, the performance analysis of UE_2 and IoT_R is focused in the remainder of the chapter.

6.3.1 Outage probability

This subsection derives an analytical expression of the outage probability.

Outage probability of UE_1

The outage probability of UE_1 is given as

$$\mathrm{P}_1 = \Pr\{\gamma_1^1 \leq \gamma_{th1}, \gamma_1^2 \leq \gamma_{th2}\}, \tag{6.9}$$

where $\gamma_{th1} = 2^{R_1} - 1$, R_1 is the target rate of UE_1. Simplifying the above equation, the outage probability of UE_1 is given as

$$\mathrm{P}_1 = 1 - \exp\left(-\max\left(\frac{\gamma_{th2}}{\rho(a_2 - a_1\gamma_{th2})}, \frac{\gamma_{th1}}{\rho a_1}\right)\right). \tag{6.10}$$

Outage probability of UE_2 with the direct link

The outage probability of UE_2 is defined as follows

$$\mathrm{P}_2 = \Pr\{\gamma_2 \leq \gamma_{th2}\} \tag{6.11}$$

where $\gamma_{th2} = 2^{R_2} - 1$, and R_2 is the target rate of UE_2. Substituting (6.5) with $\delta = 1$ in (6.11). After solving, the outage probability of UE_2 with a direct link is given as

$$\mathrm{P}_2^D = \Pr\left\{\frac{P_s|h_2|^2 a_2 + P_s\alpha a_2|f|^2|g_1|^2|C_b|^2}{P_s|h_2|^2 a_1 + P_s\alpha a_1|f|^2|g_1|^2|C_b|^2 + \sigma^2} \leq \gamma_{th2}\right\}, \tag{6.12}$$

After simplification (6.12) reduces to

$$\mathrm{P}_2^D = \Pr\left\{|h_2|^2 \leq \zeta_1 - \alpha|f|^2|g_1|^2|C_b|^2\right\}, \tag{6.13}$$

where $\zeta_1 = \frac{\gamma_{th2}}{(a_2 - a_1\gamma_{th2})\rho}$, $\rho = \frac{P_s}{\sigma^2}$. As Rayleigh fading is assumed for all the channels, the PDF of channel gains is as follows. $f_{|h_1|^2}(x) = \frac{\exp\left(-x/\lambda_{h_1}\right)}{\lambda_{h_1}}$, $f_{|f|^2}(x) = \frac{\exp\left(-x/\lambda_f\right)}{\lambda_f}$, $f_{|g_1|^2}(x) = \frac{\exp\left(-x/\lambda_{g_1}\right)}{\lambda_{g_1}}$, $f_{|C_b|^2}(x) = \exp(-x)$, Let $Z = |g_1|^2|C_b|^2$, which means that the PDF of Z is given as $f_Z(x) = \frac{2}{\lambda_{g_1}}\mathrm{K}_0\left(2\sqrt{\frac{x}{\lambda_{g_1}}}\right)$ according to [113]. Thus, utilizing the PDF, (6.13) is expressed as follows

$$\mathrm{P}_2^D = \int_{z=0}^{\infty} \int_{y=0}^{\frac{\zeta_1}{\alpha z}} \int_{x=0}^{\zeta_1 - \alpha yz} \frac{\exp\left(-x/\lambda_{h_1}\right)}{\lambda_{h_1}} \frac{\exp\left(-y/\lambda_f\right)}{\lambda_f} \frac{2}{\lambda_{g_1}} \mathrm{K}_0 \left(2\sqrt{\frac{z}{\lambda_{g_1}}}\right) dxdydz, \tag{6.14}$$

After solving the integration, (6.14) reduces to

$$\mathrm{P}_2^D = 1 - \int_{z=0}^{\infty} \exp\left(\frac{-\zeta_1}{\alpha z}\right) - \frac{\exp\left(\frac{-\zeta_1}{\lambda_{h_2}}\right)}{\lambda_f} \left(1 - \exp\left(-\left(\frac{\lambda_{h_1} - \alpha z \lambda_f}{\lambda_{h_1}\lambda_f}\right)\frac{\zeta_1}{\alpha z}\right)\right) \frac{2\mathrm{K}_0\left(2\sqrt{\frac{z}{\lambda_{g1}}}\right)}{\lambda_{g_1}} dz, \tag{6.15}$$

The integral in (6.15) is challenging to solve. Substituting $z = \frac{1+z_1}{1-z_1}$, and utilizing GCQ [53, e.q. 8.8]

$$\int_{-1}^{+1} \frac{f(x)}{\sqrt{(1-x)^2}} dx \approx \frac{\pi}{N_1} \sum_{m=1}^{N_1} f\left(\cos\left(\frac{(2m-1)\pi}{2N_1}\right)\right), \tag{6.16}$$

where N_1 is the complexity-accuracy trade-off parameter. After some simplification, the outage probability of UE_2 with a direct link is given as

$$\mathrm{P}_2^D \approx 1 - \sum_{n=1}^{N_1} \frac{4\sqrt{1-\phi_n^2}\pi}{(1-\phi_n)^2 N_1 \lambda_{g_1}} \exp\left(\frac{-\zeta_1}{\alpha\Delta}\right) 2\mathrm{K}_0\left(\sqrt{\frac{4\Delta}{\lambda_{g_1}}}\right) - \exp\left(\frac{-\zeta_1}{\lambda_{h_2}}\right) \frac{\lambda_{h_2}}{\lambda_{g_1}} \sum_{n=1}^{N_1} \frac{1 - \exp\left(\frac{-(\lambda_{h_2} - \alpha\Delta)\zeta_1}{\alpha\Delta\lambda_f\lambda_{h_2}}\right)}{\lambda_{h_2} - \lambda_f \alpha\Delta} \frac{\sqrt{1-\phi_n^2}\pi}{(1-\phi_n)^2 N_1} \mathrm{K}_0\left(\sqrt{\frac{4\Delta}{\lambda_{g_1}}}\right), \tag{6.17}$$

where $\Delta = \frac{1+\phi_n}{1-\phi_n}$ and $\phi_n = \cos\left(\frac{(2m-1)\pi}{2N_1}\right)$.

Outage probability of UE_2 without the direct link

The outage probability of UE_2 without a direct link is obtained by substituting $\delta = 0$ in (6.5). After simplification, the outage probability expression without a direct link is reduced to

$$\mathrm{P}_2^{WD} = \Pr\left\{|f|^2 \leq \frac{\zeta_1}{\alpha|g_1|^2|C_b|^2}\right\}, \tag{6.18}$$

utilizing the PDF in the (6.18), and after simplification the outage probability is expressed as follows

$$\mathrm{P}_2^{WD} = 1 - \int_{z=0}^{\infty} \exp\left(\frac{-\zeta_1}{\alpha z \lambda_f}\right) \frac{2}{\lambda_{g_1}} \mathrm{K}_0\left(2\sqrt{\frac{z}{\lambda_{g_1}}}\right) dz. \tag{6.19}$$

The above integration in (6.19) is solved using GCQ, and the obtained analytical expression is given as

$$\mathrm{P}_2^{WD} \approx 1 - \sum_{n=1}^{N_1} \frac{2\sqrt{1-\phi_n^2}\,\delta_1 \pi}{(1-\phi_n)^2 N_1 \lambda_{g_1}} \exp\left(\frac{-\zeta_1}{\alpha\Delta}\right) 2\mathrm{K}_0\left(\sqrt{\frac{4\Delta}{\lambda_{g_1}}}\right). \tag{6.20}$$

Outage probability of $\mathbf{IoT_R}$

The outage probability of $\mathrm{IoT_R}$ is defined as

$$\mathrm{P}_i = \Pr\{\gamma_i \leq \gamma_{thi}\} \tag{6.21}$$

where $\gamma_{thi} = 2^{KR_i} - 1$, and R_i is the target rate of $\mathrm{IoT_R}$. Substituting (6.8) in (6.21), the outage probability expression reduces to

$$\mathrm{P}_i = \Pr\left\{\frac{P_s K \alpha |f|^2 |g_2|^2}{\sigma^2} \leq \gamma_{thi}\right\}, \tag{6.22}$$

$$\mathrm{P}_i = \Pr\left\{|f|^2 \leq \frac{\gamma_{thi}}{|g_2|^2 \rho K \alpha}\right\}, \tag{6.23}$$

$$\mathrm{P}_i = \int_{x=0}^{\infty} \frac{1}{\lambda_{g_2}} \left(1 - \exp\frac{-\gamma_{thi}}{x\rho K \alpha \lambda_f}\right) \exp\frac{-x}{\lambda_{g_2}} dx, \tag{6.24}$$

utilizing [54, eq. 3.324], the above integral can be obtained as follows. Thus, the outage probability of $\mathrm{IoT_R}$ with perfect DLI cancellation is given as

$$\mathrm{P}_i = 1 - \sqrt{\frac{4\gamma_{thi}\lambda_{g_2}}{\rho K\alpha\lambda_f}}\mathrm{K}_1\left(\sqrt{\frac{4\gamma_{thi}}{\rho K\alpha\lambda_f\lambda_{g_2}}}\right) \tag{6.25}$$

Outage probability of $\mathbf{IoT_R}$ with imperfect DLI cancellation

Substituting (6.8) in (6.21), and after some straightforward algebraic manipulations, the outage probability is given as

$$\mathrm{P}_i^D = \Pr\left\{P_sK\alpha|f|^2|g_2|^2 \leq \gamma_{thi}(P_s\beta|h_3|^2 + \sigma^2)\right\}. \tag{6.26}$$

Utilizing the PDF of channel gains, the above equation is simplified as follows.

$$\mathrm{P}_i^D = 1 - \int_{x=0}^{\infty}\frac{1}{\lambda_{g_2}\lambda_{h_3}}\sqrt{\frac{4\gamma_{thi}\lambda_{g_2}(1+\rho\beta y)}{\rho K\alpha\lambda_f}}\mathrm{K}_1\left(\sqrt{\frac{4\gamma_{thi}(1+\rho\beta y)}{\rho K\alpha\lambda_f\lambda_{g_2}}}\right)\exp\frac{-y}{\lambda_{h_3}}dy. \tag{6.27}$$

The integral in (6.27) is challenging to solve. Thus, using GCQ, the analytical expression of outage probability of $\mathrm{IoT_R}$ with imperfect DLI cancellation is given by

$$\begin{aligned}\mathrm{P}_i^D \approx & 1 - \sum_{n=1}^{N_1}\frac{2\sqrt{1-\phi_n^2}\delta_1\pi}{(1-\phi_n)^2N_1\lambda_{g_1}}\sqrt{\frac{4\gamma_{thi}\lambda_{g_2}(1+\rho\beta\Delta)}{\rho K\alpha\lambda_f}}\frac{1}{\lambda_{g_2}\lambda_{h_3}}\mathrm{K}_1\left(\sqrt{\frac{4\gamma_{thi}(1+\rho\beta\Delta)}{\rho K\alpha\lambda_f\lambda_{g_2}}}\right)\\ & \exp\left(\frac{-\Delta}{\lambda_{h_3}}\right),\end{aligned} \tag{6.28}$$

6.3.2 System throughput

This subsection presents the delay-sensitive system throughput achieved by the proposed system. The system throughput of the considered system at the fixed target rate using the outage probability with the direct link is given as

$$\mathbf{ST}^D = (1-\mathrm{P}_1) * R_1 + (1-\mathrm{P}_2^D) * R_2 + (1-\mathrm{P}_i) * R_i, \tag{6.29}$$

The system throughput of the considered system without a direct link is given as

$$\mathbf{ST}^{WD} = (1 - \mathrm{P}_1) * R_1 + (1 - \mathrm{P}_2^{WD}) * R_2 + (1 - \mathrm{P}_i) * R_i, \tag{6.30}$$

6.3.3 Energy efficiency

In 6G communication, energy efficiency is a crucial performance metric that optimises power usage to facilitate high-speed data rates. The energy efficiency is formally defined as the ratio between the maximum achievable throughput and the total power expended by the system. The energy efficiency of the considered system with and without direct link is expressed as

$$\mathbf{EE}^{D} = \frac{\mathbf{ST}^{D}}{P_s}, \tag{6.31}$$

$$\mathbf{EE}^{WD} = \frac{\mathbf{ST}^{WD}}{P_s}, \tag{6.32}$$

6.4 Numerical and Simulation Results

This section presents the simulation and numerical results of the considered system. The simulation parameters are considered as follows. The NOMA power allocation coefficient $a_1 = 0.3$, $K = 128$ [120], the power reflection coefficient $\alpha = 0.25$, the channel gains $\lambda_{h_1} = \lambda_f = \lambda_{g_1} = \lambda_{g_2} = 1$ and $\lambda_{h_2} = 0.5$. The target data rate $R_1 = R_2 = 1$ and $R_i = 0.05$. Monte Carlo simulations are performed using Matlab to validate the obtained analytical expression. In the figures, Matlab simulations are denoted by Sim. and Ana. denotes analytical results.

In Figure 6.3, the outage probability of UE_2 and $\mathrm{IoT_R}$ are presented w.r.t. the transmit SNR. From the figure, it is observed that as the SNR increases, the outage probability decreases, and the performance of both users improves. Further, the outage probability of UE_2 is compared with that of the benchmark OMA technique. In OMA, the transmission is completed in two-time slots. For a fair comparison, the target rates for OMA and NOMA are assumed same, owing to the requirement of additional time slots by the OMA to complete the transmission. At an outage probability of 10^{-3}, the NOMA-based system provides a 1 dB SNR gain over the OMA system. Furthermore, the outage of UE_2 is assessed in the scenario where

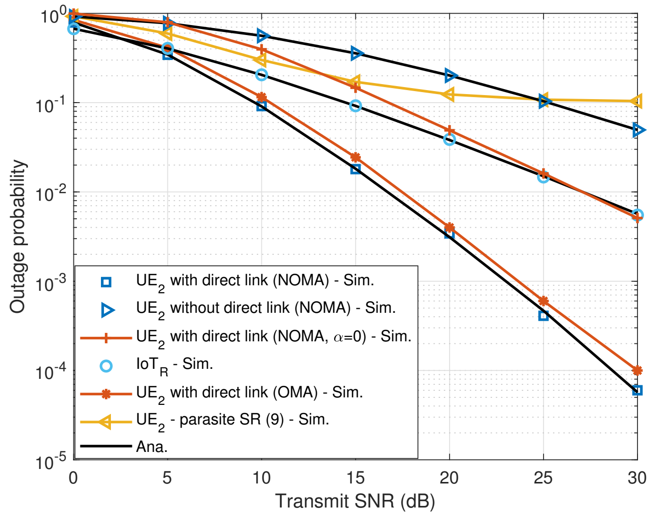

Figure 6.3: Outage probability w.r.t. SNR.

there is no transmission from $\mathrm{IoT_T}$ (i.e., $\alpha = 0$). The results indicate a significant increase in outage when the link between $\mathrm{IoT_T}$ and UE_2 is absent. At an outage level of 10^{-2}, UE_2 with the presence of the $\mathrm{IoT_T}$ link exhibits a notable gain of 10 dB compared to without UE_2-$\mathrm{IoT_R}$ link. Furthermore, the outage probability is compared with the parasitic SR-NOMA system [113]. It is observed that as the SNR increases, the outage probability of both parasitic and commensal decreases in the low SNR region. However, the parasitic SR system shows a noise floor in the high SNR region. Conversely, the proposed system does not show any noise floor because of the commensal setup. This is due to the fact that signal from $\mathrm{IoT_T}$ is treated as a multipath component, resulting in improved performance for UE_2.

In Figure 6.4, the outage probability plots for both UE_2 and $\mathrm{IoT_R}$ are presented w.r.t the power reflection coefficient (α) and different target rate values (R_i and R_2). The α parameter varies within the range of 0 to 1, while ρ is maintained at 15 dB. Notably, when $\alpha = 0$, $\mathrm{IoT_T}$ remains in the silent mode, i.e., reflecting no symbols, thereby resulting in a unity outage for $\mathrm{IoT_R}$. As α increases, the outage performance for both $\mathrm{IoT_R}$ and UE_2 demonstrates noticeable improvements. Additionally, it is observed that as R_i decreases, the outage probability of $\mathrm{IoT_R}$ also decreases. When $R_i = 0.1$, the outage probability shows a marginal improvement with increasing α compared to $R_i = 0.01$. Hence, this proposed model is well-suited for low data rate IoT devices like sensor nodes.

Figure 6.5 depict the relationship between the system throughput and the SNR.

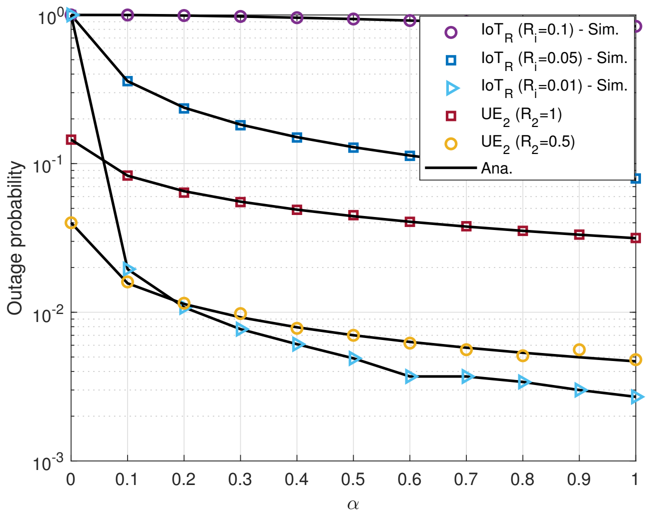

Figure 6.4: Outage probability w.r.t. α.

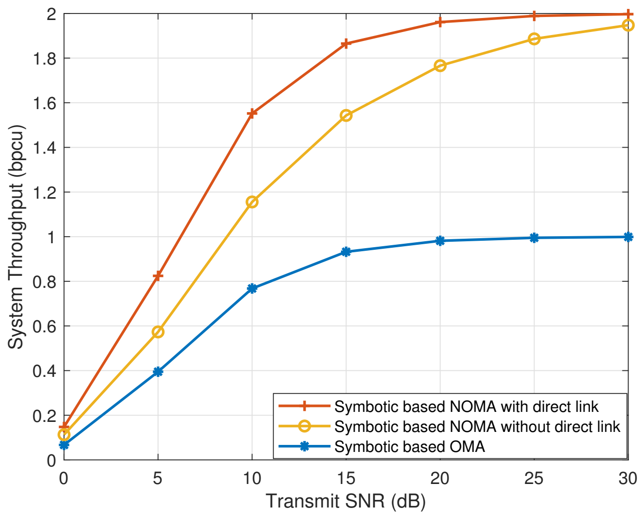

Figure 6.5: System throughput w.r.t. SNR.

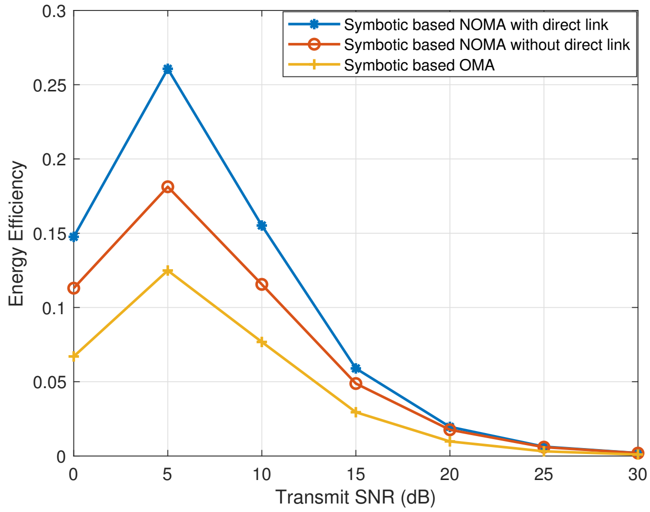

Figure 6.6: Energy efficiency w.r.t. SNR.

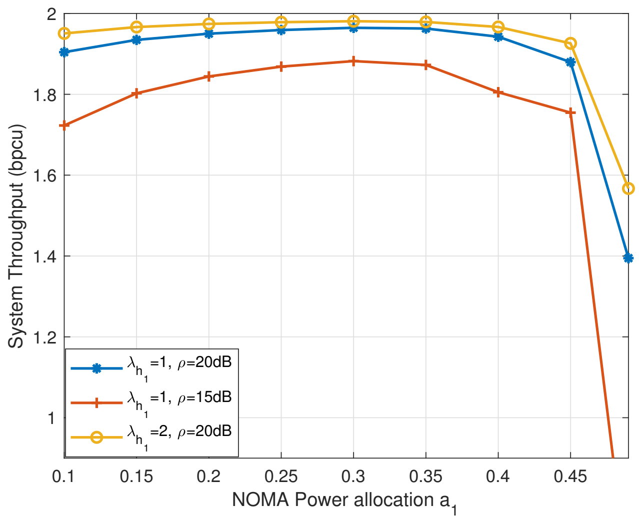

Figure 6.7: Outage probability w.r.t. a_1.

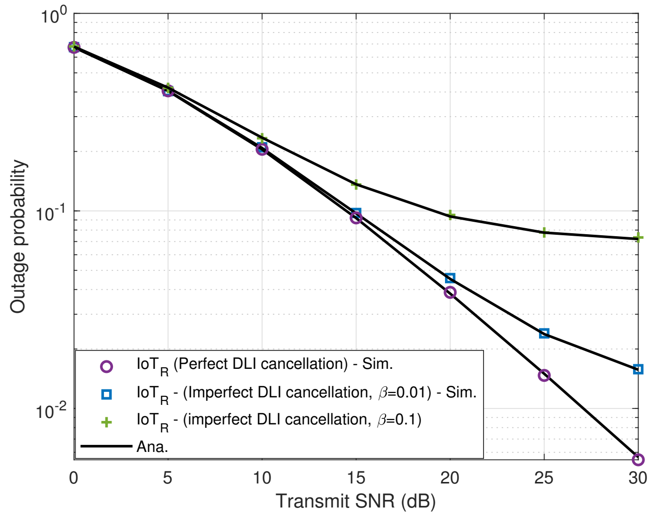

Figure 6.8: Outage probability w.r.t. SNR.

As SNR rises, the throughput increases until it reaches a constant maximum value, representing the highest achievable throughput for a given target rate. Notably, the proposed NOMA system exhibits superior performance compared to the OMA system. At a system throughput of 0.8 bpcu, the NOMA-based system with direct link provides an SNR gain of 5 dB over the OMA system.

In Figure 6.6, the energy efficiency is plotted w.r.t to SNR, offering insights into optimizing the utilization of energy resources. It is evident that energy efficiency increases as SNR rises and peaks at a specific SNR value. Particularly, an SNR threshold exists at which maximum energy efficiency is achieved. However, as SNR enters the high range, energy efficiency begins to decline due to the consumption of energy surpassing the achievable throughput. Additionally, the plot of energy efficiency is presented for scenarios both with and without a direct link, demonstrating that the system with a direct link outperforms the one without a direct link. Furthermore, the proposed NOMA system exhibits superior energy efficiency compared to the OMA system, affirming its potential for more energy-efficient wireless communication.

In Figure 6.7, the system throughput is plotted with respect to the power allocation coefficient (a_1). The parameter a_1 varies between 0.1 and 0.5, while ρ remains constant. As a_1 increases, the system throughput initially increases to a peak level before subsequently diminishing. An increase in the a_1 results in increased power allocation for UE_1, thereby increasing the overall system throughput. However, further increments in a_1 reduce the power allocated to UE_2, resulting in overall performance degradation, as indicated by the figure. The plot illustrates that the optimal value of a_1 that maximizes the system throughput lies within the range of 0.25 to 0.35 for both $\rho = 15$ dB and $\rho = 20$ dB. Further, it is observed that as λ_{h_1} increases, the system throughput increases due to an increase in the channel gain between the BS and the UE_1.

In Figure 6.8, illustrates the outage probability of $\mathrm{IoT_R}$ with respect to the SNR, considering both perfect and imperfect DLI cancellation. It is evident that as the residual interference (β) due to imperfect DLI cancellation increases, the user's performance deteriorates. Notably, at an outage probability of 2×10^{-2}, $\mathrm{IoT_R}$ users with perfect DLI cancellation show an SNR gain of 2 dB compared to those with imperfect DLI cancellation ($\beta = 0.01$). Further, it is observed that at low SNR, the performance of $\mathrm{IoT_R}$ with perfect DLI cancellation closely resembles imperfect DLI cancellation. However, as SNR increases, the interference presence becomes more pronounced, leading to performance degradation. This is because as the SNR increases, the interference due to imperfect DLI cancellation increases, resulting in the outage probability increasing effectively.

6.5 Summary

In this chapter, the study delves into an SR communication-based NOMA system integrated with an IoT network. It established analytical expressions for the outage probability for both the NOMA user and the IoT receiver while also deriving insights into the system throughput and energy efficiency. In addition, the performance of the NOMA far user is thoroughly examined, comparing scenarios with and without direct links from the base station. The results also indicate that IoT transmission not only supports its own data transmission but also enhances the performance of the NOMA far user. The impact of the power reflection coefficient and a target rate on user performance was also analyzed. These findings unequivocally underscore the superiority of the proposed NOMA system, particularly when integrated with self-sustainable IoT nodes, showcasing a significant performance improvement compared to traditional OMA-based systems.

Chapter 7

Conclusions and Future Works

7.1 Conclusions

The thesis explores advanced techniques in NOMA systems and their integration with IoT networks, addressing the evolving demands for spectral and energy-efficient wireless communication. By focusing on various aspects of NOMA, including higher order modulation schemes, interference management, and EH technologies, the research comprehensively analyses how these techniques can be leveraged to enhance system efficiency and performance. Through a detailed examination of NOMA systems, the thesis provides valuable insights into how to optimize system performance in real-world scenarios. Integrating IoT networks with NOMA is particularly significant, as it addresses the need for scalable and sustainable communication solutions in the face of rapidly increasing device connectivity. By exploring various cooperative communication strategies, the thesis contributes to a deeper understanding of achieving reliable and energy-efficient communication systems. The findings also highlight the potential of combining NOMA with advanced technologies such as BC and SR to create more robust and self-sustaining networks. The research emphasizes the importance of practical considerations, such as imperfect CSI and hardware impairments, in designing NOMA systems.

Intially, the thesis explores the downlink NOMA system with two users, deriving closed-form expressions for the ASER of generalized M-ary HQAM. The findings demonstrate that NOMA significantly outperforms OMA in HQAM scenarios. Further, it is observed that at an ASER of HQAM provides a gain of 0.4 dB over SQAM scheme. A power allocation criterion is introduced that prevents error floors at high SNRs, with insights into how modulation orders impact user performance. Adhering to the proposed criterion ensures consistent ASER performance across different constellation orders.

Expanding to multi-user NOMA systems, a multiple feedback-based successive interference cancellation algorithm is proposed to address multi-user interference and error propagation. This algorithm proves superior to conventional SIC methods by avoiding error floors at high SNRs.

Additionally, the role of cooperative relaying with EH relay nodes is emphasized for enhancing coverage, diversity, and reliability. Performance analysis of a downlink NOMA system with multiple EH relays over Nakagami-m fading channels reveals significant degradation under practical conditions such as imperfect SIC and CSI. The study finds that increasing the number of active relay nodes improves performance, and identifies an optimal power splitting coefficient for maximizing system throughput. The effects of power allocation coefficients and block time fractions on user performance are also examined.

A hybrid backscatter-based CDRT-NOMA system is analyzed, considering practical challenges like nonlinear EH, imperfect CSI, and RHI. Results show that a self-sustainable backscatter relay node provides a significant performance boost compared to traditional EH-based systems, highlighting the potential of backscatter technology for self-sustaining wireless communication networks.

An SR communication-based NOMA system integrated with an IoT network is analyzed. Integrating NOMA with IoT networks, the analysis establishes analytical expressions for outage probability, system throughput, and energy efficiency. The performance of the NOMA far user is examined in scenarios with and without direct links from the base station, demonstrating that IoT transmission enhances both its own data transmission and the performance of the NOMA far user. The impact of the power reflection coefficient and target rate on user performance underscores the advantages of integrating NOMA with self-sustainable IoT nodes. The proposed SR system integrates IoT and NOMA transmissions, resulting in a spectrum- and energy-efficient communication design that facilitates low-power wireless communication.

Overall, the thesis advances the understanding of NOMA systems by incorporating advanced modulation techniques, cooperative relaying, and backscatter communication, addressing practical challenges, and enhancing system performance and efficiency. The thesis highlights the potential of NOMA based systems in enabling spectrally and energy efficient wireless communication networks.

7.2 Future Works

- Future work should explore the integration of NOMA with integrated sensing and communication (ISAC) in future wireless standards. NOMA's capability to serve multiple users in the same resources block can complement ISAC's dual function of sensing and communication. Research can focus on developing new NOMA-based ISAC frameworks that optimize the trade-offs between communication capacity and sensing accuracy, ensuring efficient resource allocation, and minimizing interference.

- ISAC with backscatter tag-assisted NOMA systems to enhance spectral and energy efficiency in next-generation wireless networks. In this context, backscatter tags can be leveraged to simultaneously perform communication and sensing functions without requiring a dedicated power source, thereby facilitating low-power operations.

- Optimal resource utilization in wireless communication, particularly with the integration of NOMA, BC, and SR, is crucial for next-generation networks. The focus should be on developing strategies for optimizing power allocation, interference management, and user scheduling within these technologies to ensure high performance and energy-efficient communication.

- Due to the use of spectrally and energy-efficient systems, the work presented in this thesis can also be extended to beyond 5G technologies, such as intelligent reflecting surfaces (IRS), visible light communication (VLC), and others, to achieve high coverage, energy efficiency, and throughput.

References

[1] Y. Lu and X. Zheng, "6G: A survey on technologies, scenarios, challenges, and the related issues," *Journal of Industrial Information Integration*, vol. 19, p. 100158, 2020. [Online]. Available: https://www.sciencedirect.com/science/article/pii/S2452414X20300339

[2] P. K. Singya, P. Shaik, N. Kumar, V. Bhatia, and M.-S. Alouini, "A survey on higher-order QAM constellations: technical challenges, recent advances, and future trends," *IEEE Open J. Commun. Soc.*, vol. 2, pp. 617–655, Mar. 2021.

[3] Q. Wu, S. Zhang, B. Zheng, C. You, and R. Zhang, "Intelligent reflecting surface-aided wireless communications: A tutorial," *IEEE Trans. Commun.*, vol. 69, no. 5, pp. 3313–3351, May 2021.

[4] B. Zheng, C. You, W. Mei, and R. Zhang, "A survey on channel estimation and practical passive beamforming design for intelligent reflecting surface aided wireless communications," *IEEE Commun. Surv. Tutor.*, vol. 24, no. 2, pp. 1035–1071, 2nd Quart. 2022.

[5] D. Raychaudhuri and N. B. Mandayam, "Frontiers of wireless and mobile communications," *IEEE Proceed.*, vol. 100, no. 4, pp. 824–840, Feb. 2012.

[6] Z. Ding, X. Lei, G. K. Karagiannidis, R. Schober, J. Yuan, and V. K. Bhargava, "A survey on non-orthogonal multiple access for 5G networks: research challenges and future trends," *IEEE J. Sel. Areas Commun.*, vol. 35, no. 10, pp. 2181–2195, Jul. 2017.

[7] P. Swami, V. Bhatia, S. Vuppala, and T. Ratnarajah, "A cooperation scheme for user fairness and performance enhancement in NOMA-HCN," *IEEE Trans. Veh. Technol.*, vol. 67, no. 12, pp. 11 965–11 978, Oct. 2018.

[8] M. Vaezi, R. Schober, Z. Ding, and H. V. Poor, "Non-orthogonal multiple access: Common myths and critical questions," *IEEE Wireless Commun.*, vol. 26, no. 5, pp. 174–180, Sep. 2019.

[9] Y. Liu, Z. Qin, M. Elkashlan, Z. Ding, A. Nallanathan, and L. Hanzo, "Nonorthogonal multiple access for 5G and beyond," *Proc. IEEE*, vol. 105, no. 12, pp. 2347–2381, Dec. 2017.

[10] L. Dai, B. Wang, Y. Yuan, S. Han, I. Chih-Lin, and Z. Wang, "Non-orthogonal multiple access for 5G: solutions, challenges, opportunities, and future research trends," *IEEE Commun. Mag.*, vol. 53, no. 9, pp. 74–81, Jun. 2015.

[11] N. Nomikos, T. Charalambous, I. Krikidis, D. N. Skoutas, D. Vouyioukas, M. Johansson, and C. Skianis, "A survey on buffer-aided relay selection," *IEEE Commun. Surv. Tutor.*, vol. 18, no. 2, pp. 1073–1097, 2nd Quart. 2016.

[12] C. Hoymann, D. Astely, M. Stattin, G. Wikstrom, J.-F. Cheng, A. Hoglund, M. Frenne, R. Blasco, J. Huschke, and F. Gunnarsson, "LTE release 14 outlook," *IEEE Commun. Mag.*, vol. 54, no. 6, pp. 44–49, Jun. 2016.

[13] M.-L. Ku, W. Li, Y. Chen, and K. R. Liu, "Advances in energy harvesting communications: Past, present, and future challenges," *IEEE Commun. Sur. Tutor.*, vol. 18, no. 2, pp. 1384–1412, 1st Quart. 2016.

[14] J. Huang, C.-C. Xing, and C. Wang, "Simultaneous wireless information and power transfer: Technologies, applications, and research challenges," *IEEE Commun. Mag.*, vol. 55, no. 11, pp. 26–32, Nov. 2017.

[15] T. D. P. Perera, D. N. K. Jayakody, S. K. Sharma, S. Chatzinotas, and J. Li, "Simultaneous wireless information and power transfer (SWIPT): Recent advances and future challenges," *IEEE Commun. Sur. Tutor.*, vol. 20, no. 1, pp. 264–302, 1st Quart. 2018.

[16] Z. Ding and H. V. Poor, "On the application of BAC-NOMA to 6G umMTC," *IEEE Commun. Lett.*, vol. 25, no. 8, pp. 2678–2682, Aug. 2021.

[17] R. Long, Y.-C. Liang, H. Guo, G. Yang, and R. Zhang, "Symbiotic radio: A new communication paradigm for passive internet of things," *IEEE Internet Things J.*, vol. 7, no. 2, pp. 1350–1363, Feb. 2020.

[18] A. Al-Nahar, R. Jäntti, G. Zheng, D. Mishra, and M. Nie, "Ergodic secrecy rate analysis and optimal power allocation for symbiotic radio networks," *IEEE Access*, vol. 11, pp. 82 327–82 337, Aug. 2023.

[19] T. S. Rappaport, *Wireless Communications– Principles and Practice.* Horizon House Publications, Inc., 2002, vol. 45, no. 12.

[20] M. K. Simon and M.-S. Alouini, *Digital Communication over Fading Channels.* John Wiley & Sons, 2005, vol. 95.

[21] N. C. Beaulieu and C. Cheng, "Efficient Nakagami-m fading channel simulation," *IEEE Trans. Veh. Technol.*, vol. 54, no. 2, pp. 413–424, Apr. 2005.

[22] S. M. Kay, *Fundamental of statistical signal processing: estimation theory.* Prentice-hall, 1993.

[23] D. Do, T. Anh Le, T. N. Nguyen, X. Li, and K. M. Rabie, "Joint impacts of imperfect CSI and imperfect SIC in cognitive radio-assisted NOMA-V2X communications," *IEEE Access*, vol. 8, pp. 128 629–128 645, Jul. 2020.

[24] Taesang Yoo and A. Goldsmith, "Capacity and power allocation for fading MIMO channels with channel estimation error," *IEEE Trans. on Inf. Theory*, vol. 52, no. 5, pp. 2203–2214, May 2006.

[25] F. Fang, H. Zhang, J. Cheng, S. Roy, and V. C. M. Leung, "Joint user scheduling and power allocation optimization for energy-efficient noma systems with imperfect CSI," *IEEE J. Sel. Areas in Commun.*, vol. 35, no. 12, pp. 2874–2885, Dec. 2017.

[26] T. Schenk, *RF imperfections in high-rate wireless systems: impact and digital compensation.* Springer, 2008.

[27] E. Bjornson, M. Matthaiou, and M. Debbah, "A new look at dual-hop relaying: Performance limits with hardware impairments," *IEEE Trans. Commun.*, vol. 61, no. 11, pp. 4512–4525, Nov. 2013.

[28] S. Kim, H. W. Kim, K. Kang, and D. S. Ahn, "Performance enhancement in future mobile satellite broadcasting services," *IEEE Commun. Mag.*, vol. 46, no. 7, Jul. 2008.

[29] Y. Yang, H. Hu, J. Xu, and G. Mao, "Relay technologies for WiMAX and LTE-Advanced mobile systems," *IEEE Commun. Mag.*, vol. 47, no. 10, Oct. 2009.

[30] P. Swami, V. Bhatia, S. Vuppala, and T. Ratnarajah, "User fairness in noma-hetnet using optimized power allocation and time slotting," *IEEE Syst. J.*, vol. 15, no. 1, pp. 1005–1014, Mar. 2021.

[31] A. S. Parihar, P. Swami, V. Bhatia, and Z. Ding, "Performance analysis of SWIPT enabled cooperative-NOMA in heterogeneous networks using carrier sensing," *IEEE Trans. Veh. Technol.*, vol. 70, no. 10, pp. 10 646–10 656, Oct. 2021.

[32] Y. He, R. Zhang, and N. Ye, "5G-oriented non-orthogonal multiple access technology," *Int. J. Commun. Syst.*, vol. 35, no. 5, p. e4574, 2022, e4574 IJCS-20-0450.R1. [Online]. Available: https://onlinelibrary.wiley.com/doi/abs/10.1002/dac.4574

[33] Z. Xiang, W. Yang, Y. Cai, Z. Ding, Y. Song, and Y. Zou, "NOMA-assisted secure short-packet communications in IoT," *IEEE Wirel. Commun.*, vol. 27, no. 4, pp. 8–15, Aug. 2020.

[34] Y. Liu, Z. Qin, Y. Cai, Y. Gao, G. Y. Li, and A. Nallanathan, "Uav communications based on non-orthogonal multiple access," *IEEE Wirel. Commun.*, vol. 26, no. 1, pp. 52–57, Feb. 2019.

[35] A. I. Perez-Neira, M. Caus, and M. A. Vazquez, "Non-orthogonal transmission techniques for multibeam satellite systems," *IEEE Commun. Mag.*, vol. 57, no. 12, pp. 58–63, Dec. 2019.

[36] A. S. Parihar, P. Swami, and V. Bhatia, "On performance of swipt enabled ppp distributed cooperative noma networks using stochastic geometry," *IEEE Trans. Veh. Technol.*, vol. 71, no. 5, pp. 5639–5644, 2022.

[37] J. Jose, A. Agarwal, V. Bhatia, and O. Krejcar, "Outage probability minimization based power control and channel allocation in underlay D2D-NOMA for IoT networks," *Trans. Emerg. Tel. Tech.*, vol. 33, no. 9, p. e4568, Sep. 2022.

[38] S. Parvez, P. K. Singya, and V. Bhatia, "On ASER analysis of energy efficient modulation schemes for a device-to-device MIMO relay network," *IEEE Access*, vol. 8, pp. 2499–2512, Dec. 2020.

[39] N. Kumar and V. Bhatia, "Exact ASER analysis of rectangular QAM in two-way relaying networks over Nakagami-m fading channels," *IEEE Wirel. Commun. Lett.*, vol. 5, no. 5, pp. 548–551, Oct. 2016.

[40] N. Kumar, P. K. Singya, and V. Bhatia, "ASER analysis of hexagonal and rectangular QAM schemes in multiple-relay networks," *IEEE Trans. Veh. Techno.*, vol. 67, no. 2, pp. 1815–1819, Feb. 2018.

[41] T. Assaf, A. Al-Dweik, M. E. Moursi, and H. Zeineldin, "Exact BER performance analysis for downlink NOMA systems over nakagami- m fading channels," *IEEE Access*, vol. 7, pp. 134 539–134 555, Sep. 2019.

[42] I. Lee and J. Kim, "Average symbol error rate analysis for non-orthogonal multiple access with M-ary QAM signals in Rayleigh fading channels," *IEEE Commun. Lett.*, vol. 23, no. 8, pp. 1328–1331, Jun. 2019.

[43] L. Bariah, S. Muhaidat, and A. Al-Dweik, "Error probability analysis of non-orthogonal multiple access over Nakagami-m fading channels," *IEEE Trans. Commun.*, vol. PP, pp. 1–1, Oct. 2018.

[44] T. Assaf, A. J. Al-Dweik, M. S. E. Moursi, H. Zeineldin, and M. Al-Jarrah, "Exact bit error-rate analysis of two-user NOMA using QAM with arbitrary modulation orders," *IEEE Commun. Lett.*, vol. 24, no. 12, pp. 2705–2709, Dec. 2020.

[45] S. Bisen, P. Shaik, and V. Bhatia, "On ASER performance of M-ary QAM schemes over DF coordinated-NOMA," ser. IEEE Region 10 Conf. (TENCON), Nov. 2020, pp. 280–285.

[46] H. Yahya, E. Alsusa, and A. Al-Dweik, "Exact BER analysis of NOMA with arbitrary number of users and modulation orders," *IEEE Trans. Commun.*, vol. 69, no. 9, pp. 6330–6344, Sep. 2021.

[47] Y. Iraqi and A. Al-Dweik, "Power allocation for reliable sic detection of rectangular qam-based noma systems," *IEEE Trans. Veh. Technol.*, vol. 70, no. 8, pp. 8355–8360, 2021.

[48] F. Kara and H. Kaya, "A true power allocation constraint for non-orthogonal multiple access with m-qam signalling," ser. 2020 IEEE Microwave Theory and Techniques in Wireless Communications (MTTW), vol. 1, 2020, pp. 7–12.

[49] Y. Sun, Z. Ding, and X. Dai, "A new design of hybrid sic for improving transmission robustness in uplink noma," *IEEE Trans. Veh. Technol.*, vol. 70, no. 5, pp. 5083–5087, 2021.

[50] S. Park, "Performance analysis of triangular quadrature amplitude modulation in AWGN channel," *IEEE Commun. Lett.*, vol. 16, no. 6, pp. 765–768, Apr. 2012.

[51] P. Shaik, P. K. Singya, and V. Bhatia, "On impact of imperfect CSI over hexagonal QAM for TAS/MRC-MIMO cooperative relay network," *IEEE Commun. Lett.*, vol. 23, no. 10, pp. 1721–1724, Oct. 2019.

[52] D. Kumar, P. K. Singya, and V. Bhatia, "ASER analysis of hybrid receiver based SWIPT two-way relay network," *IEEE Trans. Veh. Technol.*, vol. 70, no. 10, pp. 10 018–10 030, Oct. 2021.

[53] M. Abramowitz and I. A. Stegun, *Handbook of mathematical functions: with formulas, graphs, and mathematical tables.* 9th ed. New York, NY, USA: Dover, 1970.

[54] I. S. Gradshteyn and I. M. Ryzhik, *Table of integrals, series, and products.* Academic Press, 2014.

[55] P. K. Singya, N. Kumar, V. Bhatia, and M.-S. Alouini, “On performance of hexagonal, cross, and rectangular qam for multi-relay systems,” *IEEE Access*, vol. 7, pp. 60 602–60 616, May 2019.

[56] A. Agarwal, R. Chaurasiya, S. Rai, and A. K. Jagannatham, “Outage probability analysis for NOMA downlink and uplink communication systems with generalized fading channels,” *IEEE Access*, vol. 8, pp. 220 461–220 481, Dec. 2020.

[57] F. B. Hildebrand, *Introduction to numerical analysis.* 2nd ed. Dover Publications, 1987.

[58] X. Chen, R. Jia, and D. W. K. Ng, “On the design of massive non-orthogonal multiple access with imperfect successive interference cancellation,” *IEEE Trans. Commun.*, vol. 67, no. 3, pp. 2539–2551, Mar. 2019.

[59] Y. Wang, J. Wang, D. W. Kwan Ng, R. Schober, and X. Gao, “A minimum error probability NOMA design,” *IEEE Trans. Wireless Commun.*, vol. 20, no. 7, pp. 4221–4237, Jul. 2021.

[60] N. Zhang, J. Wang, G. Kang, and Y. Liu, “Uplink nonorthogonal multiple access in 5G systems,” *IEEE Commun. Lett.*, vol. 20, no. 3, pp. 458–461, Mar. 2016.

[61] Y. Gao, B. Xia, K. Xiao, Z. Chen, X. Li, and S. Zhang, “Theoretical analysis of the dynamic decode ordering SIC receiver for uplink NOMA systems,” *IEEE Commun. Lett.*, vol. 21, no. 10, pp. 2246–2249, Oct. 2017.

[62] B. Xia, J. Wang, K. Xiao, Y. Gao, Y. Yao, and S. Ma, “Outage performance analysis for the advanced SIC receiver in wireless NOMA systems,” *IEEE Trans. Veh. Technol.*, vol. 67, no. 7, pp. 6711–6715, Jul. 2018.

[63] Z. Ding, Z. Yang, P. Fan, and H. V. Poor, “On the performance of non-orthogonal multiple access in 5G systems with randomly deployed users,” *IEEE Signal Pro. Lett.*, vol. 21, no. 12, pp. 1501–1505, Dec. 2014.

[64] Z. Ding, P. Fan, and H. V. Poor, "Impact of user pairing on 5G nonorthogonal multiple-access downlink transmissions," *IEEE Tran. Veh. Technol.*, vol. 65, no. 8, pp. 6010–6023, Sep. 2016.

[65] V. Ozduran, "Advanced successive interference cancellation for non-orthogonal multiple access," in *2018 26th Telecommunications Forum (TELFOR)*, 2018, pp. 1–4.

[66] X. Wang, F. Labeau, and L. Mei, "Closed-form BER expressions of QPSK constellation for uplink non-orthogonal multiple access," *IEEE Commun. Lett.*, vol. 21, no. 10, pp. 2242–2245, Jul. 2017.

[67] F. Wei, T. Zhou, T. Xu, and H. Hu, "BER analysis for uplink NOMA in asymmetric channels," *IEEE Commun. Lett.*, vol. 24, no. 11, pp. 2435–2439, Jun. 2020.

[68] Q. He, Y. Hu, and A. Schmeink, "Closed-form symbol error rate expressions for non-orthogonal multiple access systems," *IEEE Trans. Veh. Technol*, vol. 68, no. 7, pp. 6775–6789, May 2019.

[69] F. Kara and H. Kaya, "BER performances of downlink and uplink NOMA in the presence of SIC errors over fading channels," *IET Commun.*, vol. 12, no. 15, pp. 1834–1844, Jul. 2018.

[70] V. Ozduran, N. Nomikos, E. Soleimani, I. S. Ansari, and P. Trakadas, "Relay-aided uplink NOMA under non-orthogonal CCI and imperfect SIC in 6G networks," Dec. 2023. [Online]. Available: http://dx.doi.org/10.36227/techrxiv.24523801.v1

[71] Z. Ding, R. Schober, and H. V. Poor, "A new QoS-guarantee strategy for NOMA assisted semi-grant-free transmission," *IEEE Trans. Commun.*, vol. 69, no. 11, pp. 7489–7503, Jul. 2021.

[72] Y. Sun, Z. Ding, and X. Dai, "A new design of hybrid SIC for improving transmission robustness in uplink NOMA," *IEEE Trans. Veh. Techno.*, vol. 70, no. 5, pp. 5083–5087, Mar. 2021.

[73] J. S. Yeom, H. S. Jang, K. S. Ko, and B. C. Jung, "BER performance of uplink NOMA with joint maximum-likelihood detector," *IEEE Trans. Veh. Technol.*, vol. 68, no. 10, pp. 10 295–10 300, Oct. 2019.

[74] R. Campello, G. Carlini, C. E. C. Souza, C. Pimentel, and D. P. B. Chaves, "Successive interference cancellation decoding with adaptable decision regions for NOMA schemes," *IEEE Access*, vol. 10, pp. 2051–2062, Dec. 2022.

[75] H. Semira, F. Kara, H. Kaya, and H. Yanikomeroglu, "Error performance analysis of multiuser detection in uplink-NOMA with adaptive M-QAM," *IEEE Wireless Commun. Lett.*, vol. 11, no. 8, pp. 1654–1658, Aug. 2022.

[76] A. Agarwal, R. Chaurasiya, S. Rai, and A. K. Jagannatham, "Outage probability analysis for NOMA downlink and uplink communication systems with generalized fading channels," *IEEE Access*, vol. 8, pp. 220 461–220 481, Dec. 2020.

[77] Z. Ding, R. Schober, P. Fan, and H. V. Poor, "Simple semi-grant-free transmission strategies assisted by non-orthogonal multiple access," *IEEE Trans. Commun.*, vol. 67, no. 6, pp. 4464–4478, Jun. 2019.

[78] J. Men, J. Ge, and C. Zhang, "Performance analysis for downlink relaying aided non-orthogonal multiple access networks with imperfect CSI over Nakagami- m fading," *IEEE Access*, vol. 5, pp. 998–1004, Nov. 2017.

[79] S. Bisen, P. Shaik, and V. Bhatia, "On performance of energy harvested cooperative NOMA under imperfect CSI and imperfect SIC," *IEEE Trans. Veh. Technol.*, vol. 70, no. 9, pp. 8993–9005, Sep. 2021.

[80] V. Ozduran, B. S. B. Yarman, and J. M. Cioffi, "Opportunistic source-pair selection method with imperfect channel state information for multiuser bidirectional relaying networks," *IET Commun.*, vol. 13, no. 7, pp. 905–917, 2019.

[81] H. Qian, "Counting the floating point operations (FLOPS)," *MATLAB Central File Exchange*, Apr. 2022. [Online]. Available:

https://www.mathworks.com/matlabcentral/fileexchange/50608-counting - the-floating-point-operations-flops

[82] J. Kim and I. Lee, "Non-Orthogonal Multiple Access in Coordinated Direct and Relay Transmission," *IEEE Commun. Lett.*, vol. 19, no. 11, pp. 2037–2040, Nov. 2015.

[83] Z. Ding, M. Peng, and H. V. Poor, "Cooperative non-orthogonal multiple access in 5G systems," *IEEE Commun. Lett.*, vol. 19, no. 8, pp. 1462–1465, Jun. 2015.

[84] J. Men, J. Ge, and C. Zhang, "Performance analysis of nonorthogonal multiple access for relaying networks over Nakagami-m fading channels," *IEEE Trans. Veh. Technol.*, vol. 66, no. 2, pp. 1200–1208, Feb. 2017.

[85] Z. Ding, H. Dai, and H. V. Poor, "Relay selection for cooperative NOMA," *IEEE Wireless Commun. Lett.*, vol. 5, no. 4, pp. 416–419, Aug. 2016.

[86] P. Xu, Z. Yang, Z. Ding, and Z. Zhang, "Optimal relay selection schemes for cooperative NOMA," *IEEE Trans. on Veh. Technol.*, vol. 67, no. 8, pp. 7851–7855, Aug. 2018.

[87] Y. Li, Y. Li, X. Chu, Y. Ye, and H. Zhang, "Performance analysis of relay selection in cooperative NOMA networks," *IEEE Commun. Lett.*, vol. 23, no. 4, pp. 760–763, Apr. 2019.

[88] S. Lee, D. B. da Costa, Q. Vien, T. Q. Duong, and R. T. de Sousa, "Non-orthogonal multiple access schemes with partial relay selection," *IET Commun.*, vol. 11, no. 6, pp. 846–854, Apr. 2017.

[89] Y. Liu, Z. Ding, M. Elkashlan, and H. V. Poor, "Cooperative non-orthogonal multiple access with simultaneous wireless information and power transfer," *IEEE J. Sel. Areas Commun.*, vol. 34, no. 4, pp. 938–953, Apr. 2016.

[90] H. Dac-Binh and N. Sang Quang, "Outage performance of energy harvesting DF relaying NOMA networks," *Mobile Netw. and Appl.*, vol. 23, no. 6, pp. 1572–1585, Dec. 2018.

[91] Y. Zhang and J. Ge, "Performance analysis for non-orthogonal multiple access in energy harvesting relaying networks," *IET Commun.*, vol. 11, no. 11, pp. 1768–1774, Aug. 2017.

[92] H. Tran Manh, N. Tan. Nguyen Trungand Hoang, and P. Hiep, "Performance analysis of decode-and-forward partial relay selection in NOMA systems with RF energy harvesting," *Wireless Netw.*, vol. 25, no. 8, pp. 4585–4595, Feb. 2019.

[93] X. Li, J. Li, P. T. Mathiopoulos, D. Zhang, L. Li, and J. Jin, "Joint impact of hardware impairments and imperfect CSI on cooperative SWIPT NOMA multi-relaying systems," *Proc. IEEE/CIC Int. Conf. commun. China*, pp. 95–99, Jul. 2018.

[94] D. Do, M. Vaezi, and T. Nguyen, "Wireless powered cooperative relaying using NOMA with imperfect CSI," in *Proc. IEEE Globecom Workshops*, Dec. 2018, pp. 1–6.

[95] J. Men, J. Ge, and C. Zhang, "Performance analysis for downlink relaying aided non-orthogonal multiple access networks with imperfect CSI over Nakagami-m fading," *IEEE Access*, vol. 5, pp. 998–1004, Mar. 2017.

[96] E. N. Papasotiriou, A. A. Boulogeorgos, and A. Alexiou, "Performance analysis of THz wireless systems in the presence of antenna misalignment and phase noise," *IEEE Commun. Lett.*, vol. 24, no. 6, pp. 1211–1215, Jun. 2020.

[97] M. Alzenad and H. Yanikomeroglu, "Coverage and rate analysis for unmanned aerial vehicle base stations with LoS/NLoS propagation," in *Proc. IEEE Globecom Commun. Conf. Workshops*, Dec. 2018, pp. 1–7.

[98] X. Liang, Y. Wu, D. W. K. Ng, S. Jin, Y. Yao, and T. Hong, "Outage probability of cooperative NOMA networks under imperfect CSI with user selection," *IEEE Access*, vol. 8, pp. 117 921–117 931, May 2020.

[99] L. L. Scharf, *Statistical Signal Processing: Detection, Estimation, and Time-series Analysis.* Reading, MA: Addison-Wesley, 1991.

[100] I. Krikidis, J. Thompson, S. Mclaughlin, and N. Goertz, "Amplify-and-forward with partial relay selection," *IEEE Commun. Lett.*, vol. 12, no. 4, pp. 235–237, Apr. 2008.

[101] S. Parvez, D. Kumar, and V. Bhatia, "On performance of SWIPT enabled two-way relay system with non-linear power amplifier," in *National Conf. on Commun.*, Feb. 2020, pp. 1–6.

[102] A. Goldsmith, *Wireless Communications.* Cambridge University Press, 2005.

[103] P. Shaik, P. K. Singya, N. Kumar, K. K. Garg, and V. Bhatia, "On impact of imperfect CSI over SWIPT device-to-device (D2D) MIMO relay systems," in *2020 Int. Conf. on Signal Process. and Commun.*, 2020, pp. 1–5.

[104] W. Shuming, Z. Yudong, W. Shuihua, and J. Genlin, "A comprehensive survey on particle swarm optimization algorithm and its applications," *Math. Problems Eng.*, pp. 1211–1215, Feb. 2015.

[105] M. Song and M. Zheng, "Energy efficiency optimization for wireless powered sensor networks with nonorthogonal multiple access," *IEEE Sensors Lett.*, vol. 2, no. 1, pp. 1–4, Mar. 2018.

[106] A. Masaracchia, D. B. Da Costa, T. Q. Duong, M. Nguyen, and M. T. Nguyen, "A PSO-based approach for user-pairing schemes in NOMA systems: Theory and applications," *IEEE Access*, vol. 7, pp. 90 550–90 564, Jul. 2019.

[107] X. Lu, P. Wang, G. Li, D. Niyato, and Z. Li, "Short-packet backscatter assisted wireless-powered relaying with NOMA: Mode selection with performance estimation," *IEEE Trans. Cognitive Communications Networking*, vol. 8, no. 1, pp. 216–231, Mar. 2022.

[108] Y. Long, G. Huang, H. Zheng, S. Zhao, G. Liu, and D. Tang, "Cooperative multirelay network design with hybrid backscatter and wireless-powered relaying," *IEEE Internet Things J.*, vol. 9, no. 19, pp. 18 445–18 460, Oct. 2022.

[109] Y. Long, G. Huang, D. Tang, S. Zhao, and G. Liu, "Achieving high throughput in wireless networks with hybrid backscatter and wireless-powered communications," *IEEE Internet Things J.*, vol. 8, no. 13, pp. 10 896–10 910, Jul. 2021.

[110] Z. Ding, M. Peng, and H. V. Poor, “Cooperative Non-Orthogonal Multiple Access in 5G Systems,” *IEEE Commun. Lett.*, vol. 19, no. 8, pp. 1462–1465, Aug. 2015.

[111] Y. Guo, Y. Li, Y. Li, W. Cheng, and H. Zhang, “SWIPT assisted NOMA for coordinated direct and relay transmission,” in *2018 IEEE/CIC International Conference on Communications in China (ICCC)*, 2018, pp. 111–115.

[112] A. K. Shukla, K. Yadav, P. K. Upadhyay, and J. M. Moualeu, “Exploiting deep learning in the performance evaluation of EH-based coordinated direct and relay transmission system with cognitive NOMA,” *IEEE Commun. Lett*, pp. 1–1, 2023.

[113] Q. Zhang, L. Zhang, Y.-C. Liang, and P.-Y. Kam, “Backscatter-NOMA: A symbiotic system of cellular and internet-of-things networks,” *IEEE Access*, vol. 7, pp. 20 000–20 013, Feb. 2019.

[114] W. Chen, H. Ding, S. Wang, D. B. da Costa, F. Gong, and P. H. Juliano Nardelli, “Backscatter cooperation in NOMA communications systems,” *IEEE Trans. Wireless Commun.*, vol. 20, no. 6, pp. 3458–3474, Jun. 2021.

[115] S. Bisen and V. Bhatia, “Performance analysis of backscatter-based coordinated direct and relay transmission with NOMA,” in *IEEE Wireless Communication and Networking Conference*, 2023.

[116] X. Li, M. Zhao, M. Zeng, S. Mumtaz, V. G. Menon, Z. Ding, and O. A. Dobre, “Hardware impaired ambient backscatter NOMA systems: Reliability and security,” *IEEE Trans. Commun.*, vol. 69, no. 4, pp. 2723–2736, Apr. 2021.

[117] X. Pei, H. Yu, M. Wen, S. Mumtaz, S. Al Otaibi, and M. Guizani, “NOMA-based coordinated direct and relay transmission with a half-duplex/ full-duplex relay,” *IEEE Trans. Commun.*, vol. 68, no. 11, pp. 6750–6760, Nov. 2020.

[118] S. Wang, M. Xia, K. Huang, and Y.-C. Wu, “Wirelessly powered two-way communication with nonlinear energy harvesting model: Rate regions under

fixed and mobile relay," *IEEE Trans. Wireless Commun.*, vol. 16, no. 12, pp. 8190–8204, Dec. 2017.

[119] X. Li, J. Li, Y. Liu, Z. Ding, and A. Nallanathan, "Residual transceiver hardware impairments on cooperative NOMA networks," *IEEE Trans. Wireless Commun.*, vol. 19, no. 1, pp. 680–695, 2020.

[120] Y. Ye, L. Shi, X. Chu, G. Lu, and S. Sun, "Mutualistic cooperative ambient backscatter communications under hardware impairments," *IEEE Trans. Commun.*, vol. 70, no. 11, pp. 7656–7668, Nov. 2022.

[121] H. Yang, H. Ding, M. Elkashlan, H. Li, and K. Xin, "A novel symbiotic backscatter-NOMA system," *IEEE Trans. Veh. Technol.*, vol. 72, no. 8, pp. 11 006–11 011, Aug. 2023.

[122] M. Elsayed, A. Samir, A. A. A. El-Banna, X. Li, and B. M. ElHalawany, "When NOMA multiplexing meets symbiotic ambient backscatter communication: Outage analysis," *IEEE Trans. Veh. Technol.*, vol. 71, no. 1, pp. 1026–1031, Jan. 2022.

[123] F. Rezaei, D. Galappaththige, C. Tellambura, and S. Herath, "NOMA-assisted symbiotic backscatter: Novel beamforming designs under imperfect sic," *IEEE Trans. Veh. Technol.*, pp. 1–15, 2023.

[124] W. U. Khan, X. Li, M. Zeng, and O. A. Dobre, "Backscatter-enabled NOMA for future 6G systems: A new optimization framework under imperfect SIC," *IEEE Commun. Lett.*, vol. 25, no. 5, pp. 1669–1672, May 2021.

[125] S. Bisen, J. Jose, V. Bhatia, A. K. Mishra, and K. Choi, "Hybrid backscatter NOMA under imperfect CSI and hardware impairment," *IEEE Commun. Lett.*, pp. 1–1, 2023.

[126] G. Wang, F. Gao, R. Fan, and C. Tellambura, "Ambient backscatter communication systems: Detection and performance analysis," *IEEE Trans. Commun.*, vol. 64, no. 11, pp. 4836–4846, Nov. 2016.

[127] W. Guo, H. Zhao, C. Song, S. Shao, and Y. Tang, "Direct-link interference cancellation design for backscatter communications over ambient DVB signals," *IEEE Trans. Broadcasting*, vol. 68, no. 2, pp. 317–330, Jun. 2022.

List of Publications

Publications from thesis:

Patent:

1. V. Bhatia, **S. Bisen**, "MULTI-USER DOWNLINK NOMA COMMUNICATION SYSTEM AND METHOD THEREOF", Indian Patent (Filed)

Journal Papers:

1. **S. Bisen**, Shaik, P, Jose, J, Nebhen, J, Krejcar, O, Bhatia, V. "ASER analysis of generalized hexagonal QAM schemes for NOMA systems over Nakagami-m fading channels", *Int J Commun Syst.* 2023; 36(6):e5440.

2. **S. Bisen**, V. Bhatia, P. Brida, "Successive Interference Cancellation with Multiple Feedback in NOMA-Enabled Massive IoT Network", *EURASIP J. Wireless Commun. and Net.*, 2024 (Accepted).

3. **S. Bisen**, P. Shaik, and V. Bhatia, "On performance of energy harvested cooperative NOMA under imperfect CSI and imperfect SIC", *IEEE Trans. Veh. Technol.*, vol. 70, no. 9, pp. 8993–9005, Sep. 2021

4. **S. Bisen**, J. Jose, V. Bhatia, A. K. Mishra and K. Choi, "Hybrid Backscatter NOMA Under Imperfect CSI and Hardware Impairment", *IEEE Commun. Letters*, vol. 27, no. 11, pp. 3078-3082, Nov. 2023,

5. **S. Bisen**, J. Jose, Z. Ding, K. Choi and V. Bhatia, "On Performance of Backscatter-NOMA Systems: Symbiotic Communication for IoT Devices", *IEEE Trans. Veh. Technol.*, 2024 (Early access).

Conference Papers:

1. **S. Bisen**, J. Jose, S. Jain, A. Kaushik, V. Bhatia, "On Outage Performance of Backscatter NOMA SystemUnder Imperfect DLI Cancellation", *IEEE International Symposium on Personal, Indoor and Mobile Radio Communications*, 2024.

2. **S. Bisen**, V. Bhatia, "Ergodic Capacity Analysis of Backscatter based CDRT-NOMA Systems", *Int. Conf. Commun. Sys. Net. (COMSNETS).* IEEE, 2024 , Poster track.

3. **S. Bisen** and V. Bhatia, "Performance Analysis of Backscatter-based Coordinated Direct and Relay Transmission with NOMA," *IEEE Wireless Communications and Networking Conference (WCNC)*, Glasgow, United Kingdom, 2023, pp. 1-6.

4. **S. Bisen**, P. Shaik, and V. Bhatia, "On ASER performance of M-ary QAM schemes over DF coordinated-NOMA", *IEEE REGION 10 CONFERENCE (TENCON)*, 2020.

Book Chapter:

1. AS Parihar, **S. Bisen**, V Bhatia, O Krejcar, "Machine Learning for Non-Orthogonal Multiple Access", *Intelligent Communication Networks,* 135-153, 2024.

Publications apart from thesis:

Journal Papers:

1. J. Jose, **S. Bisen**, P. Shaik, S. Biswas, K. Singh and V. Bhatia, "Performance Analysis of IRS Assisted Full-Duplex Systems with Different Downlink and Uplink Users", *IEEE Trans. Veh. Technol*, 2024 (Early access).

2. J. Jose, P. Shaik, **S. Bisen**, A. Srivastava, V. Bhatia, and K. Choi, "Performance analysis and optimization of frequency division duplex based virtual full-duplex communication systems", *Ad Hoc Networks*, vol. 154, p.103379, Dec. 2023. (IF: 4.8)

3. J. Jose, **S. Bisen**, P. Shaik, O. Krejcar, K. Choi and V. Bhatia, "Virtual Full-Duplex Communication Enabled STAR-RIS: Performance Analysis and Machine Learning-Assisted Optimization", *IEEE Trans. Cog. Commun. Network* 2024 (Under Minor Revision).

4. **S. Bisen**, Vimal Bhatia, Amit Kumar Mishra et al. "Performance Analysis of NOMA System with QoS-Guarantee Scheme", 02 August 2023, PREPRINT

(Version 1) available at Research Square [https://doi.org/10.21203/rs.3.rs-2836358/v1] (Under Revision).

Conference Papers:

1. V. Bhatia and **S. Bisen**, "Implementation and Performance Analysis of NOMA on Software Defined Radio", *IEEE International Conference on Advanced Networks and Telecommunications Systems (ANTS)* 2023.

2. J. Jose, P. Shaik, **S. Bisen**, and V. Bhatia, "On outage probability analysis of uplink cooperative VFD-NOMA over Nakagami-m faded channels, *IEEE Nat. Conf. Commun. (NCC)*, 2021, pp. 1–6.

3. J. Jose, P. Shaik, **S. Bisen**, V. Goyal, and V. Bhatia, "Frequency division duplex based cooperative VFD: Outage analysis and relay power allocation," *Int. Conf. Commun. Sys. Net. (COMSNETS)*, 2023, pp. 1–7.

4. J. Jose, P. Shaik, **S. Bisen**, and V. Bhatia, "Ergodic rate analysis and optimization of full-duplex STAR-RIS communication systems," *Joint European Conference on Networks and Communications & 6G Summit (EuCNC/6G Summit)*, 2023, pp. 1–6.